Two-photon ionization of many-electron atoms

seit 1558

Dissertation

zur Erlangung des akademischen Grades
doctor rerum naturalium (Dr. rer. nat.)

vorgelegt dem Rat der Physikalisch-Astronomischen Facultät
der Friedrich-Schiller-Universität Jena

von Bsc. Jiří Hofbrucker

geboren am 19.2.1992 in Ivančice, Tschechische Republik

Gutachter:

1. Prof. Dr. Stephan Fritzsche, Friedrich-Schiller-Universität Jena
2. Prof. Dr. Alejandro Saenz, Humboldt-Universität zu Berlin
3. Prof. Dr. Eva Lindroth, Alba Nova University Center

Tag der Disputation: 8. Juni 2020

Zusammenfassung

Bis vor kurzem war die nichtlineare Wechselwirkung zwischen Licht und Materie auf nur niedrige Photonenenergien beschränkt, die von optischen Lasern erzeugt wurden. Vor etwa einem Jahrzehnt jedoch revolutionierte der Aufstieg von Freie-Elektronen-Laseranlagen das Feld der nichtlinearen Wechselwirkung zwischen Licht und Materie, indem sie intensive, energiereiche Lichtimpulse lieferten. Heute werden solche Laser für die Forschung in den Bereichen Materialwissenschaften, chemische Technologie, Biophysik, Festkörperphysik sowie für die Grundlagenforschung eingesetzt. Es sind die neuen experimentellen Möglichkeiten, die Freie-Elektronen-Laser bieten, die die in dieser Arbeit vorgestellten Arbeiten motiviert haben.

Der Zwei-Photonen-Ionisationsprozess ist eine der einfachsten nichtlinearen Wechselwirkungen, bei denen die Absorption von zwei Photonen durch ein Atom (oder ein Molekül) dazu führt, dass eines seiner gebundenen Elektronen zum Kontinuum befördert wird. Diese Arbeit präsentiert Studien zur Zwei-Photonen-Ionisation neutraler Atome. Nach einer kurzen historischen Einführung in das Thema der nichtlinearen Wechselwirkung zwischen Licht und Materie wird die Dichtematrix abgeleitet, die den Zustand eines Atoms und eines Photoelektronens nach der Zwei-Photonen-Ionisation beschreibt. Die Dichtematrix enthält die vollständigen Informationen über das Gesamtsystem bestehend aus einem Photoion und einem Photoelektron. In jedem nachfolgenden Kapitel wird ein Teil dieser Dichtematrix verwendet, um charakteristische Größen wie den gesamten Zwei-Photonen-Ionisationsquerschnitt, die Winkelverteilungen der Photoelektronen, die Ionenpolarisation oder sogar die physikalischen Eigenschaften des Fluoreszenzphotons zu erhalten, das durch den nachfolgenden Zerfall des erzeugten Photoions wird. Die physikalischen Eigenschaften dieser Größen sowie interessante Phänomene wie elliptischer Dichroismus, Polarisationstransfer und relativistische und Screening-Effekte werden untersucht.

Bei der Ein-Photon-Ionisationprozess wird die Photonenenergie, für die der dominante Ionisationskanal verschwindet, als Cooper-Minimum bezeichnet. Dieses Konzept wird auf die nichtlineare Ionisation von Atomen ausgedehnt und die Wirkung des Minimums auf alle oben genannten Größen untersucht. In dieser Arbeit wird gezeigt, dass das nichtlineare Cooper-Minimum zu starken Variationen praktisch aller beobachtbaren Größen des Zwei-Photonen-Ionisationsprozesses führt. Beispielsweise kann der Polarisationstransfer von dem einfallenden zum fluoreszierenden Photon maximiert werden, ebenso wie der elliptische Dichroismus bei der Winkelverteilung von Photoelektronen. Weiterhin wird vermutet, dass die Detektion der Energieposition des nichtlinearen Cooper-Minimums zu einem Vergleich von experimentellen Messungen und theoretischen Berechnungen mit bisher unerreichter Genauigkeit führen könnte.

Summary

Until recently, the nonlinear interaction between light and matter has been restricted to only low photon energies produced by optical lasers. However, about a decade ago, the rise of free-electron laser facilities revolutionized the field of nonlinear light-matter interaction by delivering intense high-energy light pulses. Today, such lasers are used for research in materials science, chemical technology, biophysical science, solid-state physics as well as fundamental research. It is the new experimental possibilities provided by free-electron lasers that motivated the work presented in this thesis.

Two-photon ionization process is one of the simplest nonlinear interactions in which absorption of two photons by an atom (or a molecule) leads to promoting one of its bound electrons to continuum. This work presents studies of two-photon ionization of neutral atoms. After a brief historical introduction to the topic of nonlinear light-matter interaction, the density matrix describing the state of an atom and a photoelectron following two-photon ionization is derived. The density matrix contains the complete information about the overall system consisting of a photoion and a photoelectron. In each successive chapter, part of this density matrix is used to obtain characteristic quantities such as total two-photon ionization cross section, photoelectron angular distributions, ion polarization or even degree of polarization of fluorescence photon produced by subsequent decay of the photoion. Physical properties of these quantities are studied and intriguing phenomena, such as elliptical dichroism, polarization transfer as well as relativistic and screening effects are investigated.

In one-photon ionization, the photon energy for which the dominant ionization channel vanishes is called the Cooper minimum. This concept is extended to nonlinear ionization of atoms and the effect of the minimum on all above mentioned quantities is studied. In this work it is shown, that the nonlinear Cooper minimum leads to strong variation in practically all observables of the two-photon ionization process. For example, the polarization transfer from the incident to fluorescence photon can be maximized and so can be the elliptical dichroism in photoelectron angular distributions. Furthermore, it is theorized, that detection of the energy position of the nonlinear Cooper minimum could lead to comparison of experimental measurements and theoretical calculations at hitherto unreachable accuracy.

Contents

1 Introduction

When atoms are exposed to electromagnetic radiation with a frequency above a certain threshold, the radiation may be absorbed and electrons are emitted. This phenomena was discovered by Heinrich Hertz and Wilhelm Hallwachs in 1887 and is called the photoelectric effect, or photoionization. In 1900, the German physicist Max Planck suggested that the energy carried by electromagnetic waves could only be released in packets of energy. In 1905, Albert Einstein advanced Planck's hypothesis and utilized the idea that light energy is carried in discrete quantized packets to explain the photoionization process, which was a key step in the development of quantum mechanics. The necessity for electromagnetic radiation to have a frequency above a certain (ionization) threshold was explained. However, is there really a strict limit on the light frequency in order to free an electron from an atom?

Simultaneous absorption of two light quanta was first suggested by Marie Göppert-Mayer who also worked out the corresponding theoretical formalism in 1931 [1]. The theoretical work lead to a prediction, that an atom can be ionized by light even if its frequency does not overcome the ionization threshold, however only under the condition that several photons are absorbed. This idea was, however, decades ahead of its time as the experimental possibilities to observe such process were not yet attainable at the time. Generally, multi-photon absorption cross sections are low, and hence, intense light sources are required to experimentally induce such interactions. It is therefore no wonder that further progress in studies of nonlinear light-matter interaction (where two or more photons interact with an atom) was achieved only after the invention of the technique of light amplification by stimulated emission of radiation (better known by its acronym *laser*), in the 1960s [2].

The ability to amplify light to very high intensities opened up new possibilities for applications in industry as well as in many field of scientific research. In atomic physics, lasers made it possible to observe nonlinear processes such as multiphoton absorption [3–6], where multiple photons are absorbed by an atom and one electron is emitted, two-photon double ionization [7–10] during which absorption of two photons leads to emission of two electrons, or tunnel ionization [11, 12], where the strong laser field distorts the atomic Coulomb potential and allows for the bound electrons to tunnel out. Although these processes share similar characteristics, the theoretical approaches how to calculate them vary according to the relative strength of the nuclear Coulomb and the radiation fields. To determine the dominance of tunneling or multi-photon ionization, Keldysh introduced a parameter $\gamma = \omega\sqrt{2m|E_0|}/(e\varepsilon_0)$ [11], with electron binding energy E_0 and the field amplitude ε_0. The Keldysh parameter draws a line between the tunneling ($\gamma < 1$) and multi-photon absorption regimes ($\gamma > 1$). While in the tunneling regime, it is important to account for the intensity of the radiation field in the atomic Hamiltonian and the Coulomb potential of the nucleus plays a secondary role (in so called strong field approximation the Coulomb potential is neglected for the continuum electron), in the multi-photon absorption regime it is vice versa. In this thesis, we will be strictly concerned only with the multi-photon regime, however, it is worth pointing out the successes of the strong field ionization which is often applied within the strong-field approximation or in the framework of the time-dependent Schrödinger theory. This approach has successfully described the high-harmonic generation in atoms and molecules with incident plane [13, 14] or twisted photon field [15], and has even been extend to account for higher multipole orders in above-threshold ionization by spatially structured light beams [16].

The first observations of many-photon absorption were reported already in 1960s from measurements of two-photon excitation of inorganic crystals and cesium vapor [17, 18]. Only few years later, also the two-photon ionization was observed for the first

time [19]. The theoretical efforts to describe the first evidence of nonlinear light matter interaction went hand in hand with the experiments, see e.g. [20–23] for the pioneering publications. In one of them, Zernik [21] analysed the dependence of the total two-photon ionization cross section on the nuclear charge and introduced a scaling law which relates the cross sections for two-photon ionization of K shell electrons of an arbitrary atom to the corresponding cross section for ionization of hydrogen atom. This scaling law estimates the cross sections for ionization of an atom with nuclear charge Z to be $\sigma(Z) = Z^{-6}\sigma(Z = 1)$. This law is still often used for a comparison of two-photon K shell ionization experiments [24–27] with which it reaches a good agreement. By now, the study of two-photon ionization of hydrogen-like atoms has been carried out in much detail, including the analysis of the relativistic and retardation effect contributions to the process as well as two-photon above-threshold ionization, where two photons are absorbed an atom, but already one has enough energy to ionize it [28–31].

Although lasers started off the research of nonlinear light-matter interaction and still play an important role in it today, the available photon energies are restricted to few electronvolts (eVs). This means that lasers are well suited to probe the dynamics of outer shell electrons, but unfortunately, do not provide means to investigate inner-shell electrons. Very common source of X-rays (often used for medical applications) are X-ray tubes, which consist of a vacuum tube in which electrons accelerate to high energies of about 50 keV, strike a metal target and generate unpolarized X-rays by bremsstrahlung or X-ray fluorescence. However, the intensity of the pulses is generally insufficient to drive a nonlinear process. Other light sources, such as synchrotron facilities, can produce polarized photon pulses of even higher energies, but suffer from the same beam intensity limitations. Another promising alternative for studying nonlinear light-matter interaction with XUV photons was based on high-harmonic generation produced by a tabletop lasers. Although there were successful experiments carried out about two decades ago [32–34], the loss of intensity in the process of generation of the high-harmonic orders is large, which significantly lowers the potential of this experimental technique.

Both, X-ray tubes and synchrotron radiation sources are incoherent light sources. In the visible light spectrum laser generates coherent radiation. In 1971, Madey introduced the concept of coherent XUV and x-ray light source, the free-electron laser (FEL) [35]. His original design consisted of a linear accelerator, an undulator magnet, two mirrors and an input electromagnetic wave, which generates stimulated emission from the electrons, amplifying the input wave. The lack of materials to manufacture mirrors to reflect XUV and X-ray light pulses lead to a creation of single pass free-electron lasers. After much theoretical as well as experimental research aiming to improve the functionality of free-electron lasers, the first large scale facilities were build about thirty years later after the Madey's publication and many more followed in the following decades, see e.g. [36] for detailed historical development.

The access to high energetic intense light pulses provided by free-electron facilities opened plethora of new opportunities to study the interaction of light with matter. One of the main challenge is to understand the complete electron dynamics of many-electron atoms upon interacting with the free-electron laser pulses. Atoms in these strong light fields reach high atomic charge states by means of many-photon multiple ionization which has been driving experimental as well as theoretical progress until today [37–46]. From theoretical side, the need for many-electron theory to describe the sequential as well as nonsequential ionization steps and subsequent Auger dynamics became unavoidable, which resulted in rigorous many-electron description of two-photon above-threshold ionization [47, 48] or in development of publicly available codes to treat the theoretical description of fundamental x-ray-atom interaction [49] as well as more general codes for providing tools for performing atomic structure calculations and

transition amplitudes to describe light-matter interaction [50]. From another point of view, the possibility to produce very short pulses at free-electron lasers or to overlap these pulses with intense optical light fields resulted in need to account for the beam properties and laser induced effect, such as Stark shift. This motivation has pushed forward the progress of time-dependent perturbation theory treatment as well as time-dependent solutions of the Schrödinger equation [43, 51–55].

Instead of studying the complete electron dynamics of an atom upon irradiation by a free-electron laser pulse, some experiments concentrated on describing individual nonlinear processes happening during the interaction. This is where we return to the process of two-photon ionization of atom. Owing to the new possibilities provided by the free-electron lasers, the fundamental two-photon ionization process can be investigated from new perspectives. For example, it became possible to study one of the simplest elements, the helium atom, which was out of reach for the optical lasers. Free-electron lasers are capable of producing any photon energy to drive a bound-bound transition or to ionize the helium atom. This allowed to study the photoelectron angular distributions in the case of direct two-photon ionization of helium [56, 57] as well as in the case of pumping the helium atom with an XUV pulse and then ionizing the electrons from Rydberg states with two IR photons [58]. But the photon energies accessible by free-electron lasers go far beyond tens of electronvolts. There have been number of experiments using nonlinear absorption by $1s$ electrons of solids to investigate the relation between one- and two-photon absorption or to access (one-photon absorption) dipole forbidden states [24–27].

Free-electron lasers also offered a new view on some well-known effects such as the Cooper minimum. The Cooper minimum in one-photon ionization process [59, 60] describes the incident photon energy at which the dominant ionization channel vanishes. This behavior is strongly projected into observable quantities such as total cross section and photoelectron angular distributions. Cooper minimum does not only influence the magnitude of the total cross section, but more significantly, can strongly affect the photoelectron angular distributions [61]. It has been shown theoretically before [62], that strong anisotropic effects can be observed near Cooper minima due to relativistic and correlation effects, which are necessary to explain experimental measurements [61, 63]. Recently, free-electron laser pulses have been used to study the asymmetry of photoelectron angular distribution in photoionization of argon atoms at the Cooper minimum and it has been shown that the induced effects increase with the charge state of the target atom [46].

This thesis is dedicated to a detailed study of the two-photon ionization process. Using the independent particle approximation and relativistic second-order perturbation theory, the transition amplitudes describing the two-photon ionization process are calculated. These transition amplitudes are the building blocks used within density matrix theory to describe the most common observables relevant for an ionization process. Moreover, the analysis of the transition amplitude yielded an extension of the concept of Cooper minimum to the nonlinear regime. This *nonlinear Cooper minimum* strongly alters the observable quantities and gives us unique opportunity to study relativistic effects or to probe the theoretical representation of the complete atomic spectrum.

With the ever increasing power of free-electron lasers, we are reaching the point, where we are able to probe strongly bound electrons of atomic systems where relativistic effect may play a significant role. For this reason, we concentrate our discussion to ionization of deeply bound electrons and apart for few exceptions, we will present calculations for two-photon ionization of K and L shell electrons only. Nevertheless, the theoretical description provided in this work is general and applicable to other electron shells. Although we base our theoretical description on relativistic approach, two-photon ionization also gives rise to many interesting effects which have nonrelativistic

nature and relativistic description would be unnecessarily complex or even confusing. For this reason, the so called top to bottom approach is used throughout this thesis. We always start with a general fully relativistic description, however, then we reduce our formalism to nonrelativistic limits in which we neglect the electron spin degree of freedom and consider electron wave functions as solutions of Schrödinger equation. In evaluating two-photon ionization cross sections, the various contributions of relativistic description are evaluated and their importance analysed.

This thesis is structured as follows. In chapter 2, we introduce the theoretical machinery needed for the description of the two-photon ionization process. Brief introduction to the Dirac equation as well as to basics of density matrix theory is provided. Finally, the density matrix describing the final state of an atomic system after a two-photon ionization process is derived. The main purpose of this thesis is to analyze individual properties of this density matrix. The analysis starts in chapter 3 with the most basic quantity used to describe a physical process, the total cross section. The dependence of the total two-photon ionization cross section on nuclear charge, photon energy and polarization is discussed and specific examples are presented to illustrate this dependence. Moreover, individual contributions to relativistic effects are investigated. In chapter 4, the photoelectron angular distributions are studied. The dependence of electron emission direction on the incident photon polarization is studied and relativistic effects are evaluated. The phenomenon of elliptical dichroism is introduced and its origin is explained. Moreover, the conditions needed to achieve a maximum elliptical dichroism are laid out and a suggestion how to fulfill these conditions is proposed. Chapter 5 discusses the magnetic state of the produced photoion. The possibility to produce a polarized photoion by two-photon ionization is exploited and the dependence of the polarization transfer from the incident photon to the photoion on photon properties is analyzed. In the case of two-photon ionization of inner-shell electrons, the produced photoion is in an excited state and a possible subsequent relaxation process is the radiative decay. Chapter 6 investigates the properties of the photon emitted during the radiative decay. The degree of polarization of this photon carries the information of atomic structure as well as the magnetic state of the photoion. Finally, chapter 7 offers a summary of this thesis and discusses interesting opportunities for future research which would continue the efforts presented in this thesis. Some materials from our own previous publications [64–68] have been used in writing this thesis. Relativistic units will be used throughout this thesis unless otherwise stated ($\hbar = c = m_e = 1$).

2 Theoretical Formalism for Description of Two-Photon Atomic Ionization

It is the aim of this chapter to give a brief introduction to relativistic atomic theory and to lay out the basic description of two-photon ionization, which will serve later for detailed analysis of this second-order process. Using the Dirac equation, we first describe the wave functions governing the motion of electrons in an atom without the presence of an external field. The interaction between individual electrons of a many-electron atom is represented by a mean field potential. This approximation is called the *independent particle* approximation and will be used throughout this work. The interaction between the atom and electromagnetic field is described using the second-order perturbation theory. In the second part of this chapter, we utilize these basic principles to obtain the transition amplitude describing the two-photon ionization process. As the transition amplitude is the key quantity to describe the two-photon ionization process itself, we analyze its properties and discuss the approach for its numerical evaluation. Finally, we introduce the concept of density matrices and derive a general density matrix for the final state of the considered system which consists of an ionized atom and a photoelectron.

2.1 Brief introduction to atomic theory

Dirac equation is the relativistic wave equation for spin-1/2 particles. It is, therefore, capable of describing electrons in atoms, including the fine structure of the atomic states. In the independent particle picture, the Dirac orbital $|n\kappa m\rangle$, characterised by the principal quantum number n, the relativistic angular momentum κ and projection of the total angular momentum m, satisfies the single-particle time-independent Dirac equation

$$\hat{H}_0(r)\,|n\kappa m\rangle = \epsilon_{n\kappa}\,|n\kappa m\rangle\,, \tag{2.1}$$

where m_e is the electron rest mass, $\epsilon_{n\kappa}$ is the single electron energy, $\hat{H}_0$ is the Dirac Hamiltonian and the spatial dependence of the wave function is implied by the braket notation. In relativistic units, the Hamiltonian describing an electron of an arbitrary atom is given by

$$\hat{H}_0(r) = \big(-i\boldsymbol{\alpha}\cdot\boldsymbol{\nabla} + m_e\beta - \frac{\alpha Z}{r} + V(r)\big), \tag{2.2}$$

where $\boldsymbol{\alpha}$ and β are the hermitian Dirac matrices, Z is the nuclear charge, and $V(r)$ represents the electron screening potential which partially accounts for the electron interaction. Each term of the Hamiltonian can be interpreted with a physical meaning. The first term, for instance, represents the operator for kinetic energy of the electron with the matrix $\boldsymbol{\alpha}$ appearing as the operator transcription of velocity. The second term represents the electron rest energy, while the last two terms describe the electromagnetic interaction between charged particles. Specifically, the third term describes the Coulomb interaction of the electron with the nucleus, while the last term represents an approximate screening potential created by the Coulomb field of all other electrons of the atom.

The solution to the above equation with spherically symmetric potential can be separated into radial and angular part. The particle wavefunction is given by a four-component spinor

$$|n\kappa m\rangle = \frac{1}{r}\begin{pmatrix} P_\kappa(r)\Omega_{\kappa m}(\theta,\phi) \\ iQ_\kappa(r)\Omega_{-\kappa m}(\theta,\phi)\end{pmatrix} \tag{2.3}$$

in which the upper two components correspond to the spin up and spin down positive-energy states, while the lower two refer to the negative-energy states. The angular

functions $\Omega_{\kappa m}(\theta, \phi)$ are normalized spin-angular functions defined as eigenfunctions of the angular momentum operators $\boldsymbol{J}^2, \boldsymbol{L}^2$, and J_z. The exact expression of these functions can be found for example in Ref. [69]. The functions P_κ and Q_κ describe the radial dependence of the wave function and are called the large and small components of the wave function. The radial functions depend on the quantum number κ which is related to the nonrelativistic notation with orbital angular momentum l and total angular momentum j as

$$\kappa = \begin{cases} -(l+1) & \text{for } j = l + 1/2 \\ l & \text{for } j = l - 1/2 \end{cases} . \tag{2.4}$$

Having introduced the relativistic wave functions, it is appropriate to discuss its nonrelativistic limits. Under certain circumstances, the relativistic treatment does not provide any additional information than a nonrelativistic treatment. However, the nonrelativistic treatment is often easier to understand, and hence, can provide simpler, more intuitive analytical description. In this thesis, we will often reduce the theoretical treatment to a nonrelativistic limit for analytical analysis, and later numerically verify the validity of this approximation. In the next chapter, we will study the total two-photon ionization cross section, for which we will analyze the individual contributions to the relativistic description. One such contribution arises from the contribution of negative continuum (the lower component of Eq. (2.3)) to the ionization process. The two-photon ionization process is generally determined by its positive-energy states, thus neglecting the negative continuum states for simplicity is often justified. Leaving out the negative continuum states from the calculation is called the *no-pair approximation*. The nonrelativistic limit itself means, that the electron wave functions are not solutions of relativistic Dirac, but nonrelativistic Schrödinger equation

$$\left(\frac{-\boldsymbol{\nabla}^2}{2} - \frac{Z}{r} + V(r)\right) |nlm_l\rangle = \epsilon_{n\kappa} |nlm_l\rangle . \tag{2.5}$$

The solutions to the Schrödinger equation can be separated into radial and angular parts, analogously to the Dirac wave functions. The nonrelativistic electron wave functions take the form

$$|nlm_l\rangle = \frac{1}{r} P_l(r) Y_{lm_l}(\theta, \phi). \tag{2.6}$$

The exact form of the solutions for a hydrogen atom can be found in many quantum mechanics textbooks, e.g. [70]. As it becomes apparent from the above equations, the nonrelativistic wave function lacks the degrees of freedom of electron spin, and hence, the final wave function is described by its orbital angular momentum only. Moreover, it is a general feature that the maximum of the probability density of the relativistic radial wave function P_κ is nearer to the atomic nucleus than the nonrelativistic solution P_l, this difference is called the *relativistic wave function contraction*. To visualise this contraction, we present Fig. 1, where the wave function of the $1s$ and $2p$ electrons of neutral uranium atom is plotted as a solution of Dirac (dot-dashed blue) or Schrödinger (solid green) equation. From the figure it is apparent that the maximum of the relativistic wave function is nearer to the atomic nucleus ($r = 0$) than the nonrelativistic wave function, which is stretches further away from the nucleus. This wave function contraction impacts various observables in atomic processes. We will investigate the contribution of this relativistic effect (and others) to the total two-photon ionization cross section in Sec. 3.2.3.

We now extend the theory of single-electron atomic states to many-electron description. We construct many-electron atomic states within the framework of second-quantization, where the wave functions describing two- or more- electron states can be constructed equivalently to a typical linear combination of Slater determinants [70]. It

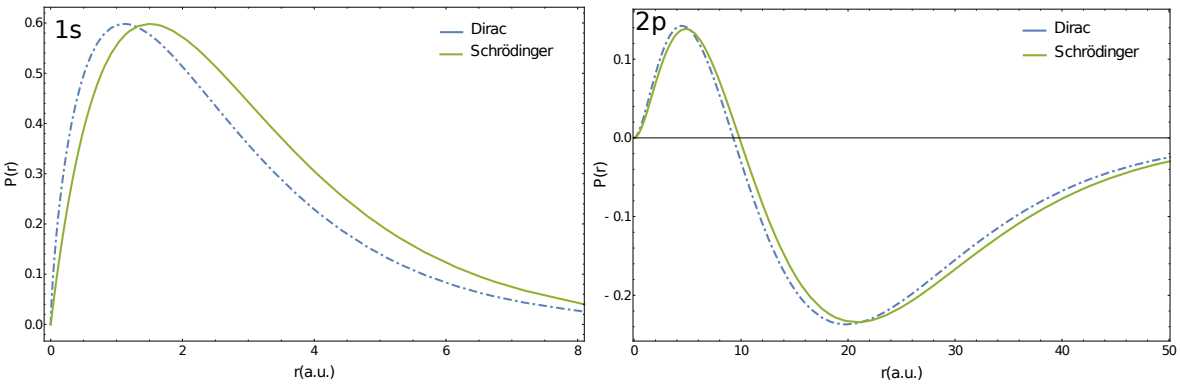

Figure 1: Wave functions of $1s$ (left) and $2p$ (right) electrons of neutral uranium as a function of distance from atomic nucleus. The wave functions have been calculated using the Dirac (dot-dashed blue) or Schödinger (solid green) equation. A clear shift of the wave function maximum towards the atomic nucleus can be seen in the figure. This wave function contraction impacts various observables in atomic processes.

is known that the total angular momentum of a fully occupied electron shell is equal to zero, whereas the angular momenta of an open shell electrons need to be coupled together. We can, therefore, construct the many-electron wave function as follows

$$\begin{aligned} |\alpha_i J_i M_i\rangle &= \mu \underbrace{\sum_{m_k M'_k} \langle j_1 m_1, j_2 m_2 \,|\, J_{12} M_{12}\rangle \ldots \langle J_{1x-1} M_{1x-1}, j_x m_x \,|\, J_i M_i\rangle}_{\text{coupling of valence electrons}} \\ &\times \underbrace{a^\dagger_{j_1 m_1} a^\dagger_{j_2 m_2} \ldots a^\dagger_{j_x m_x}}_{\text{valence electrons}} \underbrace{a^\dagger_{j_{c1} m_{c1}} \ldots a^\dagger_{j_{cf} m_{cf}}}_{\text{closed shell electrons}} |0\rangle \,, \end{aligned} \tag{2.7}$$

where μ is a normalization factor, $|0\rangle$ is the vacuum state, $a^\dagger_{jm}$ are the electron creation operators. Moreover, $\langle .., .. \,|\, ..\rangle$ is the Clebsch-Gordan coefficient and the capital letters J and M correspond to the many-electron total angular momenta. The symbol α represents all other quantum number necessary to describe the many-electron state. In this formalism, the total energy of the many-electron state is simply given by the sum of the individual single-electron energies

$$E_i = \epsilon_{n_1\kappa_1} + \epsilon_{n_2\kappa_2} + \ldots \epsilon_{n_n\kappa_n}. \tag{2.8}$$

Our goal is to describe atoms in electromagnetic fields, specifically, a single process where an atom absorbs two-photons. However, until now, only description of electron wave functions without the presence of external field were presented. This is because we will consider cases where the Coulomb field acting on the electrons is generally much stronger than the external photon field. This means, that we can use our derived wave functions and treat the electron-photon interaction perturbatively. Two-photon ionization is described within second-order perturbation theory and the interaction is described by transition amplitudes.

2.2 Two-photon ionization transition amplitudes

As mentioned in the previous subsection, we treat the interaction of atomic electrons with an external electromagnetic field perturbatively. We wish to describe the process in which an atom in an initial electronic state $|\alpha_i J_i M_i\rangle$ absorbs two photons $\gamma(\omega)$ each with energy ω. We will exclusively consider the case when absorption of one photon is not sufficient to ionize a particular electron, i.e. $\omega < \epsilon_{n_1\kappa_1}$. Due to the absorption of

the two photons, the initial state is excited into a final state $|\alpha_f J_f M_f\rangle$ with one of the bound electrons promoted to a continuum state $|\boldsymbol{p}_e m_e\rangle$ with well defined asymptotic momentum $\boldsymbol{p}_e$ and a spin projection m_e. This process can be schematically represented as follow

$$|\alpha_i J_i M_i\rangle + 2\gamma(\omega) \to |\alpha_f J_f M_f\rangle + |\boldsymbol{p}_e m_e\rangle \,. \tag{2.9}$$

We consider the case, where the two photons $\gamma(\omega)$ originate from the same source, and therefore, posses not only the same energy, but also the same wavevector $\boldsymbol{k}$. According to the second-order perturbation theory, the transition amplitude describing the two-photon ionization process can be written as

$$\begin{aligned} M^{\lambda_1\lambda_2}_{J_i M_i J_f M_f m_e} &= \sum\!\!\!\!\!\!\int_\nu \frac{1}{E_{\alpha_i J_i} + \omega - E_{\alpha_\nu J_\nu}} \left\langle \alpha_f J_f M_f, \boldsymbol{p}_e m_e \left| \hat{\mathcal{R}}(\boldsymbol{k}, \lambda_2) \right| \alpha_\nu J_\nu M_\nu \right\rangle \\ &\times \left\langle \alpha_\nu J_\nu M_\nu \left| \hat{\mathcal{R}}(\boldsymbol{k}, \lambda_1) \right| \alpha_i J_i M_i \right\rangle . \end{aligned} \tag{2.10}$$

The evaluation of expression (2.10) requires a summation to be carried out over the complete spectrum of the intermediate states $|\alpha_\nu J_\nu M_\nu\rangle$. The operator $\hat{\mathcal{R}}$ denotes the one-particle transition operator describing the electron-photon interaction. This operator can be represented in the second quantization formalism (see e.g. [70]) as

$$\hat{\mathcal{R}}(\boldsymbol{k}, \lambda) = \sum_{n_1 n_2} \langle n_2 \left| \alpha_\mu A^\mu_\lambda(\omega) \right| n_1 \rangle \, a^\dagger_{n_2} a_{n_1} , \tag{2.11}$$

where $|n_1\rangle, |n_2\rangle$ are the single-electron initial and final states, $a^\dagger_{n_2}$ and a_{n_1} are the corresponding electron creation and annihilation operators, α_μ denotes the four-vector of the Dirac matrices, and $A^\mu_\lambda = (\phi_\lambda, \boldsymbol{A}_\lambda)$ is the photon wave function.

Due to the interaction of the atom with the two photons, an electron from a substate $|n_a \kappa_a m_a\rangle$ of the atom is promoted into a continuum state, leaving a hole (or vacancy) in the atomic subshell. We will refer to this electron as the *active electron*, as all other electrons remain in their original state. According to the particle-hole formalism, a state with a hole in a substate $|n_a \kappa_a m_a\rangle$ has angular momentum properties of a particle with total angular momentum j_a and its projection $-m_a$. Then, within the independent particle approximation, the final state after an ionization process is obtained by applying the electron creation ($a^\dagger_{\boldsymbol{p}_e m_e}$) and annihilation ($a_{n_a \kappa_a m_a}$) operators to the initial state and coupling the initial atom and hole angular momenta. Hence, the final state of the system can be expressed as

$$|\alpha_f J_f M_f, \boldsymbol{p}_e m_e\rangle = \sum_{m_a M} \langle j_a - m_a, J_i M \mid J_f M_f \rangle \, (-1)^{j_a - m_a} a^\dagger_{\boldsymbol{p}_e m_e} a_{n_a \kappa_a m_a} \, |\alpha_i J_i M\rangle \,. \tag{2.12}$$

We now have all necessary tools to simplify the transition amplitude from Eq. (2.10). First, we use the second-order quantization form of the electron-photon operator (2.11) to obtain

$$\begin{aligned} M^{\lambda_1\lambda_2}_{J_i M_i J_f M_f m_e} &= \langle \alpha_f J_f M_f, \boldsymbol{p}_e m_e | \sum_{n'_1 n'_2} \left\langle n'_2 \left| \alpha_\mu A^\mu_{\lambda_2}(\omega) \right| n'_1 \right\rangle a^\dagger_{n'_2} a_{n'_1} \frac{1}{\epsilon_{n_1} + \omega - \epsilon_{n_2}} \\ &\times \sum_{n_1 n_2} \left\langle n_2 \left| \alpha_\mu A^\mu_{\lambda_1}(\omega) \right| n_1 \right\rangle a^\dagger_{n_2} a_{n_1} \, |\alpha_i J_i M_i\rangle \,. \end{aligned} \tag{2.13}$$

Upon inserting the expression of the final many-electron state of our system in particle-

hole formalism (2.12), the transition amplitude takes the form

$$\begin{aligned} M^{\lambda_1\lambda_2}_{J_iM_iJ_fM_fm_e} &= \sum_{m_aM} \langle j_a - m_a, J_iM \mid J_fM_f\rangle\, (-1)^{j_a-m_a}\, \langle \alpha_i J_i M|\, a_{\boldsymbol{p}_e m_e} a^\dagger_{n_a\kappa_a m_a} \\ &\times \sum_{n_1'n_2'} \left\langle n_2' \left|\alpha_\mu A^\mu_{\lambda_2}(\omega)\right| n_1'\right\rangle a^\dagger_{n_2'} a_{n_1'} \frac{1}{\epsilon_{n_1}+\omega-\epsilon_{n_2}} \\ &\times \sum_{n_1n_2} \left\langle n_2 \left|\alpha_\mu A^\mu_{\lambda_1}(\omega)\right| n_1\right\rangle a^\dagger_{n_2} a_{n_1} \left|\alpha_i J_i M_i\right\rangle . \end{aligned} \tag{2.14}$$

Finally, carrying out the summation over all single electron states of the electron-photon operator as well as the momentum projection M, and the using the orthogonality of the wave functions leaves us with

$$\begin{aligned} M^{\lambda_1\lambda_2}_{J_iM_iJ_fM_fm_e} &= \sum_{m_a} (-1)^{j_a-m_a}\, \langle j_a - m_a, J_iM_i \mid J_fM_f\rangle \\ &\times \sum\!\!\!\!\!\!\int_n \frac{\left\langle \boldsymbol{p}_e m_e \left|\alpha_\mu A^\mu_{\lambda_2}(\omega_2)\right| n\right\rangle \left\langle n \left|\alpha_\mu A^\mu_{\lambda_1}(\omega_1)\right| n_a\kappa_a m_a\right\rangle}{\epsilon_{n_a\kappa_a}+\omega_1-\epsilon_{n_nj_n}}. \end{aligned} \tag{2.15}$$

It is apparent, that the utilization of independent particle approximation allowed us to reduce the many-electron transition amplitude to an amplitude which depends only on one-electron wave functions of the active electron. These one electron wave functions are the solutions of the Dirac (or Schrödinger) equation as discussed in Section 2.1.

2.2.1 Expansion of transition amplitudes

Further simplification of the one-electron transition amplitude can be achieved using the multipole decomposition of the photon field $\boldsymbol{A}_\lambda(\omega)$ into spherical tensors [71]

$$\boldsymbol{A}_\lambda(\omega) = 4\pi \sum_{JMp} i^{J-p} [\hat{\boldsymbol{\varepsilon}}_\lambda \cdot \boldsymbol{Y}^{(p)*}_{JM}(\hat{\boldsymbol{k}})] \boldsymbol{a}^{(p)}_{JM}(\boldsymbol{r}), \tag{2.16}$$

where $\boldsymbol{Y}^{(p)}_{JM}$ is a vector spherical harmonics and the index p describes the electric ($p=1$) and magnetic ($p=0$) components of the electromagnetic field. The vector functions $\boldsymbol{a}^{(p)}_{JM}(\boldsymbol{r})$ are referred to as multipole potentials and their exact form can be found for example in Ref. [70]. The dot product of the polarization vector with the vector spherical harmonics can be also written as [72]

$$[\hat{\boldsymbol{\varepsilon}}_\lambda \cdot \boldsymbol{Y}^{(p)}_{JM}(\hat{\boldsymbol{k}})] = \sqrt{\frac{[J]}{8\pi}} (-\lambda)^p D^J_{M\lambda}(\theta,\phi), \tag{2.17}$$

with the D-Wigner symbol $D^J_{M\lambda}(\theta,\phi)$. In this thesis, we will consistently choose the incident photon propagation direction along the quantization axis. In this way, the polar angles above $\theta = \phi = 0$ and we obtain (see Fig. 2)

$$[\hat{\boldsymbol{\varepsilon}}_\lambda \cdot \boldsymbol{Y}^{(p)}_{JM}(\hat{\boldsymbol{k}})] = \sqrt{\frac{[J]}{8\pi}} (-\lambda)^p \delta_{\lambda M}. \tag{2.18}$$

In addition to the multipole expansion, we also perform an expansion of the continuum electron wave function into its partial waves [73]

$$|\mathbf{p}_e m_e\rangle = \sum_{jm_j} \sum_{lm_l} i^l e^{-i\Delta_{jl}} \langle lm_l, 1/2 m_s \mid jm_j\rangle\, Y^*_{lm_l} \left|\epsilon_e \kappa m_j\right\rangle , \tag{2.19}$$

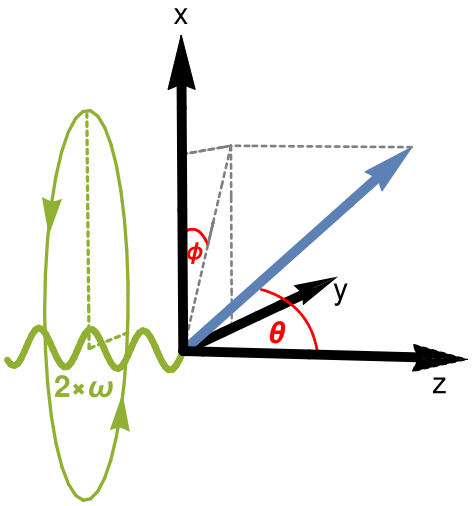

Figure 2: The considered geometry for two-photon ionization of atoms. The incident photons propagate along the quantization z axis, the linear part of polarization is along the x axis, and the photoelectron emission direction is determined by two angles θ and ϕ. This geometry is consistently used throughout the thesis.

with $\epsilon_e = \sqrt{\boldsymbol{p}_e^2 + m^2}$ being the photoelectron energy, Δ_{jl} the phase factor [73], and $Y^*_{lm_l}(\hat{\boldsymbol{p}}_e)$ the spherical harmonics that depend specifically on the direction of the emitted electron $\hat{\boldsymbol{p}}_e$). Individual wave functions $|\varepsilon_e \kappa m_j\rangle$ with given Dirac quantum number κ are called partial waves of the free electron with well-defined electron energy ε_e and quantum numbers j, l, and m_j. Inserting Eqs. (2.16), (2.18) and (2.19) into the expression (2.15) and applying Wigner-Eckart theorem (see appendix A) we obtain

$$\begin{aligned} M^{\lambda_1\lambda_2}_{J_i M_i J_f M_f m_e}(\kappa_a) &= 2\pi \sum_{m_a} (-1)^{j_a - m_a} \langle j_a - m_a, J_i M_i \,|\, J_f M_f \rangle \\ &\times \sum_{p_1 J_1} \sum_{p_2 J_2} \sum_{n_n j_n l_n m_n} i^{J_1 - p_1 + J_2 - p_2} \sqrt{\frac{[J_1, J_2]}{[j_n, j_a]}} (-\lambda_1)^{p_1} (-\lambda_2)^{p_2} \sum_{j m_j} \\ &\times \sum_{l m_l} (-i)^l e^{i\Delta_{jl}} \langle l m_l, 1/2 m_e \,|\, j m_j \rangle \, Y_{l,m_l}(\hat{\boldsymbol{p}}_e) \, \langle j m_j, J_2 - \lambda_2 \,|\, j_n m_n \rangle \\ &\times (-1)^{j - m_j} \sum_{m_a} \langle j_a, -m_a, J_i, M_i \,|\, J_f, M_f \rangle \, \langle j_n m_n, J_1 - \lambda_1 \,|\, j_a m_a \rangle \\ &\times \frac{\left\langle \epsilon_e \kappa \left\| \boldsymbol{\alpha} \cdot \boldsymbol{a}^{(p_2)}_{J_2} \right\| n_n \kappa_n \right\rangle \left\langle n_n \kappa_n \left\| \boldsymbol{\alpha} \cdot \boldsymbol{a}^{(p_1)}_{J_1} \right\| n_a \kappa_a \right\rangle}{\epsilon_{n_a \kappa_a} + \omega_1 - \epsilon_{n_n \kappa_n}}. \end{aligned} \tag{2.20}$$

To make our future analysis of two-photon ionization easier, we also integrate the reduced transition amplitudes $\left\langle f \left| \boldsymbol{\alpha} \cdot \boldsymbol{a}^{(p)}_J \right| i \right\rangle$ over angles. Performing the integration leaves us with

$$\left\langle n_f \kappa_f \left\| \boldsymbol{\alpha} \cdot \boldsymbol{a}^{(p)}_J \right\| n_i \kappa_i \right\rangle = \sqrt{\frac{[J](J+1)}{4\pi J}} (-1)^{j_i - j_f - J} [j_i]^{1/2} \langle j_i 1/2, J0 \,|\, j_f 1/2 \rangle \, R_{\kappa_f \kappa_i}(pJ), \tag{2.21}$$

where $R_{\kappa_i \kappa_f}$ is the radial integral given explicitly in Appendix C. We can now express the second-order amplitudes in terms of the radial integrals (2.21). Since these amplitudes will often appear in analyses of cross section in further chapters, we choose to use spectroscopic notation to represent these integrals for the sake of more intuitive understanding. Hence, the second order amplitude describing a specific quantum *ionization channel* (or equivalently *path*) $n_a \kappa_a \to n_n \kappa_n \to \epsilon_e \kappa$ (or in spectroscopic

notation $n_a l_{aj_a} \to n_n l_{n_{jn}} \to \epsilon_e l_j$) is

$$U_{l_j}^{(l_{njn})}(p_1 J_1 p_2 J_2) = \sum\!\!\!\!\!\!\int_n \frac{R_{\kappa\kappa_n} R_{\kappa_n\kappa_a}}{\epsilon_{n_a\kappa_a} + \omega - \epsilon_{n_n\kappa_n}}. \tag{2.22}$$

This amplitude describes a transition with multipolarities $p_1 J_1$ and $p_2 J_2$. As we will often restrict our analysis to electric dipole transition only, i.e. $J_1 = p_1 = J_2 = p_2 = 1$, it is practical to introduce a shorter notation $U_{l_j}^{(l_{njn})}$ which stands for $U_{l_j}^{(l_{njn})} = U_{l_j}^{(l_{njn})}(E1E1) = U_{l_j}^{(l_{njn})}(1111)$.

If we now consider the nonrelativistic limit, there is no fine-structure splitting. Under these circumstances, we assume that the radial wave functions representing different fine-structure levels can be considered equivalent. This leads to the equivalence of the transition amplitudes describing the corresponding fine structure ionization paths, e.g. $U_{p_{1/2}}^{(s_{1/2})} = U_{p_{3/2}}^{(s_{1/2})}$. In this limit, we can replace the amplitudes describing transition between fine-structure levels by a nonrelativistic amplitude, in terms of our previous example $U_{p_{1/2}}^{(s_{1/2})} = U_{p_{3/2}}^{(s_{1/2})} = U_p^{(s)}$. These nonrelativistic integral are given by

$$U_l^{(l_n)}(p_1 J_1 p_2 J_2) = \sum\!\!\!\!\!\!\int_n \frac{R_{ll_n} R_{l_n l_a}}{\epsilon_{n_a l_a} + \omega - \epsilon_{n_n l_n}}, \tag{2.23}$$

where the integrals $R_{l_f l_i}$ are the nonrelativistic equivalents to those shown explicitly in Appendix C. The amplitudes (2.22) and (2.23) are the key pieces for describing the two-photon ionization process. Each of these amplitudes describes one possible ionization channel and their relative values give raise to many intriguing phenomena in various observables which will be discussed in the next chapters. In order to prepare ourselves for the analysis of two-photon ionization cross sections and the properties of the produced photoion, it is reasonable to shortly discuss the number of the possible ionization paths which the above amplitudes describe as well as their basic properties.

Theoretically, there are infinitely many possible ionization channels. However, it is well known that electric dipole transitions generally dominate the light-matter interaction. Especially for higher-order processes, considering higher multipole channels results in steep rise in complexity of the analytical formalism. For these reasons, we will restrict our current discussion to electric dipole interaction only. Let us start exploring the possible two-photon ionization channels with considering ionization of s electrons. In this scenario, there are two possible intermediate angular momentum states and three final states, adding up to the total of five possible relativistic ionization channels. If the fine-structure of electron levels is neglected, the number of possible ionization channels reduces to only two nonrelativistic channels. The simplest way to count the possible ionization channels is to graphically represent them by following the selection and parity conservation rules. Figure 3 shows the schematic representation of the possible ionization channels for two-photon ionization of an s (left) or p (right) electron. Each fine-structure ionization channel is represented by a pair of arrows. If we neglected splitting of the levels due to the electron spin, the number of possible channels reduces. All the fine-structure channels with the same color reduce to one nonrelativistic channel. In 1985, Fano physically interpreted the propensity rules [74] first introduced by Berry [75] which state that all one-photon ionization transitions channels are not equally probable. Fano's propensity rule states that that out of the possible nonrelativistic channels, the one which increases the electron angular momentum is favoured due to increase of the centrifugal potential. The argument which arise from analysis of radial integrals surely also apply to many-photon ionization processes, similarly, as it was shown to apply for laser assisted ionization [76]. In our diagram 3,

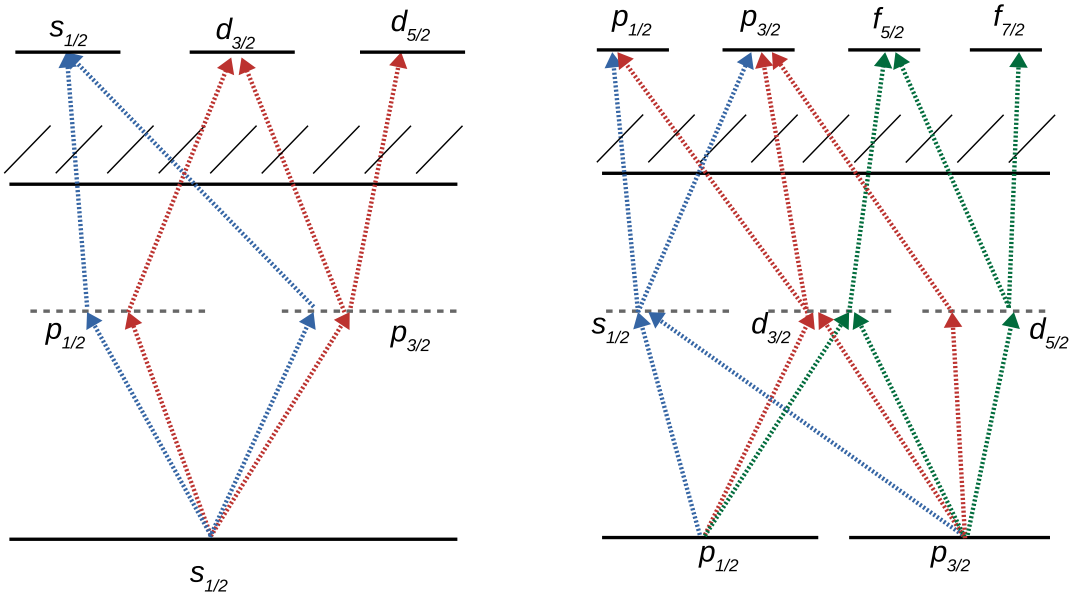

Figure 3: The possible two-photon ionization channels for ionization of s (left) or p (right) electrons. Each fine-structure ionization channel is represented by a pair of arrows. If we neglected splitting of the levels due to the electron spin, the number of possible channels reduces. All the fine-structure channels with the same color reduce to the same nonrelativistic channel.

this Fano's propensity rule would mean that the right-most channels generally dominate the ionization process. In later chapters, we will often return to this rule and explore the conditions, where this rule does not apply.

2.2.2 Nonlinear Cooper minimum

The transition amplitudes $U_{l_j}^{(l_{nj_n})}(p_1 J_1 p_2 J_2)$ describe the fundamental interaction of two photons with an atom. That is why it is worth to investigate them a little closer and try to unveil some of their properties. An important physical property these amplitudes describe is the case when the photon energy ω is comparable to a resonant electron transition, i.e. $\omega \approx \epsilon_{n_n l_n} - \epsilon_{n_a l_a}$. For a photon energy matching the resonance condition, the process can be treated sequentially since the sum over all intermediate states in (2.22) can be neglected as it is dominated by the resonant intermediate state. In this thesis, we will concentrate on cases, where the photon energy does not match any bound-bound resonant transition. However, an interesting behavior can be obtain if one tunes the photon energy between two such resonances. To understand what happens with the transition amplitude values between two resonances, let us return to Eq. (2.22). The expression shows, that all possible intermediate ionization paths contribute to the transition amplitude, and hence, we need to sum over the complete atomic spectrum. Now, consider a photon energy ω_{NCM} for which $\epsilon_{n\kappa} + \omega_{\mathrm{NCM}} - \epsilon_{\kappa_{n_1}} < 0$ and $\epsilon_{n\kappa} + \omega_{\mathrm{NCM}} - \epsilon_{\kappa_{n_2}} > 0$. We can therefore always *fine tune* the incident photon energy, such that contributions to the amplitudes from higher energy paths κ_{n_1} and

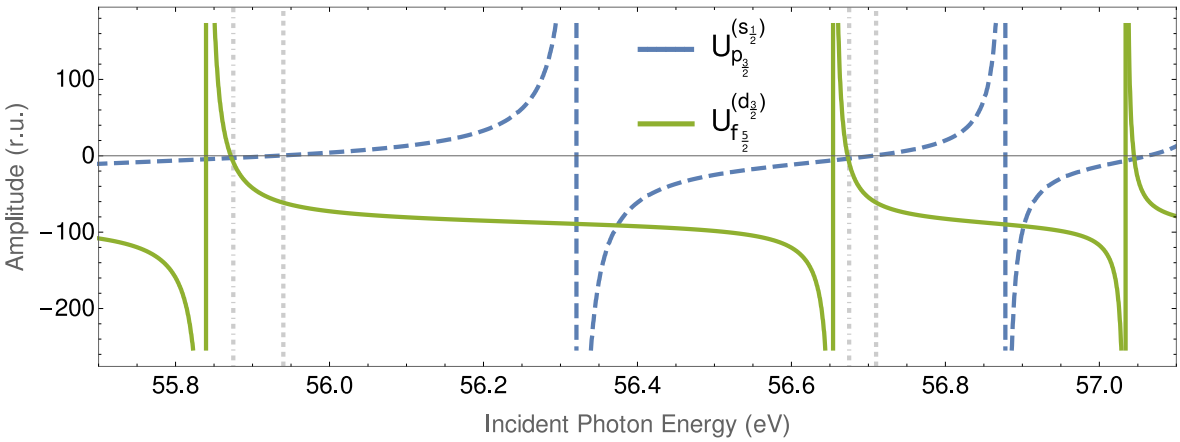

Figure 4: Electric dipole transition amplitude for two-photon ionization of $2p_{1/2}$ electron of neutral magnesium. It is clearly visible that generally, the $U_{f_{5/2}}^{(d_{3/2})}$ (solid green) ionization channel dominates the process, in accordance to the Fano's propensity rule [74]. There are two exceptions to this rule. One appears at photon energies matching the $p_{1/2} \to s_{1/2}$ resonance at which the $U_{p_{3/2}}^{(s_{1/2})}$ (dashed blue) dominates, the other at and near the nonlinear Cooper minimum, where the $U_{f_{5/2}}^{(d_{3/2})}$ channels passes through zero. Points where each of the displayed channels passes through zero are marked by gray dashed vertical lines.

from lower energy spectra κ_{n_2}

$$U_{\kappa_f}(\omega) = \sum\!\!\!\!\!\!\int_{\kappa_{n_1}}^{\epsilon_{\kappa n_1} > \epsilon_{n\kappa}+\omega} \frac{\langle \epsilon_e \kappa_f || \mathbf{r} || \kappa_{n_1} \rangle \langle \kappa_{n_1} || \mathbf{r} || n\kappa \rangle}{\epsilon_{n\kappa} + \omega_{\mathrm{NCM}} - \epsilon_{\kappa_{n_1}}} + \sum\!\!\!\!\!\!\int_{\kappa_{n_2}}^{\epsilon_{\kappa n_2} < \epsilon_{n\kappa}+\omega} \frac{\langle \epsilon_e \kappa_f || \mathbf{r} || \kappa_{n_2} \rangle \langle \kappa_{n_2} || \mathbf{r} || n\kappa \rangle}{\epsilon_{n\kappa} + \omega_{\mathrm{NCM}} - \epsilon_{\kappa_{n_2}}}, \tag{2.24}$$

exactly balance each other out, i.e. $U_{\kappa_f}(\omega_{\mathrm{NCM}}) = 0$. This energy describes passing of the otherwise dominant channel through zero, and hence, we call this point the *nonlinear Cooper minimum* (NCM). Such nonlinear Cooper minimum can be found between any two adjacent level resonances of the same angular momentum. Furthermore, this is a general feature of two-(or even multi-)photon ionization. If an initially bound electron in $n\kappa$ shell absorbs multiple photons, nonlinear Cooper minimum can be found between any pair of $n'(j+1)$ and $(n'+1)(j+1)$ resonances.

To graphically illustrate the nonlinear Cooper minimum and the dynamic behaviour of the transition amplitudes in the vicinity, we present Fig. 4. The figure shows two relativistic ionization channels for two-photon ionization of $p_{1/2}$ electron of neutral magnesium atom, $U_{f_{5/2}}^{(d_{3/2})}$ (solid green) and $U_{p_{3/2}}^{(s_{1/2})}$ (dashed blue). As the channel $U_{f_{5/2}}^{(d_{3/2})}$ possesses higher angular momentum, it generally dominates the process as predicted by Fano [74]. However, there are two types of exceptions to this rule. For example, when the incident photon energy matches the $p_{1/2} \to s_{1/2}$ resonance, where the $U_{p_{3/2}}^{(s_{1/2})}$ is strongly increased due to the denominator of the transition amplitude (2.22). Another point is where the sign of the dominant channel $U_{f_{5/2}}^{(d_{3/2})}$ changes, and therefore, passes through zero. The photon energy at which the dominant channel vanishes is called the nonlinear Cooper minimum. The photon energies at which each of the displayed channels passes through zero are marked by gray dashed vertical lines.

The significance of nonlinear Cooper minima can be better understood upon their

comparison with other known effects in different processes which contributed to accurate understanding of atomic processes. First of all, they can be considered as nonlinear equivalents of the Cooper minima in one-photon ionization process [59, 60], since in both cases vanishing of the dominant ionization channel strongly influences observable quantities. In one-photon ionization processes, Cooper minima have opened the door for accurate comparison of theory with experiment e.g. [77, 78], or even allowed to resolve relativistic effects in photoelectron angular distributions or ionization time delay [46, 62, 79–81]. The nonlinear Cooper minima also share similar characteristics with the tune-out wavelengths, specific photon energies at which the atomic polarizability vanishes. Their exact energy positions are sensitive even to small contributions such as finite nuclear mass effect, or relativistic and QED corrections [82–84]. Similarly to both above examples, Cooper resonances have the potential to push the accuracy at which we understand nonsequential nonlinear process beyond current possibilities. It is worth noting that due to their physical origin, nonlinear Cooper minima are imprinted in practically all observables of the two-photon ionization process.

2.2.3 Numerical evaluation of the transition amplitudes

From the theoretical description above, it becomes clear that the main computation challenge lies in the infinite summations of the radial matrix elements (2.22) over all multipole orders and infinite number of intermediate states. To deal with this numerically, the infinite summations over the multipoles of each of the two photons were restricted to a maximum value of $J_{\max} = 5$. This limit is sufficient to obtain convergence of the transition amplitudes at less than 0.001% level. To sum over the infinite number of intermediate states, finite basis-set [85] constructed from B-splines by applying the dual-kinetic-balance approach [86] was employed. This technique allows us to reduce infinite sum over the intermediate states in (2.22) to finite sum over pseudospectrum. This approach has been previously successfully applied, for example, in the calculations of two-photon decay rates of heliumlike ions [87, 88] or cross sections of x-ray Rayleigh scattering [89]. The continuum-state wave functions were obtained by numerical solutions of the Dirac equation with help of the RADIAL package [90].

In order to account for the screening effects, we solve the Dirac equation with a screening potential, which partially accounts for the inter-electronic interaction, as described in previous subsection. We use number of different potentials, which correspond to a potential created by all bound electrons except of the active electron. Unless otherwise specified, we use the core-Hartree potential which reproduces the electron binding energies of the presented examples in a very good agreement with the experimental values [91]. To analyse the sensitivity to the choice of potential, in addition to the core-Hartree potential, five different screening potentials were also used. The potential taken from Ref. [92], to which we refer as the "Salvat" potential and Salvat potential modified in a way to reproduce experimental binding energies $E_{\rm bind}^{\rm exp}$, referred to as "Salvat $E_{\rm bind}^{\rm exp}$". The Perdew-Zunger, Kohn-Sham and Slater screening potentials were also used [93–95] in order to estimate uncertainty or reconstruction of the electron spectra. In general, all the screening potentials agree with each other within 10%. Any deviation from this value will be reported, where appropriate.

Additionally, in order to check the consistency of our results, we carried out most of our calculations in length and velocity gauges. The results for both gauges were in a perfect agreement as expected for any local potential. Even though the agreement of the two gauges does not prove validity of the results, it shows that the effective single-electron amplitudes (2.22) are properly implemented in our codes.

2.3 Density matrix formalism

2.3.1 The concept of density matrix theory

Density matrix theory offers the most convenient and elegant theoretical framework for the fields of polarization and angular correlation studies of ionic states following excitation and ionization processes, or studies of subsequent processes such as emission of fluorescence photons. Within the density matrix theory, an atomic (or molecular) state of a physical system can be efficiently described no matter if it is in a pure quantum state or in a mixture of different states with any degree of coherence. The basic idea of density matrix theory is to propagate such an ensemble through an interaction process, starting from a well-defined initial state and by passing through one or, possibly, several intermediate states until the final state of the is accomplished.

The notion of density matrix was originally introduced in 1927 by a Hungarian-American scientist John von Neumann to describe statistical concepts in quantum mechanics [96]. After that, for quite a long period of time the use of the density matrix has been mainly restricted to statistical physics. However, it was thirty years later, that the idea of density matrices started to be used in other fields, such as solid state physics, laser physics, atomic and molecular physics [97]. Since then, density matrix approaches has been described in detail and used in scientific literature (often used books in atomic physics are e.g. those from Blum or Balashov [72, 98]) as well as in atomic physics research, for example to characterize the polarization properties of fluorescence photons after inner-shell photoionization [99, 100], or to study photoexcitation of magnetic sublevels of an atom by twisted light [101], or to analyze radiative electron polarization in strong laser fields [102]. Recently, it has also been demonstrated, that individual elements of the density matrix describing a general quantum system can be experimentally extracted by a sequence of measurements [103].

Since density matrix theory has been extensively described before (Ref. [98] provides an excellent introduction, while [72] puts the theory to practice in atomic physics), we will not repeat the basics here and introduce only those parts, relevant to two-photon ionization process. As we will be concerned with interaction of photons with atoms, the description of photon density matrix is unavoidable. Furthermore, we will return to the photon density matrix in chapter 6 to study the physical properties of fluorescence light. Having introduced the photon density matrix, we come to derivation of the density matrix describing the state of a system consisting of a singly charged ion and a photoelectron after two-photon ionization. We will repeatedly return to this final state density matrix throughout this thesis to analyze the observable properties of both, the photoelectron and the photoion.

2.3.2 Photon density matrix

In quantum mechanics, photons are the particle equivalents of the electromagnetic field. Photons have intrinsic spin of 1 and posses zero rest energy. The lack of rest mass results in a unique feature of photons, which is that the photon spin projection λ onto the its wave vector $\boldsymbol{k}$ (called *helicity*) can take only one of two values, $\lambda = \pm 1$. Helicity, therefore offers a convenient basis to characterize the photon polarization state. In the helicity basis, the two-dimensional photon density matrix can be written in terms of so-called *Stokes parameters*, which fully characterize the photon polarization

$$\langle \mathbf{k}\lambda \,|\hat{\rho}_\gamma|\, \mathbf{k}\lambda' \rangle = \frac{1}{2}\begin{pmatrix} 1+P_3 & P_1 - iP_2 \\ P_1 + iP_2 & 1-P_3 \end{pmatrix} \tag{2.25}$$

$$= \frac{1}{2}\Big(\delta_{\lambda\lambda'}(1+\lambda P_3) + (1-\delta_{\lambda\lambda'})(P_1 - i\lambda P_2)\Big). \tag{2.26}$$

In this parametrization, the first line (and column) of the photon density matrix corresponds to $\lambda = 1$ and the second one to $\lambda = -1$. The two Stokes parameters P_1 and P_2 describe the degree (and direction) of linear polarization of the photon in the plane perpendicular to the wave vector $\boldsymbol{k}$ and P_3 specifies the photon's degree of circular polarization. The beam is said to be purely polarized if $P_1^2 + P_2^2 + P_3^2 = 1$ and unpolarized when all Stokes parameters are equal to zero.

In an experiment, the Stokes parameters can be determined by measuring the intensities $I(\theta)$ of the light which is linearly polarized under particular angle θ with regard to the plane defined by the incoming beam and emitted light. The three parameters can be then written as

$$\begin{aligned} P_1 &= \frac{I(0^\circ) - I(90^\circ)}{I(0^\circ) + I(90^\circ)} \\ P_2 &= \frac{I(45^\circ) - I(135^\circ)}{I(45^\circ) + I(135^\circ)} \\ P_3 &= \frac{I(\lambda = 1) - I(\lambda = -1)}{I(\lambda = 1) + I(\lambda = -1)}. \end{aligned} \tag{2.27}$$

In this thesis, we consistently use the incident photon beam to propagate along the quantization z axis and the linear part of polarization to be along the x axis . With such choice of geometry it makes sense to use only one Stokes parameter to describe the degree of linear polarization. For the sake of generality, we still define this parameter in terms of P_1 and P_2 and rename the P_3 parameter as

$$\begin{aligned} P_l &= \sqrt{P_1^2 + P_2^2} \\ P_c &= P_3. \end{aligned} \tag{2.28}$$

We will consistently use the Stokes parameters (2.28) to describe the polarization of the incoming beam. However, in chapter 5 of this thesis, we will analyse the polarization properties of fluorescence photons following two-photon ionization. To easily distinguish between the polarization properties of the incident and fluorescence photons, we will keep the notation (2.27) for the characterization of fluorescence polarization properties.

2.3.3 Characterization of an atomic state following two-photon ionization

Having introduced the concept of density matrix theory, we can now proceed to characterize the state of an atomic system after being ionized by simultaneous absorption of two photons. First, we need to describe initial state of our system, which consists of an atom and two photons. Since all three particles are initially independent, adopting the previously introduced notation we can write the initial density matrix as

$$\begin{aligned} \langle \alpha_i J_i M_i, \boldsymbol{k}\lambda_1 \boldsymbol{k}\lambda_2 \left| \hat{\rho}_{i+2\gamma} \right| \alpha_i J_i M_i', \boldsymbol{k}\lambda_1' \boldsymbol{k}\lambda_2' \rangle &= \langle \alpha_i J_i M_i \left| \hat{\rho}_i \right| \alpha_i J_i M_i' \rangle \langle \boldsymbol{k}\lambda_1 \left| \hat{\rho}_\gamma \right| \boldsymbol{k}\lambda_1' \rangle \\ &\times \langle \boldsymbol{k}\lambda_2 \left| \hat{\rho}_\gamma \right| \boldsymbol{k}\lambda_2' \rangle . \end{aligned} \tag{2.29}$$

Generally, we will assume that the initial atom is unpolarized. In such a case, the density matrix operator of the initial atomic state averages over the magnetic quantum numbers and can be written as

$$\langle \alpha_i J_i M_i \left| \hat{\rho}_i \right| \alpha_i J_i M_i' \rangle = \frac{1}{[J_i]} \delta_{M_i M_i'}. \tag{2.30}$$

After absorption of the two photons, one of the atomic electrons is promoted to continuum and the produced photoion is in a singly-charged state. The density matrix of

the composite system is given by

$$\begin{aligned}\left\langle \alpha_f J_f M_f, \boldsymbol{p}_e m_e \left| \hat{\rho}_f \right| \alpha_f J_f M'_f, \boldsymbol{p}_e m'_e \right\rangle &= \sum_{M_i \lambda_1 \lambda_2} \sum_{M'_i \lambda'_1 \lambda'_2} M^{\lambda_1 \lambda_2}_{J_i M_i J_f M_f m_e} M^{\lambda'_1 \lambda'^{*}_2}_{J_i M'_i J_f M'_f m'_e} \\ &\times \left\langle \alpha_i J_i M_i, \boldsymbol{k} \lambda_1 \boldsymbol{k} \lambda_2 \left| \hat{\rho}_{i+2\gamma} \right| \alpha_i J_i M'_i, \boldsymbol{k} \lambda'_1 \boldsymbol{k} \lambda'_2 \right\rangle , \end{aligned} \tag{2.31}$$

where the transition amplitudes $M^{\lambda_1 \lambda_2}_{J_i M_i J_f M_f m_e}$ describing the interaction of the electron with the two photons are explicitly given by Eq. (2.10). With appropriate prefactors, the density matrix gives the cross section of the two-photon ionization process. The derivation of these prefactors is provided in the Appendix B. In most examples in this thesis, we will study two-photon inner-shell ionization of neutral atoms. The produced photoion is in this case in an singly-charged excited state which would undergo a subsequent relaxation. Emission of a fluorescence photon as a type of a possible subsequent process will be discussed in chapter 6.

The density matrix (2.31) is the key expression of interest in this thesis. It describes the final state of our system (photoion + photoelectron) and the aim of each chapter will be to analyze different components of this density matrix in detail. Although we are considering only two-photon ionization where the photon energy is lower than the binding energy of the active electron (i.e. $\omega < \epsilon_{n_a \kappa_a}$), all our general theoretical description is also applicable for above-threshold ionization.

3 Two-Photon Ionization Cross Sections

Consider an atomic target irradiated with a strong laser beam with an electron detectors placed near the target. The detector will yield a certain count of photoelectrons which were ionized from the target. If we now increase the number of atoms in the target, or number of photons in the laser beam, the photoelectron yield we measure becomes greater than before. This yield, therefore, depends on number of experimental parameters, and does not reflect the fundamental probability of a given process. In order to avoid these dependencies and to describe the probability of the fundamental ionization process, a quantity called cross section is often defined. The cross section for absorption of N photons from a beam with photon flux F and pulse of duration τ in an interaction region that contains n atoms is then given by $\sigma^{(N)} = Y^{(N)}/(F^N \tau n)$. The units of the cross section describing the absorption of N photons by a single atom $\sigma^{(N)}$ are $\mathrm{cm}^{2N}\mathrm{s}^{N-1}$. In this section, we describe the total (angle-integrated) cross sections for two-photon ionization of atoms. We first derive a general expression of the cross section from the density matrix of Eq. (2.31). Afterwards we obtain explicit analytical cross section expressions for two-photon ionization of atomic s and p orbitals, and analyze their dependency on the incident photon energy and polarization, evaluate the importance of relativistic description of the ionization process and discuss the current experimental efforts which aim to determine the total two-photon ionization cross sections.

3.1 General form of the total cross section

In the previous chapter, we derived the density matrix of the final state of an atom after one of its electrons was ionized by the absorption of two photons. This density matrix fully describes all properties of the system. We can, therefore, extract all necessary information to obtain the total two-photon ionization cross section which expresses the probability to ionize an electron from a specific atomic shell. This cross section accounts for detection of photoelectrons at all angles and of any ion and electron magnetic state. The total two-photon ionization cross section can be simply obtained from the general scattering formula (see the Appendix B) and by tracing out all degrees of freedom of the photoelectron and summing over all possible final states of the photoion of Eq. (2.31). The total two-photon ionization cross section is given by

$$\begin{aligned}
\sigma_{l_a j_a}(\omega) &= \frac{8\pi^3\alpha^2}{\omega^2} \sum_{J_f M_f m_e} \int d\Omega_{\hat{\boldsymbol{p}}_e} \left\langle \alpha_f J_f M_f, \boldsymbol{p}_e m_e \left| \hat{\rho}_f \right| \alpha_f J_f M_f, \boldsymbol{p}_e m_e \right\rangle \qquad (3.1) \\
&= \frac{8\pi^3\alpha^2}{\omega^2} \frac{1}{[J_i]} \sum_{\substack{\lambda_1\lambda_2 \\ \lambda_1'\lambda_2'}} \left\langle \boldsymbol{k}\lambda_1 \left| \hat{\rho}_\gamma \right| \boldsymbol{k}\lambda_1' \right\rangle \left\langle \boldsymbol{k}\lambda_2 \left| \hat{\rho}_\gamma \right| \boldsymbol{k}\lambda_2' \right\rangle \sum_{\substack{J_f M_f \\ M_i m_e}} \int d\Omega_{\hat{\boldsymbol{p}}_e} \\
&\times \; M^{\lambda_1\lambda_2}_{J_i M_i J_f M_f m_e}(\kappa_a) M^{\lambda_1'\lambda_2'*}_{J_i M_i J_f M_f m_e}(\kappa_a).
\end{aligned}$$

As this work discusses two-photon ionization process only, we consistently use the short notation for any cross section $\sigma(\omega) = \sigma^{(2)}(\omega)$. Moreover, we use spectroscopic notation in the subscript $\sigma_{l_a j_a}(\omega)$ to indicate the initial angular momentum of the active electron. Since the two-photon ionization is a second-order process, its cross section has the units of $[L^4T]$.

We can further simplify the above total cross section by utilizing the expression of the transition amplitude (2.20). Owing to the separation of radial and angular parts of the electron wave functions, it is possible to carry out the angular integration and

summation over photoelectron spin projections analytically to obtain

$$\sigma_{l_a j_a}(\omega) = \frac{8\pi^3\alpha^2}{\omega^2} \sum_{\substack{\lambda_1\lambda_2 \\ \lambda_1'\lambda_2'}} \langle \boldsymbol{k}\lambda_1 \,|\hat{\rho}_\gamma|\, \boldsymbol{k}\lambda_1' \rangle \, \langle \boldsymbol{k}\lambda_2 \,|\hat{\rho}_\gamma|\, \boldsymbol{k}\lambda_2' \rangle \sum_{\kappa m_j} T^{\lambda_1\lambda_2}_{\kappa m_j}(\kappa_a) T^{\lambda_1'\lambda_2'*}_{\kappa m_j}(\kappa_a), \tag{3.2}$$

where the simplified transition amplitude takes the form

$$\begin{aligned} T^{\lambda_1\lambda_2}_{\kappa m_j}(\kappa_a) &= 2\pi \sum_{p_1 J_1} \sum_{p_2 J_2} \sum_{\substack{n_n j_n \\ l_n m_n}} i^{J_1 - p_1 + J_2 - p_2} \sqrt{\frac{[J_1, J_2]}{[j_n, j_a]}} (-\lambda_1)^{p_1} (-\lambda_2)^{p_2} \\ &\times (-1)^{j-m_j} \, \langle j m_j, J_1 - \lambda_1 \,|\, j_n m_n \rangle \, \langle j_n m_n, J_2 - \lambda_2 \,|\, j_a m_a \rangle \\ &\times \frac{\left\langle \varepsilon_e j l \left\| \boldsymbol{\alpha} \cdot \boldsymbol{a}^{(p_1)}_{J_1} \right\| n_n j_n l_n \right\rangle \left\langle n_n j_n l_n \left\| \boldsymbol{\alpha} \cdot \boldsymbol{a}^{(p_2)}_{J_2} \right\| n_a j_a l_a \right\rangle}{\epsilon_{n_a j_a l_a} + \omega - \epsilon_{n_n j_n l_n}}. \end{aligned} \tag{3.3}$$

Owing to the single-particle approximation and the summation over all possible final states of the atom, all dependencies on the many-electron quantum numbers vanish for the calculation of the total cross section.

Although the above expression is significantly simplified, it is still generally difficult to deduce any properties of the two-photon ionization process without a rigorous calculation. In the following subsection, we will consider two-photon ionization of specific electron shells and apply further approximations in order to obtain a more intuitive analytical expressions. However, equation (3.2) will be used in future for calculation of exact total cross section, without further simplifications.

3.2 Analysis of ionization of specific shells

In this subsection, we will study two-photon ionization of s and p electrons. Specifying the initial angular properties of the active electron and applying the electric dipole approximation allows us to write the total cross section expression 3.2 in a much more compact and intuitive form. Both of the above mentioned assumptions are generally well justified. It is generally easy to determine the initial state of an electron in an experiment from the measured photoelectron energy spectra by the photoelectron energy. Furthermore, the assumption that the electric dipole transition is the strongly dominant contribution to the process is known [70, 104] and becomes invalid only under special circumstances [46, 62, 79]. The contributions of higher multipoles, and hence the validity of the electric dipole approximation, will be evaluated in section 3.2.3.

3.2.1 Ionization of s electrons

The main motivation to study the two-photon ionization of s electrons arose from the possibility to ionize the K shell electrons with multiple photons at the free-electron laser facilities. The two-photon ionization of the most deeply bound electrons is in particular of interest in the field of nonlinear spectroscopy [24–27], where the ionization of the K shell electron of solids is studied through the detection of the subsequent fluorescence. However, it is not only these heavy complex atoms that are of interest. Free-electron lasers also give us the opportunity to investigate nonlinear processes in one of the simplest atomic systems, gaseous helium. Although helium nucleus is orbited by only two-electrons, recent experiments [45] demonstrate that even this relatively simple atomic system has some surprising properties in store, waiting for us to discover them.

To unveil the characteristics of two-photon ionization of s electrons, we derive the relativistic total cross section within electric dipole approximation. Afterwards, we make a further simplification and reduce the derived expression to nonrelativistic limits. Let us start with Eq. (3.2) and choose the initial state to be an s electron, i.e. $\kappa_a = -1$ (or $j_a = 1/2$, $l_a = 0$) and $m_a = \pm 1/2$. Moreover, since we restrict the electron-photon interaction to electric dipole only, we have $J_1 = J_2 = p_1 = p_2 = 1$. For simplicity, let us also assume that the incident photons are purely polarized, which means that $P_l^2 + P_c^2 = 1$. This assumption is well justified since the beam produced at free-electron laser facilities do reach high purity of polarization. By performing the above mentioned assumptions and carrying out all summation of Eq. (3.2), we obtain

$$\sigma_{s_{1/2}}^{(\mathrm{rel.})} = \frac{4\pi^3\alpha^2}{25\omega^2}\Big[25(1-P_c^2)U_{s_{1/2}}^2 + (2+P_c^2)\big[U_{d_{3/2}}^2 + 54U_{d_{5/2}}^2\big]\Big], \tag{3.4}$$

where $U_{s_{1/2}} = (U_{s_{1/2}}^{(p_{1/2})} + U_{s_{1/2}}^{(p_{3/2})})$, $U_{p_{3/2}} = (5U_{d_{3/2}}^{(p_{1/2})} + U_{d_{3/2}}^{(p_{3/2})})$, and $U_{d_{5/2}} = U_{d_{5/2}}^{(p_{3/2})}$ are the radial transition amplitudes from Eq. (2.22). From the above expression, it becomes apparent that only interference from ionization channels with the same final state contribute to the total cross section. As a consequence, the dependence on the photoelectron phase vanishes and hence, this information cannot be accessed by measuring the total cross section. From the above expression, we can already deduce some interesting features. For example, the dependency of the total cross section and number of ionization channels on the photon polarization. If we ionize our atom with pure circularly polarized light, the ionization channel $U_{s_{1/2}}$ vanishes. This is because the a photon with helicity $\lambda = \pm 1$ increases (or decreases) the projection of the electron's angular momentum by unity. This means that after absorption of two such photons, the electron cannot posses smaller absolute value of projection of angular momentum than 3/2, i.e. $|m_j| \geq 3/2$. This restriction can be also seen from the first term of the above expression, which vanishes whenever $P_c = \pm 1$.

The above expression is relativistic (within electric dipole approximation), however, in many situations it is reasonable to neglect relativistic effect, such as wave function contraction or fine-structure splitting, and carry out the calculations nonrelativistically (see Sec. 2.2.1 and Fig. 3 in particular). For weakly bound electrons, the ionization paths for different fine-structure levels are approximately equivalent, i.e. $U_{s_{1/2}}^{(p_{1/2})} \approx U_{s_{1/2}}^{(p_{3/2})} \approx U_s^{(p)}$, and $U_{d_{3/2}}^{(p_{1/2})} \approx U_{d_{3/2}}^{(p_{3/2})} \approx U_{d_{5/2}}^{(p_{3/2})} \approx U_d^{(p)}$. In this nonrelativistic limit, we can derive the total cross section analogous to Eq. (3.4) to

$$\sigma_s^{(\mathrm{nonrel.})} = \frac{18\pi^3\alpha^2}{5\omega^2}(5(1+P_l^2-P_c^2)|U_s^{(p)}|^2 + (7+P_l^2+5P_c^2)|U_d^{(p)}|^2), \tag{3.5}$$

where we no longer assume that the incident photons are fully polarized. If we persist with this assumption, we can reduce the above expression to the one obtained by Manakov *et al.* [105]. As before, we can see that the ionization channel $U_s^{(p)}$ vanishes for the case of ionization by pure circularly polarized light. Moreover, the above equation also reveals, that the total cross section is larger for ionization by circularly than with linearly polarized light [3]. This is one of the differences from the well-known one-photon ionization, where the total cross section generally does not depend on the photon polarization. The dependence of the total cross section on the photon polarization can, therefore, be considered to be a nonlinear effect. The importance of the relativistic effects, and hence the difference between Eq. (3.4) and (3.5) will be analyzed in section 3.2.3.

Let us now utilize the fully relativistic expression for the total two-photon ionization cross section and study the dependence of the total cross section on the incident photon

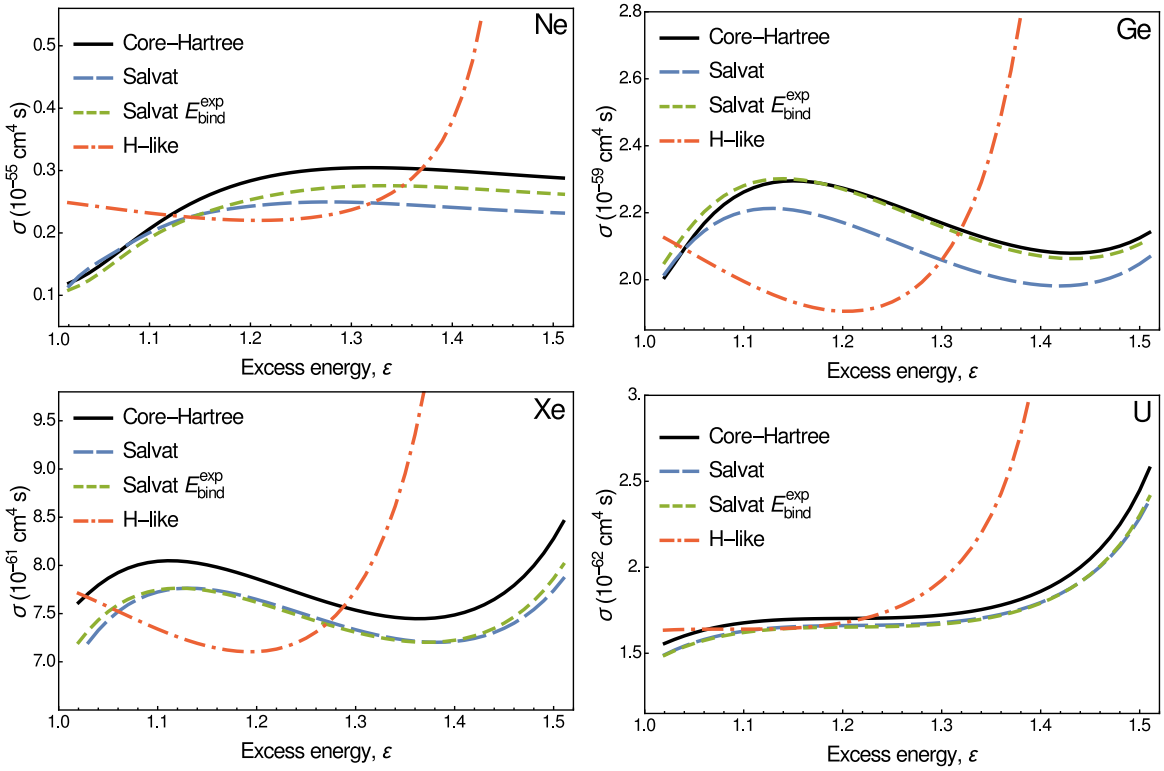

Figure 5: The total two-photon K-shell ionization cross section $\sigma_{s_{1/2}}^{(\rm rel)}$ as a function of excess energy ε (two-photon energy in units of K-shell binding energy) for ionization by linearly polarized photons. Results are shown for the two-photon ionization of hydrogen-like (dash-dotted red) ions and neutral atoms calculated in three different potentials: core-Hartree (solid black), Salvat (long-dashed blue) as well as Salvat $E_{\rm bind}^{\rm exp}$ (short-dashed green) potentials. Calculations were performed for neon, germanium, xenon, and uranium atoms (as labelled).

energy. Although the formalism derived in this section applies generally for neutral atoms as well as ions, detailed calculations have been carried out for two-photon K-shell ionization of neutral neon, germanium, xenon, and uranium atoms. We will compare cross sections for K-shell ionization of hydrogen-like and neutral atoms as well as the sensitivity to the choice of a screening potential used in the calculation of the electron wave functions (see Sec. 2.2.3). Since there are two electrons in the K-shell of neutral atoms but only one electron in the K-shell hydrogen-like ions, we introduce an additional factor of two in the hydrogen-like calculation for the sake of comparison. We start by comparing the total two-photon ionization cross sections for ionization of hydrogen-like and neutral atoms in terms of so called *excess energy*. Excess energy represents the (combined) energy of the two photons in units of binding energy of the active electron, i.e., $\varepsilon = 2\omega/\epsilon_{\rm bind}$. Figure 5 presents the total cross sections for two-photon ionization of neutral (solid black) as well as for hydrogen-like (dashed-dotted red) neon, germanium, xenon, and uranium by linearly polarized photons. One can notice that the first resonant behaviour (sharp increase) in the total cross section occurs in lower excess energy for hydrogen-like ions than for neutral atoms. This resonant behaviour occurs when the single photon energy reaches the $1s \to 2p$ transition energy. Although the $2p$ state is generally occupied for neutral atoms, the resonant two-photon ionization can be understood as follows. The $2p$ electron is ionized by the first photon and the corresponding vacancy is then filled by excitation of the $1s$ electron by the second photon.

The more significant difference between neutral and hydrogen-like systems lies in the decrease of the total cross section towards the ionization threshold. This cross section

reduction is strongest for elements with nuclear charge $Z = 7 - 12$ and becomes much less significant for heavy atoms. In the case of hydrogen-like ions, no such behaviour has been predicted and the total two-photon ionization cross section is slowly decreasing in nonresonant energy regions [30, 31], which we also confirm in the present calculations. We can therefore conclude that the change of the total cross section for light neutral elements close to the ionization threshold can be directly linked to the deviation of the binding potential from the Coulomb potential created by the nucleus. These so called *screening effects* reduce the amplitude of the dominant ionization channel near the two-photon ionization threshold, and hence, decrease the value of the total cross section [64].

Figure 5 also shows the comparison of the total two-photon ionization cross section obtained using three screening potentials (solid black, dashed green, and blue curves) introduced in Sec. 2.2.3. We see that for low-Z and medium-Z atoms, the core-Hartree and Salvat potentials differ in the magnitudes of the total cross section by less than 25%. This is partially caused by the calculated value of the binding energy. When the Salvat potential was modified to reach perfect agreement with the experimental binding energies, the cross section difference from the core-Hartree calculation was reduced to about 10%. Therefore, even though part of the difference between the cross sections as predicted by each potential arises from the difference of binding energies, the distinct potential formulations also result in a deviation. Despite the small magnitude differences, all screening potentials predict similar energy dependence of the total cross section. The agreement of these potentials justifies that the obtained behaviour and magnitude is not very sensitive to the choice of potential. We ascribe the difference between the core-Hartree and Salvat calculations as an uncertainty of presented results. The uncertainty decreases from 25% for Ne to 10% for U. We restrict all further discussion to the use of core-Hartree potential.

To gain deeper understanding of the total cross section results, we now look only at the $E1E1$ ionization channels which dominate the ionization process. In this approximation, only the $J = 1$ and $p = 1$ multipole of each of the two photons is considered. Since we are interested in ionization of a $1s$ electron with zero orbital angular momentum $l = 0$, $E1E1$ transition allows only two possible ionization channels; $s \to p \to s$ and $s \to p \to d$ (see Fig. 3). Therefore, only s and d partial waves of the free electron are allowed in dipole approximation. While both of these channels are open for linear and unpolarized light, only the $s \to p \to d$ channel is open for circularly polarized light. This restriction comes from the conservation of the angular momentum projection. Since we are considering two equally circularly polarized photons, the angular momentum projection must change by ± 2, then $|m_j| > 1/2$ is always the case, making the final s state forbidden. This is a point worth remembering. As we will soon see, the absence of the $s \to p \to s$ channel leads to a magnification of the screening effects, which increases the probability of experimental detection of these effects.

Figure 6 shows the plots of the partial-wave cross sections considering only the s or d partial-waves of the continuum electron as a function of excess energy. Results are presented for ionization of hydrogen-like (dash-dotted red and short-dashed orange) and neutral (solid black and long-dashed green) neon, germanium, xenon, and uranium atoms by linearly polarized light. We can see that the energy dependence of the partial-wave cross section of hydrogen-like ions fulfils our expectation we gained from Fig. 5. The cross sections of $s \to p \to d$ channel always dominates the $s \to p \to s$ channel and the two curves remain approximately parallel. Analogously to the total cross section, both channels can be considered constant in nonresonant energy region up to the proximity of the $1s \to 2p$ resonant energy. Similar behaviour can be seen in the case of neutral uranium. However, for neutral atoms with lower nuclear charge, we observe a competition of the two partial waves in near-threshold energy region. A drop of the

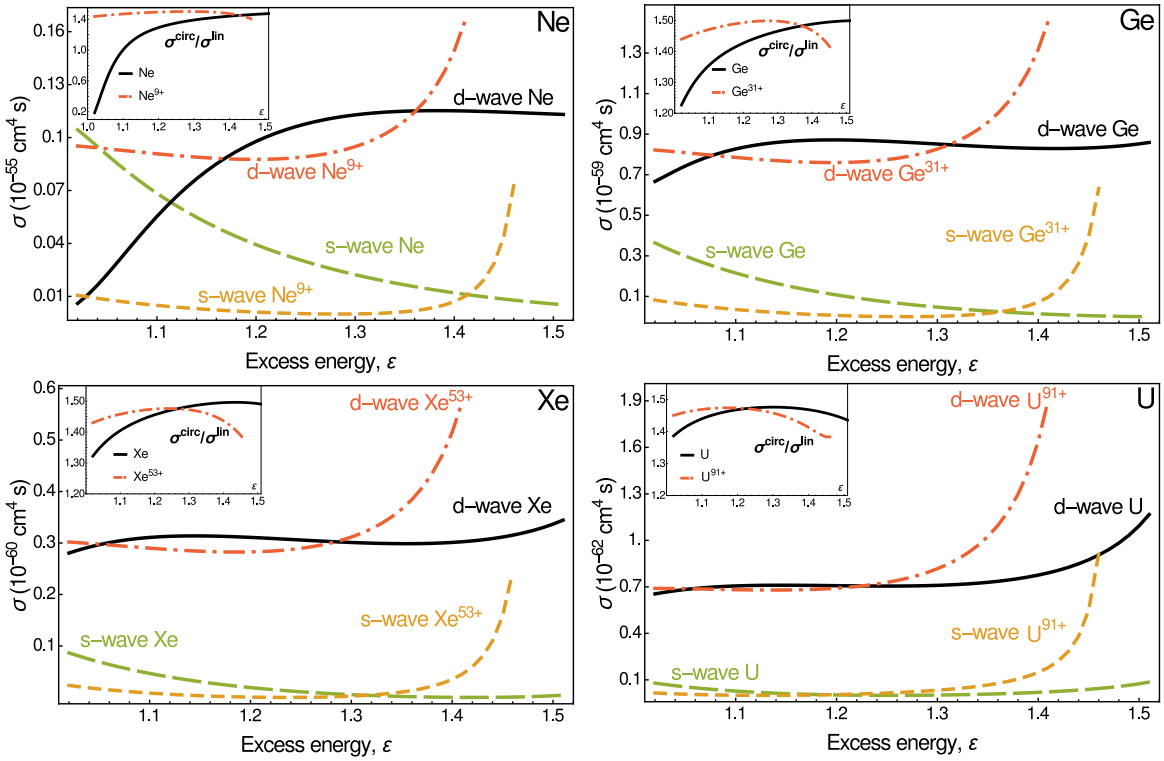

Figure 6: The partial-wave cross section as a function of excess energy compared for the $s \to p \to s$ (long-dashed green) and $s \to p \to d$ (solid black) ionization channels of neutral atoms by linearly polarized light. Results for the $s \to p \to s$ (short-dashed orange) and $s \to p \to d$ (dash-dotted red) ionization channels of hydrogen-like ions are also shown. As a consequence of screening effects, the $s \to p \to s$ channel becomes dominant for low-Z atoms in near-threshold photon energies. The ratio of cross sections corresponding to ionization by circularly and linearly polarized light is presented in top left corner of each figure. The screening effects also result in a deviation of this ratio from the known estimate of the ratio of cross sections corresponding to ionization by circularly $\sigma^{\rm circ}$ or linearly $\sigma^{\rm lin}$ polarized light, $\sigma^{\rm circ}/\sigma^{\rm lin} \approx 3/2$.

dominant channel occurs and creates a minimum of the cross section. We investigated the behaviour of the dominant d partial-wave near the ionization threshold energy, both with and without a screening potential, and found out that the d partial-wave in the presence of other electrons expands much further from the atom. That is why the d partial-wave contribution to the total cross section changes so drastically in this energy region. An opposite behaviour, i.e. a wave function collapse, was observed in Refs. [106, 107], where a strong increase of the single photon absorption cross section was predicted. The cross section minimum in our results is most pronounced for neon, for which the cross section of the $s \to p \to s$ channel is greater than the dominant $s \to p \to d$ channel in an energy region from the ionization threshold up to a crossing point of the channels at $\varepsilon = 1.12$. This crossing of the ionization channels is present for atoms with nuclear charges in the range $Z = 5 - 13$. Although for elements in this range other than neon, the crossing point lies in lower energies and the effects are thus weaker.

In the top left part of each of the figures 6, the ratio of total cross section for ionization by circularly $\sigma^{\rm circ}$ and linearly $\sigma^{\rm lin}$ light are also presented. According to the known estimate $\sigma^{\rm circ}/\sigma^{\rm lin} \approx 3/2$ [3], the ratio should be always approximately equal to 3/2 in nonresonant energy region. While this holds true for the hydrogen-like ions (dash-dotted red curve), in the case of neutral atoms (solid black curve), the screening effects result in a strong deviation from the estimated value. This follows directly from

the discussion of partial waves above.

3.2.2 Ionization of p electrons

In comparison to previous subsection, the analytical analysis of the two-photon ionization of a p electron increases on complexity due to the higher number of possible ionization channels. There are thirteen possible fine-structure two-photon ionization channels within electric dipole approximation. While it is still possible to analyze the total cross section for this process analytically, it becomes lengthy and cumbersome. On the other hand, the increased analytical complexity offers us new possibilities of controlling the two-photon ionization process. This will not become immediately apparent in the two-photon ionization cross section, however, in section 5.2.2 these "new" possibilities will be exploited in detail.

We use the Eq. (3.2) to derive the two-photon ionization of the atomic p shell within electric dipole approximation. If we further assume that the ionizing beam is fully polarized, we obtain the two-photon ionization cross sections for ionization of $p_{1/2}$ and $p_{3/2}$ respectively

$$\begin{aligned}\sigma^{(\mathrm{rel})}_{p_{1/2}} &= \frac{4\pi^3\alpha^2}{25\omega^2}\Big[25(1-P_c^2)|U^{(s_{1/2})}_{p_{1/2}}+U^{(d_{3/2})}_{p_{1/2}}|^2+(2+P_c^2)\big[|5U^{(s_{1/2})}_{p_{3/2}}+U^{(d_{3/2})}_{p_{3/2}}|^2\\ &+ 54|U^{(d_{3/2})}_{f_{5/2}}|^2\big]\Big] \end{aligned} \tag{3.6}$$

and

$$\begin{aligned}\sigma^{(\mathrm{rel})}_{p_{3/2}} &= \frac{4\pi^3\alpha^2}{5^4\omega^2}\Bigg\{-625\left(-4+P_c^2\right)|U^{(s_{1/2})}_{p_{3/2}}|^2+\left(82-34P_c^2\right)|U^{(d_{3/2})}_{p_{1/2}}|^2\\ &+ 81\left(52-49P_c^2\right)|U^{(d_{5/2})}_{p_{3/2}}|^2-108\left(-7+9P_c^2\right)U^{(d_{3/2})}_{p_{1/2}}U^{(d_{5/2})}_{p_{1/2}}\\ &- 50U^{(s_{1/2})}_{p_{3/2}}\left[2\left(-1+7P_3^2\right)U^{(d_{3/2})}_{p_{3/2}}+27\left(-4+3P_c^2\right)U^{(d_{5/2})}_{p_{3/2}}\right]\\ &+ 7\left(2+P_c^2\right)\left[175\left(5U^{(s_{1/2})}_{p_{1/2}}+U^{(d_{3/2})}_{p_{1/2}}\right)^2\right]\\ &+ 27\left[\left(7U^{(d_{3/2})}_{f_{5/2}}+3U^{(d_{5/2})}_{f_{5/2}}\right)^2+600|U^{(d_{5/2})}_{f7_{3/2}}|^2\right]\Bigg\}, \end{aligned} \tag{3.7}$$

where we used the fact that the transition amplitudes are real for nonresonant below-threshold two-photon ionization. Equation (3.7) already demonstrates the higher level of complexity. For analysis of the total two-photon ionization of light atoms, it is reasonable to assume that the fine-structure splitting does not play a significant role. In this nonrelativistic limit, it is possible to compactly express the cross section even without assuming that the incident beam is fully polarized. Since the splitting of the initial p state is not considered in this limit, by assuming the real-valued radial amplitudes $U^{(l_{n_{j_n}})}_{l_j}$ are equivalent for all fine-structure levels the two cross sections above results in a one nonrelativistic cross section

$$\begin{aligned}\sigma^{(\mathrm{nonrel})}_{p} &= \frac{18\pi^3\alpha^2}{25\omega^2}\Big[50|U^{(s)}_{p}|^2+\left(47+21P_l^2-45P_c^2\right)|U^{(d)}_{p}|^2+20U^{(s)}_{p}U^{(d)}_{p}(1+3P_l^2)\\ &+ 9\left(7+P_l^2+5P_c^2\right)|U^{(d)}_{f}|^2\Big]. \end{aligned} \tag{3.8}$$

It is immediately clear that the nonrelativistic cross section expression offers significantly compact and more intuitive form. Comparing the above nonrelativistic expression of the total two-photon ionization cross section to its relativistic equivalents, one

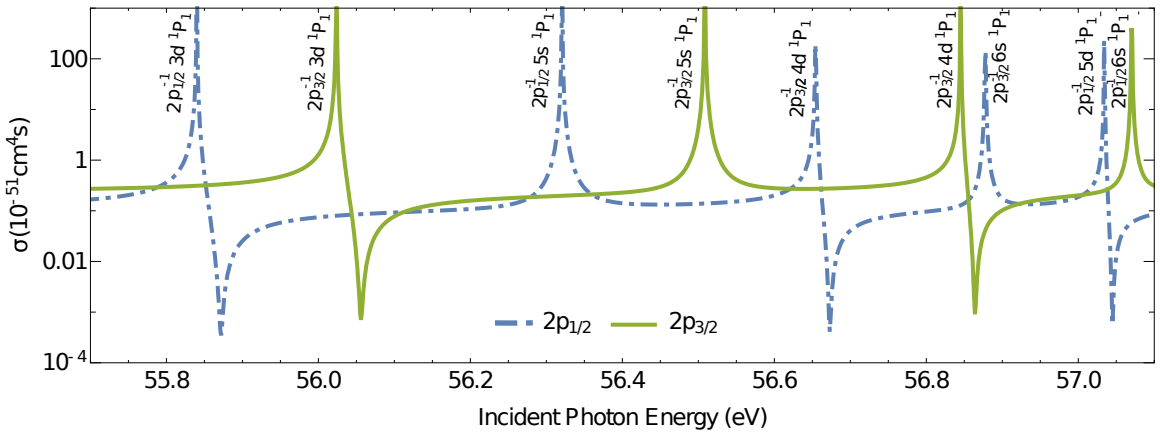

Figure 7: Total cross section of two-photon ionization of $2p_{1/2}$ (dot-dashed blue) and $2p_{3/2}$ (full green) electrons of a magnesium atom by right circularly polarized photons as a function of incident photon energy. The clearly visible resonances are due to matching of the photon energy and the $2p \to ns$ or $2p \to nd$ transitions. Between each pair of $nd_{3/2,5/2}$ resonances, there is a clear local minimum of the cross section. Each minimum appears due to the disappearance of the $p \to d \to f$ channel and is called the nonlinear Cooper minimum.

can notice subtle differences. For example, while the nonrelativistic $p \to s \to p$ channel is independent of the photon polarization, the fine-structure levels not only do, but some even vanish completely in the case of ionization by pure circularly polarized light.

While in the previous subsection we concentrated on two-photon ionization of s electrons near the two-photon ionization threshold, here, we demonstrate the impact of nonlinear Cooper minimum on the two-photon ionization of p electrons. According to the propensity rules [74], the ionization channel with the highest angular momentum generally dominates the ionization process process. This means, that for two-photon ionization of p electrons, the $p \to d \to f$ mainly determines the process. At the nonlinear Cooper minimum, this dominant ionization channel vanishes which is projected in practically all observables of the process (see 2.2.2 for detailed description of nonlinear Cooper minimum). Vanishing of the dominant ionization channel has indeed a significant influence on the amplitude of the total two-photon ionization cross section. Figure 7 shows the cross sections for ionization of $2p_{1/2}$ and $2p_{3/2}$ electrons of the neutral magnesium atom by two right-circularly polarized photons as a function of incident photon energy. In this very dynamic energy range, we can notice resonances which originate from the the photon energy matching the $2p \to ns$ or $2p \to nd$ electronic transitions. Beside these resonances, clear minima of the cross sections are also visible. The photon energies at which the total cross section is locally minimal correspond to the nonlinear Cooper minima. Each of these points occurs between $2p \to nd$ and $2p \to (n+1)d$ resonances. In the case of two-photon ionization of magnesium $2p$ electron, the minima appear near the resonance with lower principal quantum number. However, the position of the nonlinear Cooper minimum can vary extensively between different elements. The exact position is determined by the complete energy spectrum of an atom. Creation of an inner-shell hole in a p state often results in a strongly coupled system and rigorous many-electron treatment would be required for accurate predictions. In other words, experimental detection of the position of this nonlinear Cooper minimum could put the theoretical construction of the complete atomic spectrum to a test and could lead to our deeper understanding of light-matter interaction.

Just as we analysed the properties of the two-photon ionization of the s and p electrons, it would of course be possible to carry the corresponding analysis for other electron shells using the expression (3.2). However, due to the limited length of the

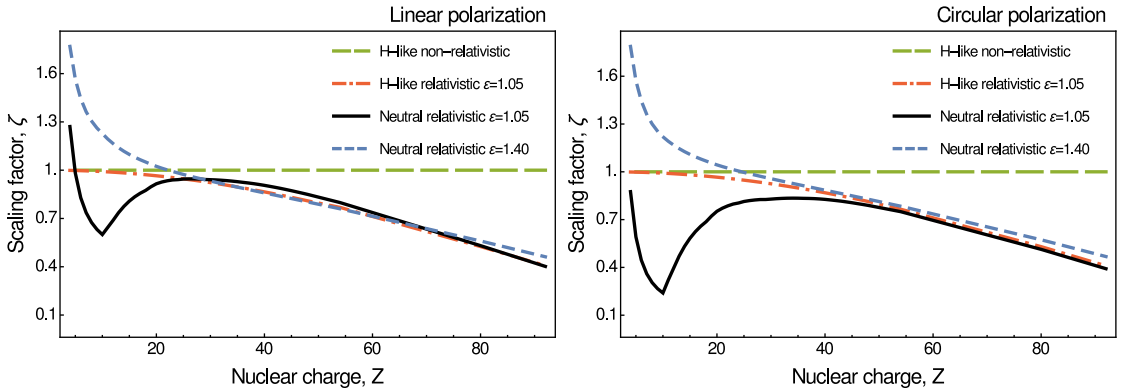

Figure 8: The scaling factor ζ as a function of nuclear charge for ionization of a $1s$ electron of neutral atoms ($Z = 4 - 92$) by two linearly (left) and circularly (right) photons at the excess energies $\varepsilon = 1.05$ and $\varepsilon = 1.40$. According to the nonrelativistic scaling of hydrogen-like ions (dashed green), the cross section scales with Z^{-6}. The deviation from this scaling due to relativistic effects is clearly visible for hydrogen-like (dash-dotted red) as well as neutral (solid black and short-dashed blue) atoms. Moreover, further deviation of the scaling factor in low-Z region is present for neutral atoms due to screening effects.

dissertation, we restrict our analysis to the two-photon ionization of the two mentioned shells.

3.2.3 Evaluation of relativistic and electron screening effects

Interaction of high intensity ultraviolet or x-ray laser pulses with atoms can results in ejection of electrons from the atom at relativistic energies. It is therefore important to evaluate the importance to account for relativistic effects [108, 109]. Reference [30], Koval *et al.* show that in two-photon ionization of heavy hydrogen-like ions, the relativistic effects contribute significantly to the ionization cross sections, and hence, may not be neglected in their calculations. It is therefore reasonable to expect similar behaviour for ionization of neutral atoms. The purpose of this subsection is to evaluate the importance of using fully relativistic approach to describe the two-photon ionization of atoms as well as to describe the difference of ionization of neutral and hydrogen-like atoms. Since relativistic effects depend on the effective strength of the Coulomb field the active electron is in, it is reasonable to perform the analysis on two-photon ionization of $1s$ electrons. First, we will compare nonrelativistic electric-dipole with fully relativistic calculations and investigate the dependence of the relativistic effects on the nuclear charge. Moreover, we will also study the influence of the choice of screening potential (see Sec. 2.2.3) on the total two-photon ionization cross section. This will be done by performing additional calculations for two-photon ionization of hydrogen-like atoms. Then, we carefully analyze the individual contributions to the relativistic effects, which were introduced in Sec. 2.1.

In nonrelativistic theory, the nonresonant cross section for the two-photon ionization of hydrogen-like ions in dipole approximation scales with the nuclear charge as $\sigma(Z, \omega Z^2) = \sigma(Z = 1, \omega) Z^{-6}$ [21]. We adopt the approach from Ref. [30] and introduce so called scaling factor ζ to the above expression, i.e., $\sigma(Z, \omega Z^2) = \zeta(Z)\sigma(Z = 1, \omega) Z^{-6}$. The deviation of the scaling factor from the value 1 then represents various effects arising from the full relativistic description and/or the inter-electronic interaction. For nonrelativistic electric dipole calculation in Coulomb potential, the scaling factor is $\zeta(Z) = 1$ for all Z values and is almost independent of the excess energy in the nonresonant region.

Figure 8 shows the plot of the scaling factor $\zeta(Z)$ as a function of nuclear charge

for two-photon ionization by linearly, and circularly polarized light. The results are shown for nonrelativistic (dashed green) and relativistic (dash-dotted red) calculations for ionization of hydrogen-like ions as well as relativistic calculation for ionization of neutral atoms at $\varepsilon = 1.05$ (solid black) and $\varepsilon = 1.40$ (long-dashed blue) excess energies. We can see that for neutral atoms, there are two distinct deviations of the scaling factor from the constant nonrelativistic value. One of the deviations stretches between the medium- and high-Z region and is also present for the case of hydrogen-like atoms. The second deviation lies in the low-Z region and is present only for the ionization of neutral atoms. Let us first discuss the deviation in the low-Z region. This deviation results from the interelectronic interaction, which decreases the electron binding energies and as a result, increases the total cross section. We can see, that this is indeed the case for the $\varepsilon = 1.40$ excess energy, where the screening effects increase the total cross section in the low-Z region. This increase rapidly weakens with increasing nuclear charge as we would expect. However, for $\varepsilon = 1.05$, the screening effects result in a decrease of the cross section, with a maximum at $Z = 10$. The sharpness of the trough is a result of the discrete values of the nuclear charge Z values. For photon energies exceeding the ionization threshold by more than 15%, i.e. $\varepsilon > 1.15$, the trough vanishes. From figure 8, we can see that the screening effects are stronger for the case of ionization by circularly than linearly polarized light. We can understand this from a partial-wave analysis, which reveals the local minimum of the dominant ionization channel for the low-Z elements [64].

The second deviation of the scaling factor in medium- and high-Z region in the Fig. 8 arises from the relativistic effects. The importance of these effects linearly increases with nuclear charge Z. We can also see that unlike screening effects, relativistic effects are independent of polarization of the incident photon. From this we can conclude that relativistic effects influence all partial waves in a same way. For two-photon ionization of uranium, the relativistic effects decrease the total cross section by about a factor of two. We would expect, that the relativistic effects would be stronger for the ionization of hydrogen-like ions than for ionization of neutral atoms, since the electron binding energies of hydrogen-like ions are higher. However, from Fig. 8, it can be seen, that the deviation of the scaling factor (and therefore the cross section itself) for neutral atoms due to relativistic effects is comparable as for hydrogen-like ions.

As we described in the second chapter of this thesis, relativistic effects constitute of units of various origin. We will now closely investigate the individual contributions by performing calculations within different approximations. Each of the approximations can be understood as a certain simplification of Eq. (3.4). Firstly, in order to study the effects of higher-order multipoles, we restrict the infinite summations in transition amplitude (2.20) over the multipoles pJ to $p = 1$ (electric) and $J = 1$ (dipole) terms only. This approximation is known as the dipole approximation (DA), and we denote the corresponding cross section as σ^{DA}. Secondly, the summation in Eq. (3.4) over the virtual intermediate states $|n_n\kappa_n m_n\rangle$ runs over the complete (positive and negative) energy spectrum. The presence of negative energy states in the sum corresponds to the process with creation of a positron in the intermediate state. Thus, in order to enumerate the contribution from this process, we, in addition to the dipole approximation, restrict summation over the intermediate states to the positive energy states only. We refer to this calculation as dipole and no-pair approximations (DA + NPA), and denote the corresponding cross section as $\sigma^{\mathrm{DA+NPA}}$. Finally, we consider also the nonrelativistic limit (NR) of Eq. (3.4). For this, we employ the wave functions which are the solutions of the Schödinger equation and replace interaction operators $\boldsymbol{\alpha} \cdot \boldsymbol{a}_J^{(p)}$ by its nonrelativistic limit $\omega r/\sqrt{6\pi}$ and also set $p_1 = p_2 = 1$ and $J_1 = J_2 = 1$. The corresponding cross section is denoted as σ^{NR}. If, however, no approximation is made, i.e., the Dirac equation is used to obtain the electron wave functions, summation over

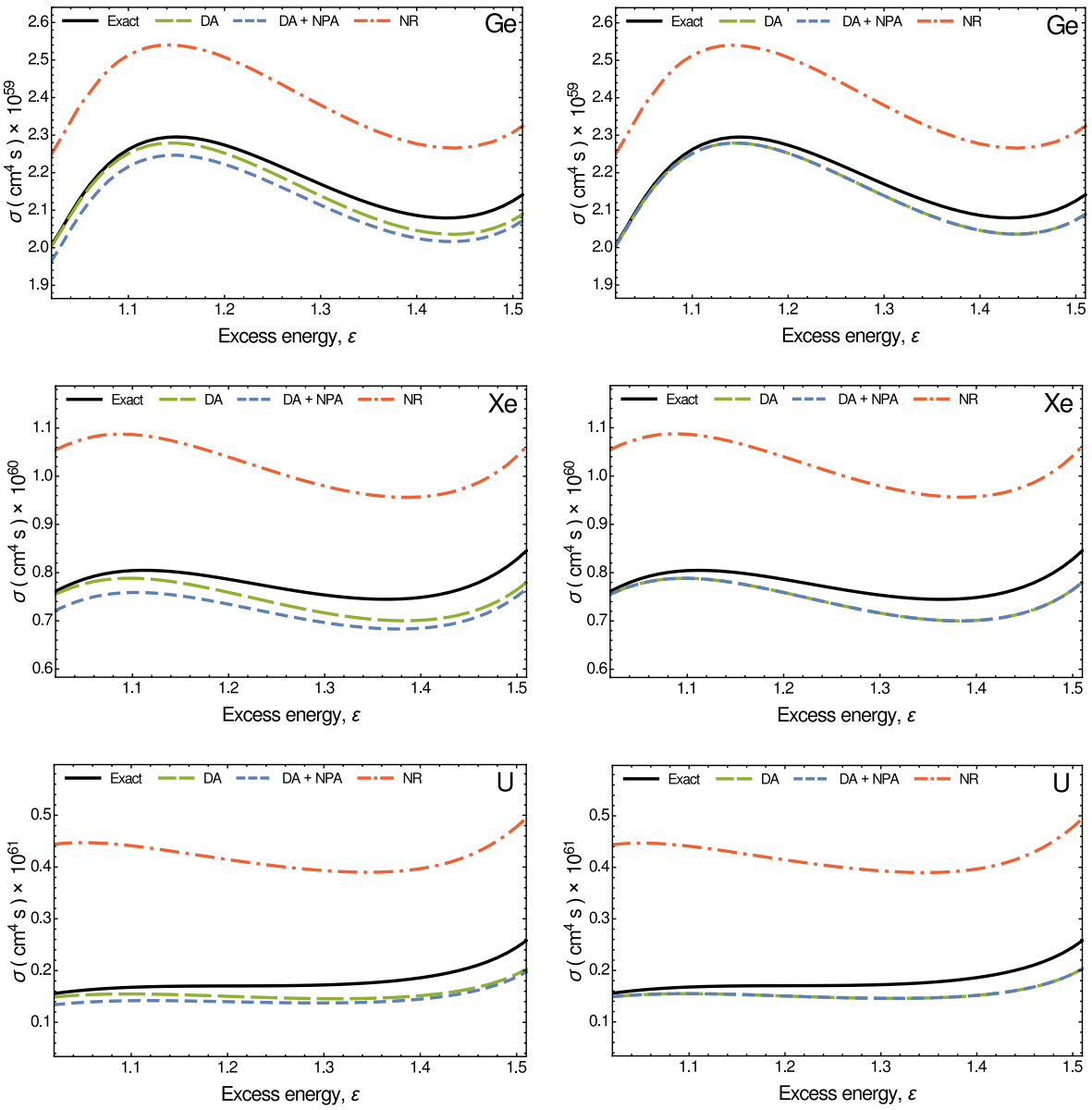

(a) Velocity gauge (b) Length gauge

Figure 9: Total nonresonant K-shell two-photon ionization cross section $\sigma^{(\mathrm{rel})}_{s_{1/2}}$ as a function of excess energy within different approximations; exact relativistic σ^{Exact} (solid black), dipole σ^{DA} (long-dashed green), dipole + no-pair $\sigma^{\mathrm{DA+NPA}}$ (short-dashed blue), and nonrelativistic σ^{NR} (dot-dashed red). The calculations are carried out in (a) velocity (left column) and (b) length (right column) gauges for ionization of neutral germanium, xenon, and uranium atoms.

the intermediate states runs over both positive and negative energy states, and all multipoles are taken into account, we refer to such calculations as "Exact", and we write the cross sections as σ^{Exact}. In practice, the multipole summation is restricted to $J_{\max} = 5$, which is sufficient to obtain convergence of the corresponding total cross section at less than 0.001% level.

Figure 9 presents the total nonresonant K-shell TPI cross section as function of excess energy for the ionization of neutral germanium, xenon, and uranium atoms by linearly polarized light. The minima in the total cross sections (see Fig. 9) in near-threshold energies occur as consequences of screening effects as discussed earlier. Here, we compare the total cross section values within various approximations and see that

the major difference is present between σ^{NR} and all other approximations. The reason for this is that the Dirac wave functions have been used in all calculations, except the NR one, and solving the Dirac equation results in a contraction of the electron wave function (see Fig. 1). As a consequence of this contraction, the total two-photon ionization cross section is significantly lower in the relativistic description. We would expect that the decrease of the exact calculation (in comparison to the nonrelativistic limit) should be "stronger" with increasing nuclear charge and photon energy. However, while it is true that the cross section drop increases with nuclear charge, it slowly decreases with energy. This is due to the higher multipole (beyond dipole approximation) effects, which open further channels for the ionization. As it is clear from Fig. 9, the cross section values in electric dipole approximation coincide with the exact calculation for near threshold energies, however, the "strength" of multipole effects increases with energy and counteracts the cross section decrease due to wave function contraction. Thus, in the exact calculation, the strength of the overall relativistic effects slowly decreases with energy. We can see that this is the case both in velocity as well as length gauges. The gauge independence does not hold any longer for the no-pair approximation. Our results show that DA+NPA calculations result in a decrease of the total cross section values in the velocity gauge, while in the length gauge they result only in negligible effect (less than 0.05%). Thus, the negative continuum energy effects are only essential in the velocity gauge, where they lead to an increase of the cross section by up to 10% as compared to the length gauge. The strong gauge dependence of negative continuum energy effects has been previously also reported for the case of two-photon bound-bound transitions in hydrogen-like ions [110, 111].

Although the importance of relativistic contributions to the two-photon ionization was evaluated for ionization of K shell electrons, we can estimate the corresponding contributions to other shells. From figure 9, we concluded that the dominant relativistic effect arises from the wave function contraction of the bound electron. Since the Coulomb field is weaker for higher shell electrons, one would respectively also expect that their wave function contraction is less significant. This physical picture is confirmed by figure 1, where the $2p$ electron wave function is affected by relativistic contraction less than the $1s$ wave function. Quantitatively, one could therefore expect that the importance of the relativistic effects for ionization of higher shells scales as n^{-2} with respect to the two-photon ionization of K shell electrons. Same dependence of the strength of relativistic effects on ω and Z is expected for ionization of higher shells as for ionization K shell electrons.

3.3 Experimental status

While the first experiments measuring the two-photon ionization concentrated on ionization of outer shell electrons [112–115], much of recent experiments probed the K shell electrons of solid targets [24–27]. The ionization of these deeply bound electrons was enabled by the advances in free-electron laser development. Although the nonresonant two-photon ionization still remains a challenge due to low cross sections, it is possible to detect the process by measuring the subsequent $K\alpha$ fluorescence. This fluorescence radiation emitted by the decay of the $2p$ electron into the $1s$ vacancy is a direct signature of the two-photon ionization process. This approach has been exploited in number of experiments [24–27]. The majority of inner-shell two-photon ionization experiments has been performed on the nonresonant ionization of $1s$ electrons only, which we analysed in Sec. 3.2.1. For this reason, we will concentrate on comparison of our calculations with the above mentioned experimental measurements.

To compare the two-photon K shell ionization cross sections with theory, the Z^{-6} scaling introduced by Zernik [21] is often used. This simple nonrelativistic scaling

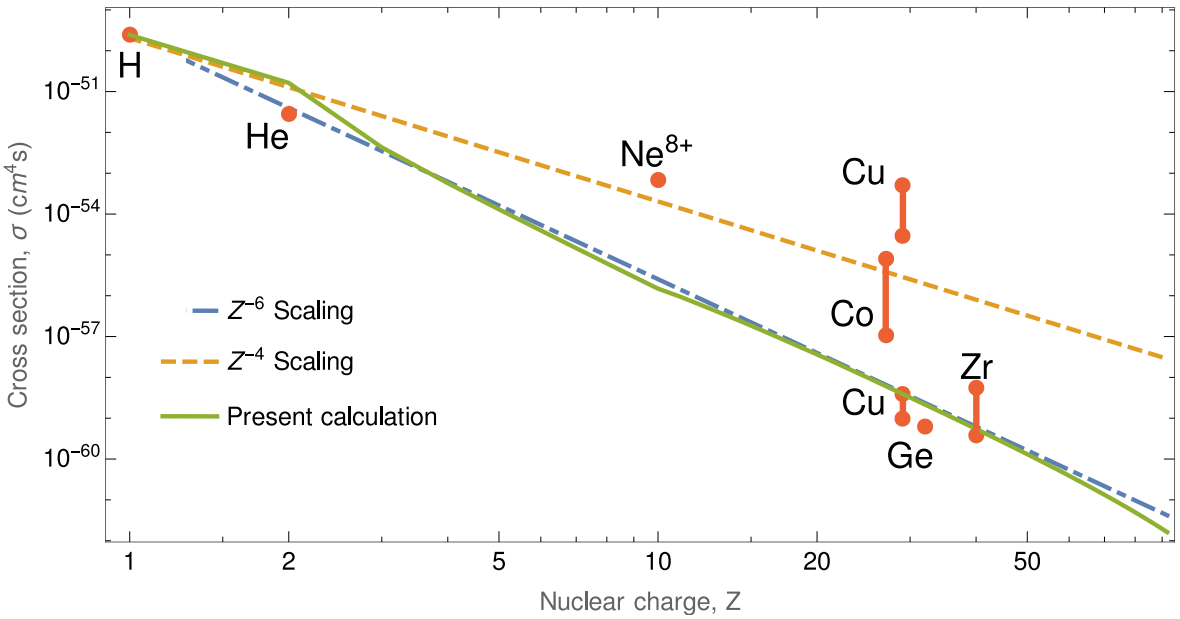

Figure 10: The total cross section for two-photon ionization by linearly polarized light as a function of nuclear charge. The cross section is plotted for incident photon energy near two-photon ionization threshold, or in terms of the excess energy, $\varepsilon = 1.05$, (solid green). The Z^{-6} scaling law (dot dashed blue), Z^{-4} scaling (dashed orange) and experimental values for hydrogen [22, 23], helium [116](which was measure for above-threshold ionization with 41.8 eV photon energy), helium-like neon [38], cobalt [117] (a value obtained from scaled one-photon absorption cross section), copper near one-photon [26] and two-photon ionization threshold [27], germanium [24] and zirconium [25] atoms are also shown.

law reaches a good agreement with the full relativistic calculation and most of the experimental values. Figure 10 shows calculated total cross sections for elements in the range $Z = 1 - 92$ for photon energy near the two-photon ionization threshold ($\varepsilon = 1.05$, solid green) as well as the scaling law (dot-dashed blue). One can notice slight deviations of our calculated cross sections from the Z^{-6} scaling, explicitly, two at low Z elements and then at high Z. The deviation at two-photon ionization of low Z elements is caused by the electron screening effects discussed earlier. While for helium, the electron screening results in higher cross section, for $Z \approx 10$, the screening has an opposite effect. For two-photon ionization of heavy elements, the relativistic effects, which were analyzed in previous section, start to significantly contribute and decrease the cross section value. The explicit decrease of the cross section for high-Z atoms can be better seen in Fig. 8.

Figure 10 also shows experimental values (red marks) for the two-photon K-shell ionization of hydrogen [22, 23], helium [116], helium-like neon [38], cobalt [117], copper near one-photon [26] and two-photon ionization threshold [27], germanium [24] and zirconium [25] atoms. Out of these experiments, the values for two-photon ionization of helium atoms [116] were performed with photon energy of 41.8 eV, and hence, it corresponds to above-threshold ionization, where already the first photon promotes the electron to continuum. Moreover, the cross section for ionization of cobalt [117] was obtained from a previously obtained scaling between one- and two-photon absorption [26]. We can also see that our cross section value for ionization of germanium [24], copper [27] as well as zirconium [25] is close to the experimental value, which lies within the experimental uncertainty. These experiments have been performed with photon energies tuned to the vicinity of two-photon ionization threshold. On the other hand, in another experiment, Doumy, *et al.* [38] measured the two-photon ionization of helium-like neon to be 7×10^{-54} cm^4 s. Theoretical calculations [31, 118, 119] of this

cross section resulted in a discrepant value, lower by about three orders of magnitude. We applied our formalism for the case of Ne^{8+} as well, and obtained a cross section of 3.1×10^{-57} cm^4 s which is in an agreement with previous calculations [31, 118, 119]. The three orders of magnitude deviation obtained suggests a resonant enhancement of the cross section and can be explained by broader spectral bandwidth of the FEL employed. Furthermore, the experimentally determined cross section for two-photon ionization of cobalt [117] and copper [26] atoms are also orders of magnitude larger than theoretically predicted values. These experiments have been performed at photon energies near the one-photon ionization threshold. Similarly as in the case of two-photon ionization of helium-like neon, this could be possibly explain by the spectral properties of the free-electron laser beams. It has been suggested, that the total cross sections near one-photon ionization threshold could be scaling with the fourth power of nuclear charge, instead of the sixth, i.e. $\sigma(Z, \omega Z^2) = \sigma(Z = 1, \omega)Z^{-4}$ [117]. At this point, there are further experiments planned to test this scaling hypothesis.

At the time of writing, there are already numerous experiments planned to be carried out to measure the total two-photon ionization cross sections. For example, there are experiments planned at the SACLA free-electron laser facilities to carry out laser assisted ionization, in which an K shell electron is promoted into the Rydberg manifold by an extreme ultraviolet pulse and is ionized by an overlapping infrared beam. Another promising idea comes from the ion trap project called HILITE at GSI Helmholtzzentrum für Schwerionenforschung in Darmstadt [120]. The penning trap developed by the group will be able to trap charged ions which will be then coupled to a free-electron laser with the goal to detect multi-photon ionization. This approach would allow to study the two-photon ionization on a fundamental level and explore the effects of changing atomic potential (by varying the charge state) on the total cross section.

4 Emission Direction of Photoelectrons

When an electron is photoionized from an atom, it is generally not emitted homogeneously into all directions. Instead, the emission along the electric field vector of the incident light is generally preferred. However, does this general expectation hold in all cases? Is there any specific photoelectron emission direction that is forbidden? Does the electron emission direction depend on the handedness of the ionizing light? On the course of this chapter, we will unveil the answers to these questions and discover further insights.

In the previous section, we have ignored any angular dependence of the electron emission, and assumed that we are able to collect photoelectrons emitted in all directions. However, it is indeed experimentally possible to resolve the angular emission of the photoelectrons. In this chapter, we will show that carrying out such angle-resolved studies is important for our understanding of light-matter interaction, and demonstrate that these studies reveal information, which was not contained in the total cross sections. One such example is the photoelectron phase, which allows us to study the time delay in photoionization [81, 121, 122], or give rise to interesting effects such as elliptical dichroism in two-photon ionization [67]. The measurements of photoelectron angular distributions can also reveal light-matter interaction beyond the electric dipole approximation. Contributions of higher multipole transitions can be extracted from the forward-backward asymmetries in photoelectron angular distributions [30, 46, 62, 123]. Furthermore, particularly in nonlinear regime, photoelectron distributions can be used for accurate extraction of ionization parameters [56]. This is the case as the angular distributions are generally insensitive to experimental parameters such as beam intensity, which is the main limitations of experimental accuracy. All above mentioned properties of angular distributions provide a strong motivation to study this observable for the fundamental two-photon ionization process.

We start with a general description of angle-resolved photoelectron emission in the following subsection. Then, analogously to the previous section, we will perform electric dipole approximation to derive photoelectron distributions for two-photon ionization of specific electron shells and analyse the effects of polarization of the incident photons on the distributions. Analysis of these results will lead us to description of elliptical dichroism as well as to studying its physical origin and properties. In the final subsection, we will compare our calculations to experimentally obtained results. We will present some of our results in a form of three dimensional plots, where the length of a point from the distribution center represents the amplitude of the cross section in that particular direction. An example of such distribution is shown in Fig. 11. In the figure, we also present two different planes which will be used in this section for presentation of the results. The left side of Fig. 11 shows a plane perpendicular to the photon propagation direction, which will be particularly useful in studying the left-right asymmetry in photoelectron distributions for two-photon ionization by elliptically polarized light. The right side of Fig. 11, shows a plane which intersects the three dimensional distribution in the plane spanned by the photon propagation and linear polarization directions, which will be important in quantifying the relativistic effects in photoelectron angular distributions.

4.1 General angle-differential cross section

Similarly as in previous chapter, we start with the general density matrix of the final state Eq. (2.31) and trace out those degrees of freedom, which we consider to be unobserved in an experiment. For the angle-differential cross section, we do not consider observation of the spin state of the escaping electron nor the polarization of the pho-

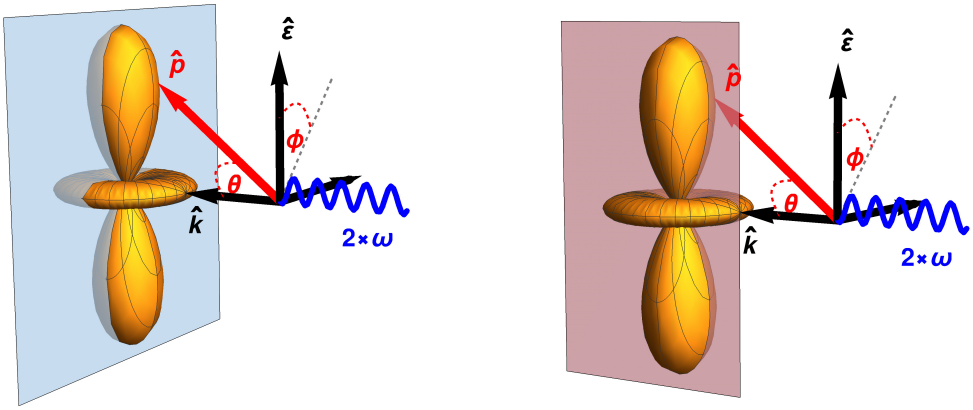

Figure 11: Photoelectron angular distributions for two-photon ionization in considered geometry. The propagation direction of the two incident photons defines the quantization axis. The photoelectron emission direction is defined by two angles θ and ϕ. Results in this chapter will be presented in three different forms. Three dimensional distributions, where the length of a side represents the magnitude of cross section in given direction, in plane perpendicular to the photon propagation direction (left), and in the plane created by the linear polarization and photon propagation directions (right).

toion. We do however consider detectors which are sensitive to the direction of emission of the photoelectron. In order to obtain the angle-differential two-photon ionization cross section, we need to sum over all quantum numbers of the final ion state as well as the photoelectron spin projection. The angle-differential cross section has the form

$$\begin{aligned}\frac{d\sigma(\omega)}{d\Omega} &= \frac{8\pi^3\alpha^2}{\omega^2}\sum_{J_f M_f m_e}\langle \alpha_f J_f M_f, \boldsymbol{p}_e m_e \left|\hat{\rho}_f\right| \alpha_f J_f M_f, \boldsymbol{p}_e m_e\rangle \qquad (4.1)\\ &= \frac{8\pi^3\alpha^2}{\omega^2[J_i]}\sum_{\substack{\lambda_1\lambda_2\\ \lambda_1'\lambda_2'}}\langle \boldsymbol{k}\lambda_1\left|\hat{\rho}_\gamma\right|\boldsymbol{k}\lambda_1'\rangle\langle \boldsymbol{k}\lambda_2\left|\hat{\rho}_\gamma\right|\boldsymbol{k}\lambda_2'\rangle\sum_{\substack{J_f M_f\\ M_i m_e}} M^{\lambda_1\lambda_2}_{J_i M_i J_f M_f m_e} M^{\lambda_1'\lambda_2'*}_{J_i M_i J_f M_f m_e}.\end{aligned}$$

This cross section places no restriction on the photon polarization nor on the angular momentum properties of the active electron, however, it does not offer any theoretical insights into the ionization process. To analytically investigate the properties of the angle-differential two-photon ionization cross section, we need to restrict our analysis to ionization of a specific shell. Consistently with the previous section, we perform the analysis for two-photon ionization of s and p electrons. Moreover, for practical purposes, we apply the electric dipole approximation, which nevertheless describes the dominant part of the photon-electron interaction. Later, we will present numerical calculations of the cross sections including higher multipole orders, which will be done using Eq. (4.1).

4.2 Ejection of an electron from specific electron shells

4.2.1 Ionization of s electrons

We start with a discussion of the photoelectron emission direction in the case of two-photon ionization of s electrons. Although we will restrict this discussion to electric dipole interaction only, later, we will analyse the limits of this approximation in later section. The relatively low amount of ionization channels in the case of ionization of s electrons makes the analysis of the photoelectron angular distributions allows to still

provide fairly compact expressions. This analysis has been done before by Manakov *et al.*[124], who derived the photoelectron angular distributions expression for two-photon ionization in a nonrelativistic picture and for purely polarized light. Since the relativistic treatment is more complex than nonrelativistic one due to the fine structure of the atomic levels, we also assume purely polarized photons, i.e. $P_l^2 + P_c^2 = 1$. However, later when we reduce our formalism to the nonrelativistic limit, we will uplift this restriction placed on incident photon polarization and obtain a more general expression. Under the above mentioned constrains, the angle-differential cross section for two-photon ionization of s electrons is obtained from the general Eq. (4.1)

$$\begin{aligned}
\frac{d\sigma_s^{(\mathrm{rel})}}{d\Omega} &= \frac{\pi^2\alpha^2}{10\omega^2}\Big\{10|U_{s_{1/2}}|^2P_l^2 + \frac{1}{5}|U_{d_{3/2}}|^2\big[2P_l^2 + 3\sin^2\theta(3 - 2P_l^2 + P_l\cos(2\phi))\big] \\
&+ \frac{81}{10}|U_{d_{5/2}}|^2\big[4P_l^2 - 4\sin^2\theta(3P_l^2 - 2 + P_l\cos(2\phi)) + 5\sin^4\theta(P_l\cos(2\phi) + 1)^2\big] \\
&+ 18\mathrm{Re}\Big[U_{d_{5/2}}U_{s_{1/2}}^* e^{i(\Delta_{d_{5/2}} - \Delta_{s_{1/2}})}P_l\big[2P_l - 3\sin^2\theta(P_l + \cos(2\phi) - iP_c\sin(2\phi))\big]\Big] \\
&+ \frac{9}{5}\mathrm{Re}\Big[U_{d_{5/2}}U_{d_{3/2}}^* e^{i(\Delta_{d_{5/2}} - \Delta_{d_{3/2}})}\big[15\sin^4\theta(P_l\cos(2\phi) - 1\big)^2 \\
&- 12\sin^2\theta(2P_l\cos(2\phi) + P_l^2 + 1) + 4P_l^2\big]\Big] \\
&+ 4\mathrm{Re}\Big[U_{s_{1/2}}U_{d_{3/2}}^* e^{i(\Delta_{s_{1/2}} - \Delta_{d_{3/2}})}\big[P_l^2 - \frac{3}{2}P_l\sin^2\theta(P_l + \cos(2\phi) + iP_c\sin(2\phi))\big]\Big] \\
&\Big\}, \qquad (4.2)
\end{aligned}$$

with $U_{s_{1/2}} = U_{s_{1/2}}^{(p_{1/2})} + 2U_{s_{1/2}}^{(p_{3/2})}$ and $U_{d_{3/2}} = 5U_{d_{3/2}}^{(p_{1/2})} + U_{d_{3/2}}^{(p_{3/2})}$, and $U_{d_{5/2}} = U_{d_{5/2}}^{(p_{3/2})}$.

If we compare this expression to its angle-integrated equivalent (3.4), which represents the total two-photon ionization cross section, we can notice, that the photoelectron angular distributions offer access to information, which cannot be obtained from the total cross section. For example, the interference terms between the channels with final s and d symmetry are the only terms of Eq. (4.2) which depend linearly on the degree of circular polarization. This means that the interference gives rise to interesting phenomena such as elliptical dichroism (see Sec. 4.3 for more details). Moreover, the photoelectron angular distributions also contain the information about the difference of photoelectron phases of different ionization channels, which can play a key role in determination of the emission direction of the photoelectrons.

In nonrelativistic limit, the radial transition amplitudes $U_{l_j}^{(l_{n j_n})}$ and phases Δ_κ are considered to be equivalent for individual fine-structure levels. This means that the five possible ionization paths reduce to two nonrelativistic paths $s \to p \to s$ and $s \to p \to d$ (see Sec. 2.2.1 for more details and Fig. 3 in particular for an illustrative explanation). Both of these channels contain a transition through intermediate state with p symmetry. For the sake of shorter notation, we will omit the superscript from the notation of transition amplitudes. In the nonrelativistic limit the angle-differential two-photon ionization cross section is given by

$$\begin{aligned}
\frac{d\sigma_s^{(\mathrm{nonrel})}}{d\Omega} &= \frac{9\pi^2\alpha^2}{2\omega^2}\Big\{|U_s|^2\mathcal{P} \qquad (4.3) \\
&+ |U_d|^2\Big[\mathcal{P} - 3\sin^2\theta\big(\mathcal{P} + 2P_l\cos(2\phi)\big) + \frac{9}{2}\sin^4\theta\big(1 + P_l\cos(2\phi)\big)^2\Big] \\
&+ 2\mathrm{Re}\big[U_sU_d^* e^{i(\Delta_s - \Delta_d)}[\mathcal{P} - \frac{3}{2}\sin^2\theta\big(\mathcal{P} + 2P_l\cos(2\phi) + 2iP_lP_c\sin(2\phi)\big)]\big]\Big\},
\end{aligned}$$

where the parameter $\mathcal{P} = 1 + P_l^2 - P_c^2$, takes the value $\mathcal{P} = 2$ whenever the incident photons are purely linearly polarized and $\mathcal{P} = 0$ for purely circularly polarized light.

Unlike in the relativistic expression, the Stokes parameters in Eq. (4.3) can take any value, as we did not assume that the photons are fully polarized, i.e. $P_l^2 + P_c^2 = 1$. If we would consider that the photons are purely polarized, the above formula reduces to the one derived in Ref. [105].

The general structure of this thesis aims to present numerical examples for each analytical case study. However, plethora of examples of two-photon ionization of s electrons will be presented in this section in the next sections and presenting examples here would lead to an unnecessary repetition. We will, therefore, restrain of presenting any results in this subsection and refer the curious reader to further section for examples of the corresponding angular distributions.

4.2.2 Ionization of p electrons

As we have seen in the case of total two-photon ionization cross section, the complexity of analytical analysis of two-photon ionization of electrons with nonzero angular momentum is generally higher than for the case of ionization of s electrons. While in the case of total two-photon ionization the relativistic cross section expression was of a reasonable length, in the case of electron angular distribution the cross section reaches impractical complexity. For this reason, in this chapter we will abandon our general top-to-bottom approach in which we derive the relativistic expression and then reduce it a nonrelativistic limit. Instead, we directly derive only the nonrelativistic angle-differential two-photon ionization cross section. Numerically, however, it causes no difficulties to calculate the corresponding cross section. The general angle-differential cross section (4.1) was used to obtain the results in this subsection.

By selecting the initial state together with the electric dipole approximation, equation (4.1) can be used to obtain the angle-differential cross section for two-photon ionization of p electrons in the nonrelativistic limit

$$
\begin{aligned}
\frac{d\sigma_p^{(nonrel.)}}{d\Omega} = \frac{9\pi^2\alpha^2}{25\omega^2}\Bigg\{ & 50|U_p^{(s)}|^2 \sin^2\theta\big(1 + P_l\cos(2\phi)\big) \\
& + |U_p^{(d)}|^2\Big[18\mathcal{P} + \sin^2\theta\big(10 + 14P_l\cos(2\phi) - 3P_l^2 - 9P_c^2\big)\Big] \\
& + |U_f^{(d)}|^2\Big[2\mathcal{P} - 2\sin^2\theta\big(2P_l\cos(2\phi) + 2P_l^2 - 4P_c^2\big) + 5\sin^4\theta\big(1 + P_l\cos(2\phi)\big)^2\Big] \\
& + 20U_p^{(s)}U_p^{(d)*}\sin^2\theta\big(1 + 4P_l\cos(2\phi) + 3P_l^2\big) + 60\mathrm{Re}\Bigg[U_p^{(s)}U_f^{(d)*}e^{i(\Delta_p - \Delta_f)} \\
& \times\Big[\sin^2\theta\big(2 + 3P_l\cos(2\phi) + P_l^2 + iP_lP_c\sin(2\phi)\big) - \frac{5}{2}\sin^4\theta\big(1 + P_l\cos(2\phi)\big)^2\Big]\Bigg] \\
& + 6\mathrm{Re}\Bigg[U_p^{(d)}U_f^{(d)*}e^{i(\Delta_p - \Delta_f)}\Big[6\mathcal{P} - 5\sin^4\theta\big(1 + P_l\cos(2\phi)\big)^2 \\
& + \sin^2\theta\big[20iP_lP_c\sin(2\phi) - 12P_l\cos(2\phi) - 7P_l^2 + 9P_c^2 - 5\big]\Big]\Bigg]\Bigg\}.
\end{aligned}
\tag{4.4}
$$

As a reminder, the symbol $\mathcal{P}$ is given by $\mathcal{P} = 1 + P_l^2 - P_c^2$, and hence vanishes for pure circular polarization and is equal to two for linear polarization. Even in nonrelativistic limit, the angle-differential cross section for two-photon ionization of p electrons becomes lengthy. Nevertheless, it is worth noticing few details which reveal some properties of the photoelectron distributions. For example, the first four terms (including one interference term) of the above expression do not depend on the photoelectron

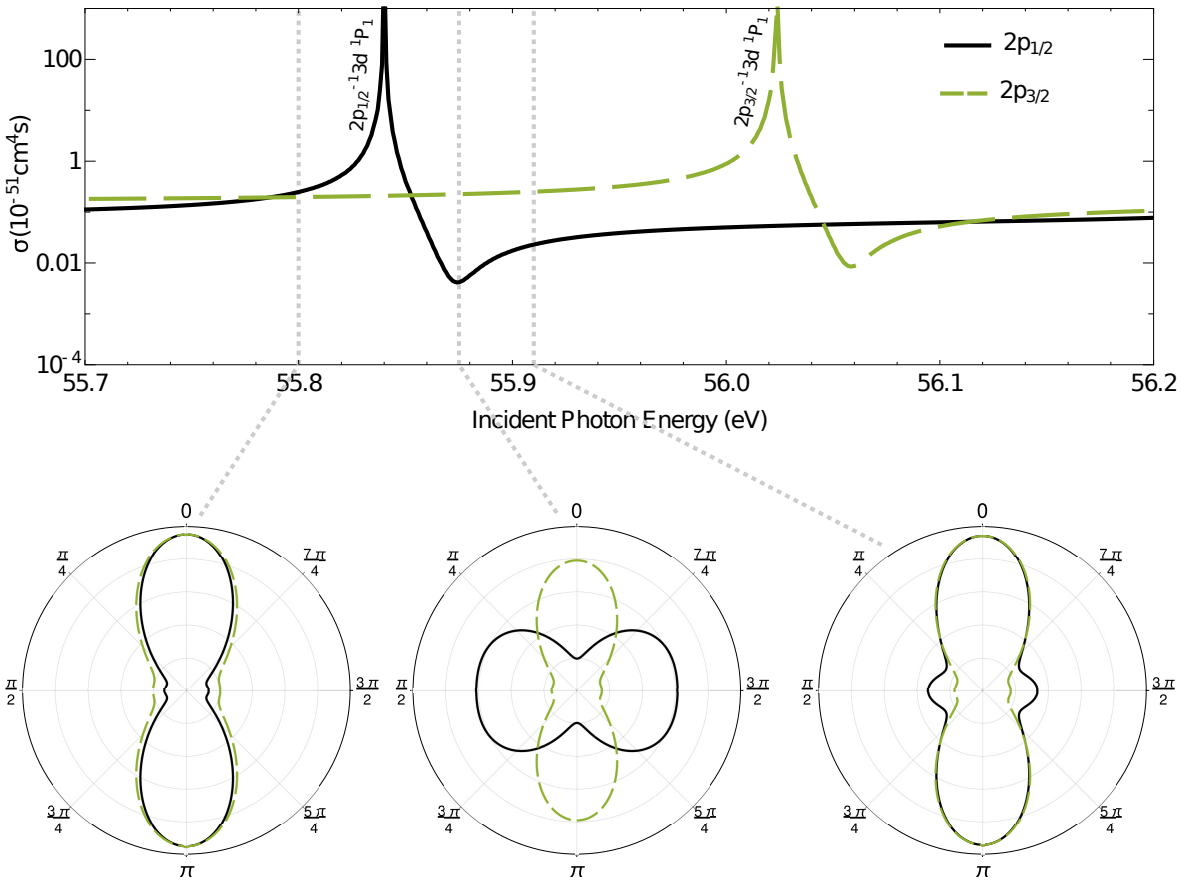

Figure 12: Two-photon ionization of magnesium $2p$ electrons with linearly polarized light. The upper figure shows the total cross section for ionization of $p_{1/2}$ (solid black) and $p_{3/2}$ (dashed green) electrons in the vicinity of nonlinear Cooper minimum (see Sec. 2.2.2 and Sec. 3.2.2 for details). The lower part of the figure three photoelectron angular distributions at energies lower than, matching and higher than the nonlinear Cooper minimum corresponding to ionization of the $2p_{1/2}$ electron. Distributions are shown for ionization of both $2p_{1/2}$ (solid black) and $2p_{3/2}$ (dashed green) electrons. The magnitudes of the distributions were scaled for clarity. The distributions are shown in a plane perpendicular to the photon propagation direction (see Fig. 11).

phase, since the final partial wave is the same and the phases cancel out. The last two interference terms, which do depend on the photoelectron phase, also contain a term which is linearly proportional to the degree of circular polarization of the incident photon and the angle ϕ. It is these terms which give rise to rise to sensitivity of the distributions to the helicity of the light and to left-right asymmetries in the distributions. The outcome of these contributions will be discussed in Sec. 4.3.

Since we will concentrate on two-photon ionization of atomic s electrons in the rest of this chapter, we take the opportunity here to present few examples of two-photon ionization of p electrons. Similarly as in Sec. 3.2.2, we will investigate the behavior of cross sections of two-photon ionization of $2p$ electrons of magnesium atom in the vicinity of nonlinear Cooper minimum. However, this time we consider ionization by linearly polarized light and study the dynamics of the corresponding photoelectron angular distributions. Figure 12 show the total two-photon ionization cross section for ionization of $p_{1/2}$ (solid black) and $p_{3/2}$ (dashed green) electrons in the vicinity of nonlinear Cooper minimum of the $p_{1/2}$ electron. Below, corresponding photoelectron angular distributions are shown at three photon energies; lower than, equivalent to and larger than the nonlinear Cooper minimum. The photoelectron angular-distributions can be understood from the consideration of interplay of ionization channels. There

are three possible nonrelativistic ionization channels, generally, the $p \to d \to f$ channel dominates [74], which results in the typical distributions such as the left- and rightmost plots of figure 12. However, this dominant channel vanishes at the nonlinear Cooper minimum and the distribution is determined by the symmetry of the other two channels (see Fig. 3). For this reason, the distribution for two-photon ionization of $2p_{1/2}$ electron of magnesium at the photon energy $\omega = 55.875$ eV strongly varies from the rest. It is also worth noting, that for two-photon ionization at the nonlinear Cooper minimum, the photoelectron emission does not follow the photon polarization vector, but is emitted perpendicularly to this direction. The shown distributions were scaled for clarity, but without the scaling the distribution corresponding to ionization of $p_{1/2}$ electron at the nonlinear Cooper minimum would be much smaller than the one for ionization of the $2p_{3/2}$ electron, due to the lower total cross section value.

4.2.3 Dependence on polarization of ionizing light

Already from single-photon ionization, it is well known, that the emission direction of an electron depends on the photon polarization. Often, the dominant emission direction is explained with the help of the direction of the electric field. This "rule of thumb" holds also for two-photon ionization, however, two-photon ionization offers some subtle differences. We will describe the electron emissions for two-photon ionization of s and p electrons below.

In the two-photon ionization, the photoelectron angular distribution shows more often than not the same behavior, quite independent of the atomic target and the coupling of the valence-shell electrons. Figure 13 displays such typical distributions for four different photon polarizations; circular, linear, elliptical, as well as for unpolarized photons. For the ionization by circularly or unpolarized photons, obviously, the photoelectron angular distributions are always axially symmetric and, thus, independent of the azimuthal angle ϕ. It is worth noting, that for two-photon ionization of unpolarized atoms by two completely circularly polarized photons, there is no photoelectron emission along the photon propagation direction. Indeed, the emission along this axis is forbidden by the conservation of projection of angular momentum. Since the helicity of the two photons is $\lambda_1 + \lambda_2 = \pm 2$, the change in the projection of angular momentum cannot be compensated by the photoelectron emitted along the photon propagation direction. However, for ionization by photons with a lower degree of circular polarization (i.e. $P_c < 1$), the electron emission along the quantization axis becomes possible. With ever decreasing degree of polarization, the distribution will become similar to the one for the unpolarized case. This can be also seen analytically from Eq. (4.3). For the completely circularly polarized case ($P_c = 1$), we have $\mathcal{P} = 0$ and $P_l = 0$. Therefore, the photoelectron distribution is given solely by the $\sin^4\theta$ distribution, which corresponds to $l = 2,\ m = \pm 2$ partial wave of the photoelectron. The pure dependence on the sine function analytically confirms the zero emission cross section in the photon propagation direction ($\theta = \phi = 0$). Similar conclusion can be drawn if one considers two-photon ionization of p electrons and considers the Eq. (4.4). If we now decrease the polarization purity, other partial waves will also contribute to the photoelectron distribution and the emission into forward direction will increase. For the case of two-photon ionization of atoms by linearly polarized light, the photoelectrons are dominantly emitted along the photon polarization direction. However, as we have seen in previous section, this rule can be broken under special circumstances, such as at the nonlinear Cooper minimum. From Eq. (4.3), we see that the distribution now depends also on the azimuthal angle ϕ, and that it contains contributions from both ionization channels.

Figure 13 shows the two-photon ionization of s electrons. The photoelectron an-

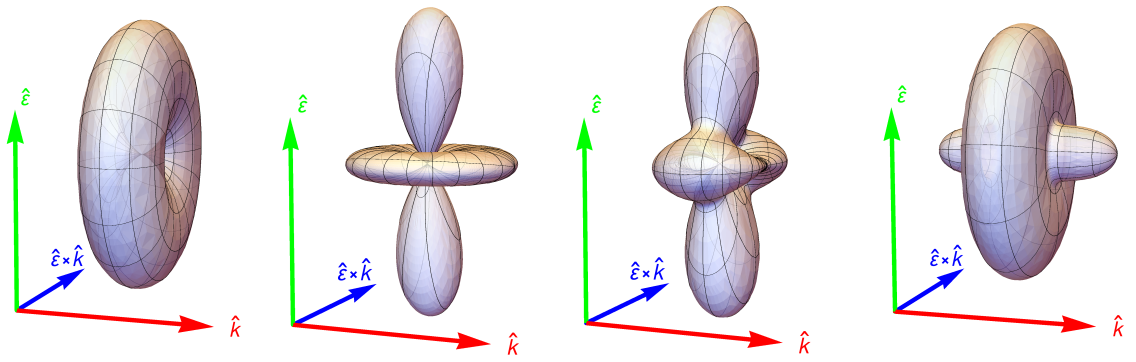

Figure 13: Typical photoelectron angular distributions for the nonresonant two-photon K-shell ionization of neutral atoms for incident photons polarized circularly ($P_c = 1$), linearly($P_l = 1$), elliptically ($P_c^2 = 1/2$, $P_l^2 = 1/2$), or unpolarized ($P_c = 0$, $P_l = 0$).

gular distributions for two-photon ionization of other shells generally posses similar properties as those, shown above. However, some features vary. For example, for two-photon ionization of p electrons by linearly polarized light, the emission in the plane perpendicular to the photon propagation and polarization directions is smaller. Analogously, for ionization by unpolarized light, the emission of photoelectrons along the photon propagation direction decreases with respect to the distribution shown in Fig. 13. These differences can be understood by the geometrical properties of partial waves with higher angular momentum, which posses the above described features.

Although the distributions of Fig. 13 generally provide a good description of the photoelectron emission direction for two-photon ionization of s electrons, we will present cases where significant deviations from these distributions occur due to screening or relativistic effects. While the screening effects are taken into account also in the nonrelativistic cross section (4.3), which can be characterized by two parameters, the expression is insufficient to describe relativistic processes. In the following section, the validity of the nonrelativistic description will be critically evaluated and its limitations will be shown. Moreover, the importance of the screening potential will be assessed.

4.2.4 Evaluation of relativistic and electron screening effects

Up until now, we have concentrated on the photoelectron angular distributions of two-photon ionization only within the electric dipole approximation. In the case of total two-photon ionization cross section, we have shown that the multipole effects can become important for heavy atoms. It is generally known, that photoelectron angular distributions are even more sensitive to the precise theoretical treatment. The multipole effects, for example, have been accessed in one-photon ionization through detection of photoelectron distributions in the vicinity of Cooper minimum or giant dipole resonance [45, 62, 78]. Therefore, it is reasonable to question the degree of validity of the simplified expression (4.2) in comparison to the exact treatment (4.1). Moreover, it was shown that the electron screening effects can influence the value of the total cross section. This implies that also the photoelectron distributions will be influenced. That is why we will compare our calculations for two-photon ionization of neutral atoms, with those for ionization of hydrogen-like atoms. For convenience, we will restrict our analysis to two-photon ionization of K shell electrons only.

Figure 14 presents the photoelectron angular distributions of the two-photon K-shell ionization of neutral and hydrogen-like atoms for two excess energies ($\varepsilon = 1.05,\ 1.40$) and for four different elements (Ne, Ge, Xe, U). The solid black distributions correspond to the relativistic calculations of two-photon ionization of neutral atoms, while

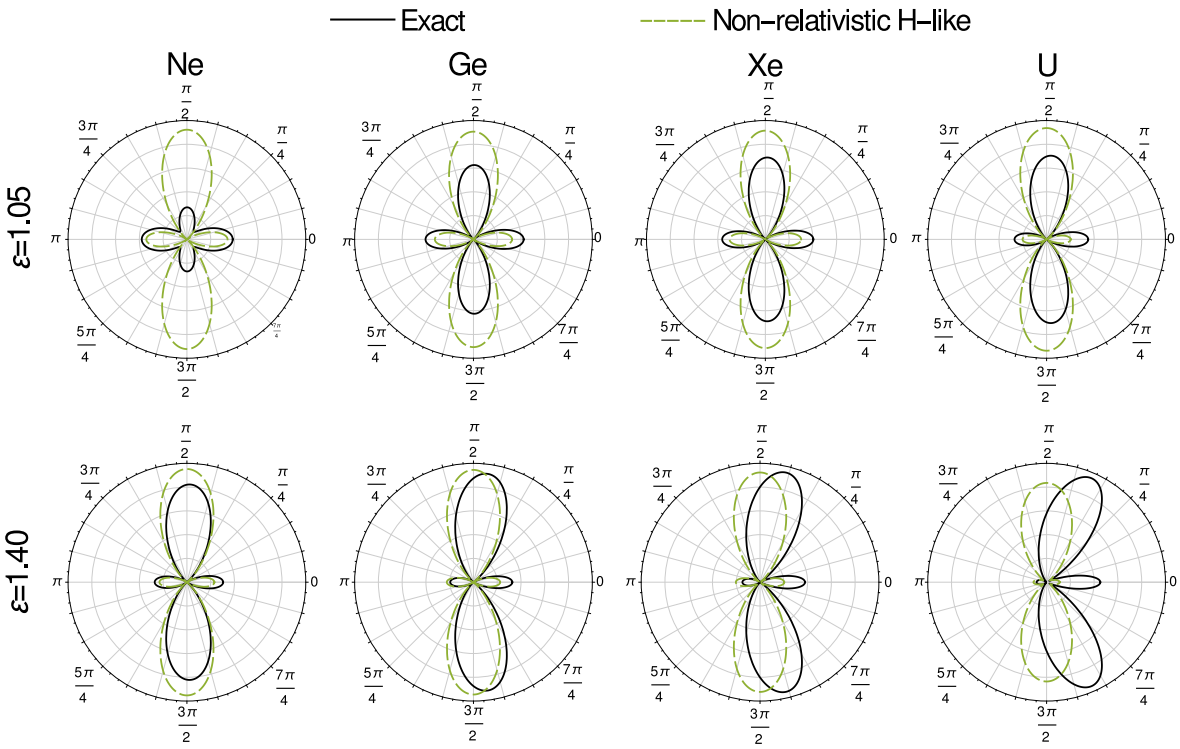

Figure 14: Screening and multipole contributions to the two-photon K-shell ionization of neutral Ne, Ge, Xe, and U atoms, using linearly polarized photons with $\varepsilon = 1.05$ (upper row) and $\varepsilon = 1.40$ (lower row) excess energies. An exact relativistic computation of two-photon ionization of neutral atoms (solid black) is compared with a nonrelativistic calculation for ionization of hydrogen-like ions (dashed green) is presented. At $\varepsilon = 1.05$ excess energy, the photoelectron emission from a neon atom (upper-left figure) significantly decreases along the polarization axis due to the screening effects. For uranium $\varepsilon = 1.40$ (lower-right figure), the emission into the incident photon direction is highly promoted due to relativistic effects. In order to compare the results for neutral atoms and hydrogen-like ions, the distributions have been scaled in the given plane. All plots were obtained for $\phi = 0$, i.e. in the $\hat{\boldsymbol{\varepsilon}}\hat{\boldsymbol{k}}$-plane (see figure 11).

the dashed green distributions correspond to the nonrelativistic calculations of two-photon ionization of hydrogen-like ions. The results of the latter serve as reference distributions, since they are neither affected by the relativistic nor screening effects. Therefore, the comparison of the corresponding results for these two calculations gives us the necessary insight on how the relativistic and multipole contributions affect the angular emission of photoelectrons in the two-photon K-shell ionization of atoms and ions.

There are various relativistic contributions to the cross sections. For the total cross section, the relativistic contraction of the wave function may result in a reduction of up to 30%, while the higher multipoles give rise to rather small changes only (see section 3.2.3). For the photoelectron angular emission, in contrast, the different multipole contributions may significantly alter the distribution. These contributions sensitively depend on the nuclear charge and the energy of the incident photons. For ionization of medium and heavy atoms with high energetic photons, forward emission of the photoelectron is enhanced, while the backward emission decreases. This distortion of the angular distribution can be clearly seen in Fig. 14, together with the nuclear charge and photon energy dependencies. Although, we present results for incident linearly polarized light, an identical change of the distributions is found for all types of polarization. A similar behavior was found in relativistic calculations of hydrogen-like

atoms [30]. Interestingly, the distortion of the distribution due to the multipole effects in two-photon ionization of neutral atoms is comparable with the one for hydrogen-like ions. This can be understood from Fig. 14. Since the importance of multipole contributions depends more strongly on the relative photon energy (the excess energy), the results do not significantly differ if the nuclear potential is partially screened by the electrons in higher shells.

From the analysis of relativistic effects, it may seem, that neglecting the screening effects of inactive electrons would not yield a significantly different results, as long as we include higher multipole orders of the photon field. However, from Fig. 14, it can be seen that following this rushed conclusion could lead to large errors. This is because the screening effects are significant for photon energies near the ionization threshold and light elements. The influence of the screening effects was found strongest for the two-photon ionization of neon, where the electron emission along the photon propagation axis exceeds the emission along the linear polarization axis. This result can be best understood in the simplified electric dipole picture, where there are only two ionization channels present; s channel and d channel, where s and d refer to the partial waves of the emitted photoelectron. The contribution of the s channel to the cross section is angle-independent, and is therefore spherically symmetric. On the other hand, the contribution of the d channel is similar to the distribution of two-photon ionization by linearly polarized light with most photoelectrons emitted along the photon polarization direction, see Fig. 13. Generally, the ionization channel with higher angular momentum is dominant, hence, only small contribution to the distribution arises from the s channel. However, in Sec. 3.2, we have shown that due to the screening effects, the dominant d channel drops down for light elements in near-threshold ionization, while the amplitude of the s channel increases. This is exactly what we can see in Fig. 14. The emission along the polarization axis sharply decreases (d-channel contribution) and the emission into all direction slightly increases (the spherical contribution of the s-channel). Instead, if we consider the case of ionization by completely circularly polarized light, i.e. $P_c = \pm 1$, only the d channel contributes to the cross section. More specifically, only the d channel with projection of orbital angular momenta $m_e = \pm 2$ contributes. This leads to the typical doughnut shape distribution. Since there is only one active channel, screening effect lead solely to the decrease of the magnitude of the cross section. As none of the described behavior has been observed in two-photon ionization of hydrogen-like ions, it must therefore arise from the additional screening potential created by the inactive electrons.

A similar analysis to evaluate the importance of relativistic effects can be of course carried out for ionization of any electron shell. Although we will not perform such analysis, we can utilized our gained experience to make an educated guess of what results we would expect. From Fig. 14 it is apparent, that screening effects can alter the photoelectron distributions significantly near the two-photon ionization threshold due to changing amplitudes of the ionization channels. This dynamic behaviour of the ionization channels is typically rather difficult to predict, without a calculation. It is, however, expected that this effect would occur in ionization of higher shells as well. The relativistic effects are generally easier to predict. Figure 14 shows, that the distortion of the photoelectron distributions into the forward direction are more significant for tightly bound electrons and for high photon energies. Hence, simply by comparing the magnitude of the Coulomb potential, one could quickly estimate the relativistic effects for two-photon ionization of electrons with nonzero angular momentum.

4.3 Elliptical dichroism

4.3.1 What is dichroism?

It is well known, that when unpolarized atoms or mirror symmetric molecules are irradiated with an ionizing *circularly* polarized light, the ionization cross sections are identical for the left- and right-handedness of the light. When the atoms are initially polarized, in magnetic field or if the molecules are chiral, however, the cross sections generally depend on the handedness of the light [125–128]. The different outcome of cross sections for left- and right- polarized light, so-called *circular dichroism*, has been explored for many years. Since its discovery, it has become an inevitable tool for studying biomolecules [129], and for determining the structure of chiral molecules [130]. However it has also found an application in other fields; for example in polarization effect control [131], or control of optical activity in metamaterials [132].

Three decades ago, observations of left-right asymmetries in photoelectron angular distributions in above-threshold ionization of unpolarized noble gas atoms by elliptically polarized light were observed for the first time [133], and it was demonstrated, that dichroism itself does not require a chiral target, but arises also from nonlinear interactions with elliptically polarized light. Although the origin of the asymmetries remained unclear to the authors at that time, first reasoning for this asymmetry could be found already in an earlier work of that year [134], in which this asymmetry remained unnoticed. The dots were soon connected by two theoretical groups [135, 136], who provided a brief explanation of the phenomenon based on lowest-order perturbation theory. While these theories fully describe the observed elliptical dichroism, a lucid explanation is still missing until the present.

Goreslavski *et al.* have shown that the asymmetries in the angular distributions can be understood from the changes in Coulomb potential as seen by the emitted electron. From a theoretical point of view, this means that the widely used Keldysh approximation is insufficient the dichroism, and hence, that the binding potential needs to be treated explicitly [137, 138]. In the 90s, however, such studies on the elliptical dichroism were restricted by the rather low energies of the available lasers. These lasers only allowed two schemes to be realized, either the production of very slow photoelectrons due to the absorption of the minimal number of photons necessary for an ionization to occur, or by making use of above-threshold ionization by absorbing additional photons in the focus of strong laser fields [124, 139, 140]. The first option was performed experimentally e.g. for the two-photon ionization of the rubidium $5s\ ^2S_{1/2}$ electron [115, 141], with the emphasis on extracting relative phases and transition amplitudes from the photoelectron angular distribution [142]. These experiments gave rise to an unexpected cross section ratio of the two fine structure channels (partial d wave), and suggested much stronger spin-orbit effects than predicted theoretically [143]. Further studies on the elliptical dichroism were performed for near-threshold energies, and confirmed strong asymmetries for several atoms [64, 66, 144]. Elliptical dichroism is generally always present in the two-photon ionization photoelectron angular distributions. However, it is typically difficult to estimate the magnitude of the dichroism parameter without performing detailed calculations.

To make the notation in this chapter simpler, we define $d\sigma_\pm/d\Omega$ as the angle-differential cross sections for ionization by right- or left-handed light. With this definition, we can analytically describe the dichroism using a normalized parameter given by

$$\Delta_{\mathrm{ed}} = \frac{d\sigma_+/d\Omega - d\sigma_-/d\Omega}{d\sigma_+/d\Omega + d\sigma_-/d\Omega}. \tag{4.5}$$

These cross sections could be in a general case also replaced by the total cross sec-

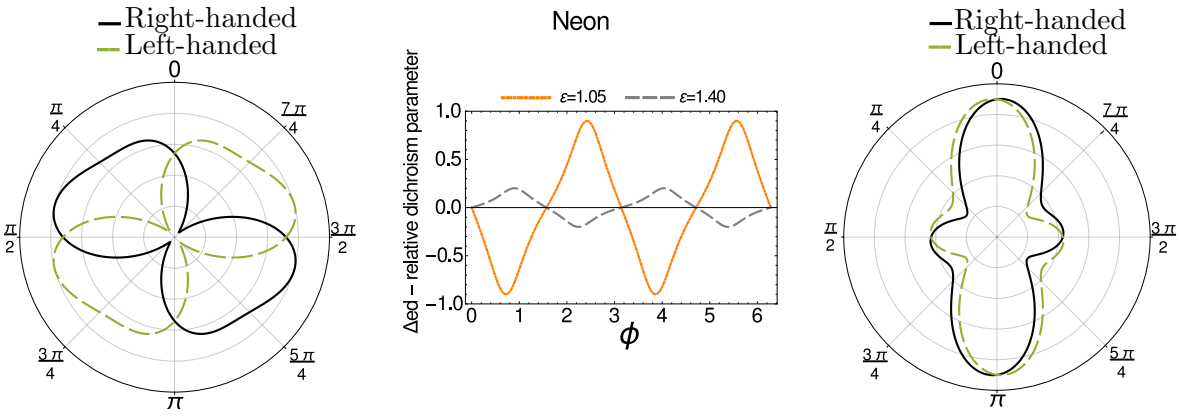

Figure 15: Elliptical dichroism in nonresonant two-photon K-shell ionization of neutral neon. The angular distributions are presented in the plane perpendicular to photon propagation direction (the polar angle $\theta = \pi/2$) for two photon excess energies; $\varepsilon = 1.05$ (left) and $\varepsilon = 1.40$ (right). The photon polarization is $P_l = 1/\sqrt{2}$ and $P_c = 1/\sqrt{2}$ (solid black) or $P_l = 1/\sqrt{2}$ and $P_c = -1/\sqrt{2}$ (dashed green). The sensitivity of the dichroism is clearly visible from the distributions as well as from the relative dichroism parameter Δ_{ed} (middle).

tions, however, in the case of two-photon ionization of unpolarized targets, this would always yield a zero dichroism. The dichroism parameter takes values in the interval $\Delta_{\rm ed} \in [-1, 1]$, where $|\Delta_{\rm ed}| = 1$ describes the maximum possible effect. To express the dichroism parameter explicitly, let us write the parameter for two-photon ionization of atomic s electrons, for which the nonrelativistic limit of the above expression takes the form

$$\Delta_{\rm ed} = \frac{-12 U_s U_d^* P_l P_c \sin(\Delta_s - \Delta_d) \sin^2\theta \sin(2\phi)}{d\sigma_+/d\Omega + d\sigma_-/d\Omega}, \tag{4.6}$$

where the denominator of this expression yields twice the Eq. (4.3) except of the the very last term. The superscript in the transition amplitude was once again dropped for brevity, i.e. $U_d = U_d^{(p)}$. Equation (4.6) demonstrates that the dichroism parameter is given by the helicity dependent term(s) normalized to all terms independent of the light handedness. Its magnitude is also strongly determined by the difference of the photoelectron partial wave phases.

To allow the reader to get first intuitive feeling about the elliptical dichroism and to demonstrate its magnitude can vary, we present an example. In figure 15, we show the photoelectron angular distributions in the polarization plane for two-photon ionization of $1s$ electron of neon atom by elliptically polarized light, with $P_l^2 = 1/2$ and $P_c^2 = 1/2$. The figure shows distributions for ionization by photons with excess energies of $\varepsilon = 1.05$ (left) and $\varepsilon = 1.40$ (right) as well as the dichroism parameter for both cases (middle).

This figure clearly shows the energy dependence of the elliptical dichroism. While for low energies, the difference between ionization the atom by right $P_c = 1/\sqrt{2}$ and left $P_c = -1/\sqrt{2}$ handed light is large and the dichroism parameter nearly reaches unity for four given values of ϕ, the dichroism for the higher energy is much weaker. A similar behavior applies to the dependence on nuclear charge, with the dichroism being strongest for neon atom. The large value of elliptical dichroism parameter here is due to the screening effects also discussed in previous section. The otherwise dominant d ionization channel decreases, and s channel increases, the relative amplitude of the interference term of Eq. (4.6) increases, and hence, the sensitivity to the handedness of light increases. As shown in Ref. [64], the screening effects for two-photon ionization of s electrons are strongest for neon, therefore, even the dichroism is largest for ionization of the neon atom. Since the screening effects are fully encapsulated in the transition

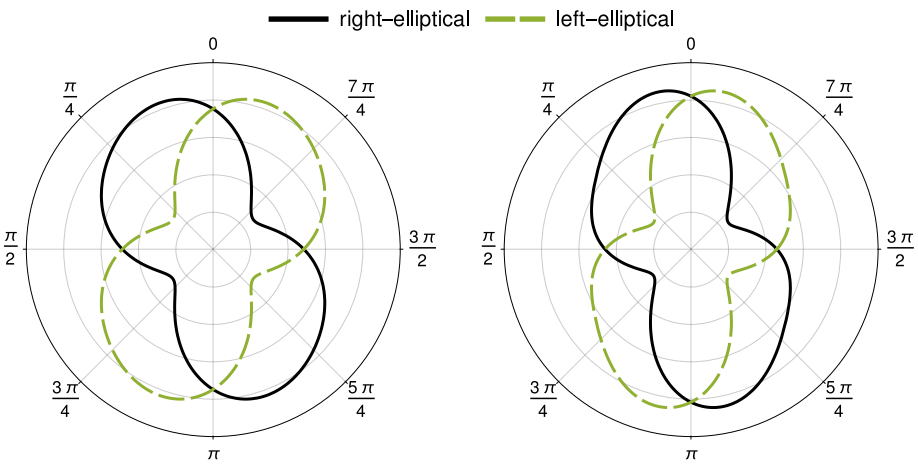

Figure 16: Nonresonant two-photon ionization of $3p$ electron of krypton atom by elliptically polarized light with energy $\omega = 235$ eV. The plot demonstrates the low sensitivity of elliptical dichroism to the ellipticity of light. The left-hand side figure shows the photoelectron distribution for two-photon ionization by 50% linearly and 50% circularly polarized light, while the right-hand side figure shows distribution corresponding to 80% linearly and 20% circularly polarized light. The angular distributions are presented in the plane perpendicular to photon propagation direction (the polar angle $\theta = \pi/2$), see Fig. 11.

amplitudes and since the relativistic effects are low for light elements, the elliptical dichroism can be described well with the nonrelativistic expression (4.6).

We will discuss the origin and characteristics of the elliptical dichroism on example of two-photon ionization of s electrons. However, this does not mean that the effect appears only in this case. It is actually quite contrary. The elliptical dichroism appears generally in two-(or even multi-)photon ionization of any atomic shell, independent of the angular momentum. The terms which give raise to the elliptical dichroism, i.e. those which linearly depend on the degree of circular polarization of the ionizing light, can be seen in the interference in Eq. (4.4).To briefly support this claim by a numerical calculation, we present figure 16, where the photoelectron angular distribution for two-photon ionization of the $3p$ electrons of neutral krypton by elliptically polarized light are shown. The distributions correspond to ionization either by right-(solid black) or left- (dashed green) handed light. This figure also demonstrates the dependence of the elliptical dichroism on the ellipticity of the ionizing light. The left plot was generated for $P_c^2 = 1/2$ and $P_l^2 = 1/2$ while the plot on the right-hand side corresponds to $P_c^2 = 1/5$ and $P_l^2 = 4/5$. Although the dichroism is more pronounce when the photons are half circularly polarized, the dichroism is still strong even at 20% of circular polarization.

4.3.2 Origin of the elliptical dichroism

The concept of circular dichroism is well known not only in the fields of atomic and molecular physics but is also applied in fields such as biology. The explanation of circular dichroism which uses the geometrical picture of chiral molecules or oriented atoms is widely accepted and became for many the default condition for occurrence of sensitivity to photon handedness. That is why elliptical dichroism is startling at first, since dichroic behavior is obtained with a spherically symmetric target. The aim of this subchapter is to provide a simple and intuitive explanation of the origin of the elliptical dichroism to widen our understanding of dichroism phenomena. In order to explain where the elliptical dichroism arises from, we take the example of two-photon ionization of s electrons for simplicity, although the effect is generally present in multi-photon ionization of any atomic (or molecular) shell. Elliptical dichroism

arises already within nonrelativistic electric-dipole approximation [66, 124], and does not require treatment of the electron spin. Let us, therefore, carry out the explanation within these approximations.

Consider an s electron in a bound (atomic) state, as well as elliptically polarized photons. After the interaction of the s electron with both photons, the electron either undergoes an $s \to p \to s$, or $s \to p \to d$ transition, and will be released eventually with kinetic energy ε into some direction θ and ϕ (see Fig. 2). The photoelectron is assumed to be in a pure state, and its wave function can be simply written as a sum of just two partial waves

$$\psi_\varepsilon(\mathbf{r}) = a_0\psi_{\varepsilon 00}(\mathbf{r}) + \sum_{m_d} b_{m_d}\psi_{\varepsilon 2m_d}(\mathbf{r}), \tag{4.7}$$

where $m_d = 0, \pm 2$ only, since the quantization axis is chosen along the photon propagation direction. Obviously, the s and d partial-wave amplitudes a_0 and b_{m_d}, respectively, contain all information about the dynamics of the ionization process,

$$a_0, b_{m_d} \propto \rho_\gamma^{\lambda_1\lambda_1'}\rho_\gamma^{\lambda_2\lambda_2'}, \tag{4.8}$$

and their exact expressions can be obtained from the photon density matrix similar similar as in Ref. [142]. The propagation direction of the photoelectron itself is completely characterized by its probability density

$$\begin{aligned} |\psi_\varepsilon|^2 &= |a_0\psi_{\varepsilon 00}|^2 + |\sum_{m_d} b_{m_d}\psi_{\varepsilon 2m_d}(\mathbf{r})|^2 \\ &+ \sum_{m_d} a_0^* b_{m_d}\psi_{\varepsilon 00}^*(\mathbf{r})\psi_{\varepsilon 2m_d}(\mathbf{r}) \\ &+ \sum_{m_d} a_0 b_{m_d}^*\psi_{\varepsilon 00}(\mathbf{r})\psi_{\varepsilon 2m_d}^*(\mathbf{r}). \end{aligned} \tag{4.9}$$

We shall analyze this expression in order to explore the left-right asymmetry in the photoelectron angular distribution in further detail. Mathematically speaking, this means that we are looking for an antisymmetric contribution in Eq. (4.9), which changes its sign under the coordinate transformation $y \to -y$, or equivalently $\phi \to -\phi$. Since the angular dependence of the wavefunction is described by the spherical harmonics, we easily see that only the imaginary part of spherical harmonics, $\mathrm{Im}[Y_{2\pm 2}(\theta, \phi)]$ changes its sign with the $\phi \to -\phi$ coordinate transformation. Since this term is complex, we can conclude that the antisymmetric contribution must be contained only in the interference terms.

In the dipole approximation, the well-known selection rules provide a simple relationship between the helicities λ_1 and λ_2 (as well as λ_1' and λ_2') of the two photons for obtaining a particular projection of the angular momentum m of each partial wave. For example, in order to obtain $m = \pm 2$, both photons must have the same helicity $\lambda_1 = \lambda_2$, while we must have $\lambda_1 = -\lambda_2$ for $m = 0$. We therefore expect, the ϕ-dependent part of the interference to be proportional to $\propto \sum_{\lambda_1\lambda_1'} Y_{0\lambda_1-\lambda_1}Y_{2\lambda_1'+\lambda_1'}^*\rho_\gamma^{\lambda_1\lambda_1'}\rho_\gamma^{\lambda_1-\lambda_1'} \propto iP_lP_c\sin(2\phi)$. This is exactly the antisymmetric term responsible for the dichroism which changes sign under the $\phi \to -\phi$ transformation, or equivalently, changes sign upon a change of photon handedness. Moreover, we can see, that for pure linear, or circular polarization ($P_c = 0$, or $P_l = 0$) this term vanishes. One can carry out a similar analysis to show, that there is no elliptical dichroism in photoelectron angular distribution of one-photon ionization of a spherically symmetric target, and hence show that elliptical dichroism is a purely nonlinear phenomenon.

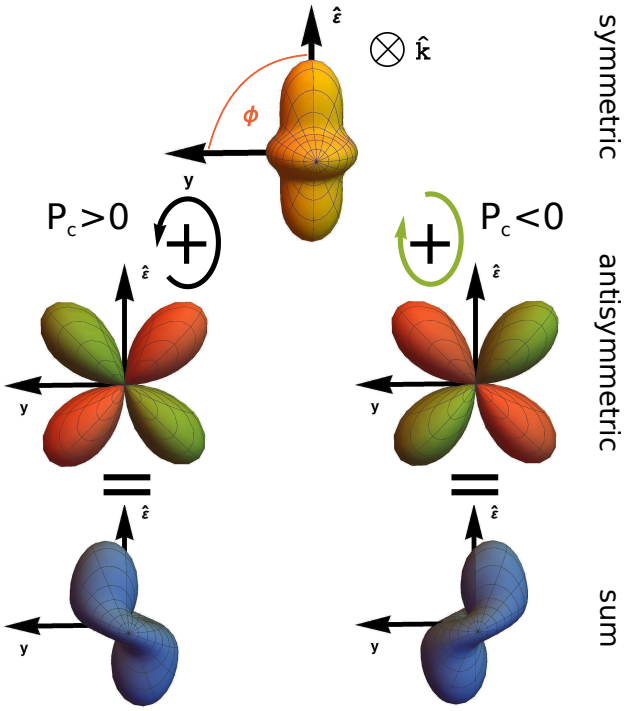

Figure 17: (Color online) The origin of elliptical dichroism in the photoelectron angular distribution of two-photon ionization of an s-electron. We can separate the distribution into a symmetric "core" contribution (top) and an antisymmetric "dichroic" contribution (middle row). The dichroic part is given by a $\sin(2\phi)$, and has therefore positive (green) and negative (red) intervals. The sum of the "core" and "dichroic" contributions gives us the final photoelectron distribution (bottom row).

The geometrical analysis given above predicts the presence of the dichroism. However, the photoelectron angle-differential cross section can be of course derived rigorously. The explicit expression for the photoelectron angular distributions is given by Eq. (4.3). We can decompose the differential cross section into a symmetric and an antisymmetric contributions. Figure 17 visualizes these two contributions to the angle-differential cross section. The "core" symmetric part (orange) contains the squared terms of Eq. (4.9) as well as the symmetric part of the interference term. The last term of Eq. (4.3) represents the "dichroic" asymmetric part (red-green), and is the only term depending on the photon handedness. The signs of the circular Stokes parameter P_c, and the phase difference $\delta_s - \delta_d$ determine the intervals for which the "dichroic" term contributes constructively (green), or destructively (red). The sum of the "core" and the "dichroic" contributions gives the final photoelectron angular distribution (blue). The relative contributions of the "core" and "dichroic" parts, and hence the magnitude of the left-right asymmetry, are consequently determined by the ratio of the partial waves U_d/U_s. The asymmetry in photoelectron angular distribution is quantified by the dichroism parameter Δ_{ed} given in Eq. (4.5).

4.3.3 Maximum of elliptical dichroism

Since we now know, why elliptical dichroism occurs in two-photon ionization of (unpolarized) atoms, we can explore some of its properties. For example, looking at figure 15, it is clear that elliptical dichroism can be either strongly pronounced, or only weak. This "strength" of elliptical dichroism of course depends on the parameters, which determine the photoelectron angular distributions. In nonrelativistic approximation and for two-photon ionization of s electrons, there are two parameters, the amplitude ratio

$u \equiv U_d/U_s$ and photoelectron partial-wave phase difference $\delta' \equiv \delta_s - \delta_d$. Naturally, we can now ask ourselves, what values should these two parameters take, such that the elliptical dichroism is maximized? This is a question which we will answer in this subsection. As maximum of elliptical dichroism, we use simply the equation (4.6). This means we will be searching for the maximum of the dichroism parameter in a single direction given by the angles θ and ϕ.

To find the maximum dichroism, we concentrate on distributions in the polarization plane (perpendicular to the photon propagation direction, i.e., $\theta = \pi/2$). Moreover, since the FEL pulses possess a high degree of polarization, we can consider a fully polarized beam which is half linearly and half circularly polarized, $P_l^2 = 1/2$ and $P_c^2 = 1/2$. We can use the Eq. (4.6) to obtain the expression for elliptical dichroism parameter. By analyzing the second derivatives of Δ_{ED}, we find that the dichroism parameter reaches its extrema (+1 or −1) at particular azimuthal angles $\phi_{\max}$, and corresponding values of the amplitude ratio $u_{\max} = 2[(3\cos(2\phi_{\max}) + \sqrt{2})^2 + 8]^{-1/2}$. The angle $\phi_{\max}$ can be obtained from a fit to numerical solutions and is given by $\phi_{\max}(\delta') = 0.95\delta' - 0.33\delta'^2 + 0.06\delta'^3$ for $0 < \delta' < \pi$, and $\phi_{\max}(2\pi - \delta')$ for $\pi < \delta' < 2\pi$. Note that at this angle either $d\sigma_+/d\Omega = 0$ or $d\sigma_-/d\Omega = 0$. The elliptical dichroism at this angle can, therefore, be used for sensitive extraction of the phase information and amplitude ratios. The important conclusion is that for any nonzero phase difference, there exists an amplitude ratio for which the elliptical dichroism reaches its maximum. Of course, we cannot dictate nature what the amplitude ratio should be. We can, nevertheless, search for photon energies ω, for which the transition amplitudes fulfill the above condition (assuming that δ' varies much slower than u). To achieve the optimal ratio, we can use our arguments from definition of nonlinear Cooper minimum (see Sec. 2.2.2) and state that the maximum elliptical dichroism can be obtained by tuning the photon energy such that the virtual intermediate state lies between two resonances. Then, by fine-tuning the photon energy, we will find two u_{max} values in the near vicinity of the nonlinear Cooper minimum. For future reference, we call the photon energies which yield u_{max} the "tune-in" photon energies $\omega_{\max}$.

Before we demonstrate our findings with an example, we would like to draw a brief conclusion. Maximum elliptical dichroism in the photoelectron angular distribution can be obtained by tuning in the photon energy $\omega_{\max}$ so that after absorption of one photon, an s electron of an atom is promoted to an intermediate virtual state between np and $(n+1)p$ resonances, with the exception of high n states, for which the corresponding width is comparable to the energy separation of the resonances.

We will demonstrate the detection of maximum elliptical dichroism on an experimentally plausible example of two-photon ionization of ground state helium, which has already been used as a target for various atomic studies in the past decade [45, 145, 146], and where two-photon ionization is the dominant process. To obtain maximum dichroism, $|\Delta_{\mathrm{ed}}| = 1$, in two-photon ionization of He, we need to tune in a photon energy which promotes one of the $1s$ electrons into continuum, through a virtual intermediate state sandwiched between two resonances; $1s^2 \to 1s2p$ and $1s^2 \to 1s3p$. The resonances are clearly visible in the plot of total ionization cross section in Fig. 18 (yellow). The red plot represents the normalized ratio of the partial waves $(|U_s| - |U_d|)/(|U_s| + |U_d|) \in [-1, 1]$. According to the propensity rules [74], upon absorption of a photon, transitions corresponding to $l \to l + 1$ should be favored, and the normalized partial-wave ratio should be negative. Figure 18 shows, that this is generally true, however around the resonances, the ratio strongly deviates from these rules. The amplitude ratio becomes positive at a point, where the dominant contributions from Eq. (2.24) cancel each other out, and it reaches unity when the U_d channel is equal to zero. Between these two significant points, the amplitude ratio passes the optimal ratio (horizontal gray line), where maximum elliptical dichroism, $|\Delta_{\mathrm{ed}}| = 1$ can be observed. After the phase

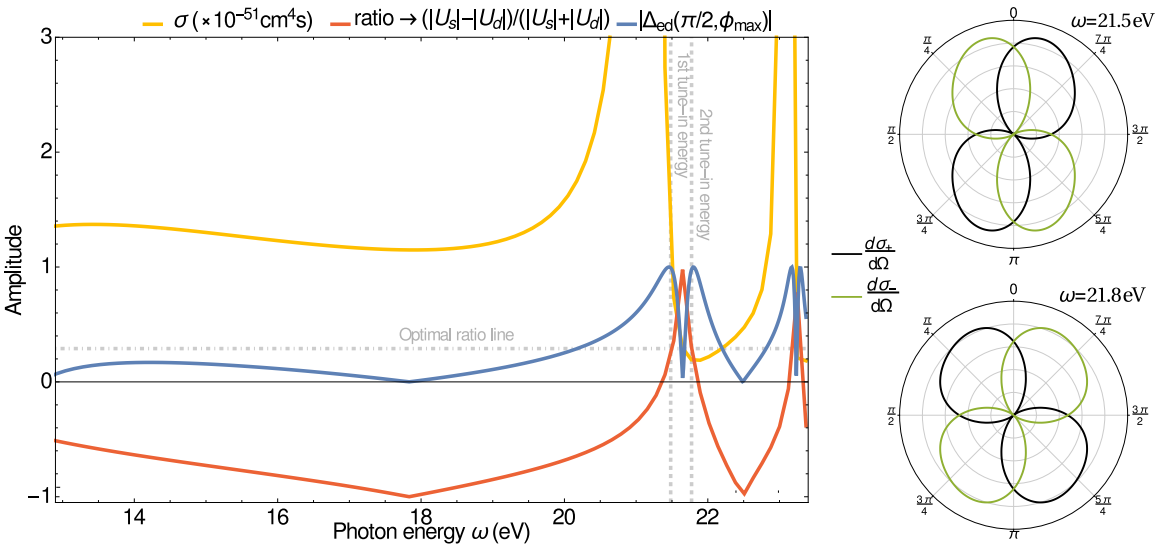

Figure 18: (Color online) Total cross section (yellow), partial-wave ratio (red), and elliptical dichroism parameter (blue) as functions of single photon energy. The horizontal gray dot-dashed line signifies the optimal ratio for obtaining $|\Delta_{\rm ed}| = 1$. This line intersects the partial-wave ratio at two tune-in energies (marked by two gray dotted vertical lines). Photoelectron angular distributions corresponding to these two intersections are shown on the right side of the figure. The angular distributions are presented in the plane perpendicular to photon propagation direction (the polar angle $\theta = \pi/2$), see Fig. 11.

jump induced by transition of U_d through zero, the amplitude ratio decreases, and crosses the optimal ratio line for a second time. The fulfillment of the optimal ratio are also clearly visible in the blue plot of the $\Delta_{\rm ed}$ (elliptical dichroism at $\phi_{\rm max}$, which maximizes the effect) as a function of photon energy, with the two peaks between the $2p-3p$ resonances (and another two between the $3p-4p$ resonances), each representing the maximum possible dichroism. The corresponding photoelectron angular distributions for these maxima are provided on the right-hand side of Fig. 18 in the polarization plane ($\theta = \pi/2$) as functions of ϕ, for both left-(green) and right-(black) elliptically polarized light. In a real experiment, these distributions could be influenced by the bandwidth of the incoming laser beam. However, in the case of helium, the width would be lower than < 0.1 eV. Our calculations show, that such an energy deviation would not be significantly reflected in the measured photoelectron distributions. These calculations supported a proposal sent to the free-electron laser facility FERMI in Triest, Italy. Unfortunately, the submitted proposal (proposal ID: 20184040) was not granted a beamtime, however, the proposal was resubmitted (proposal ID: 20194083) and is under scientific evaluation (at the time of writing).

4.4 Comparison with experiment

In contrast to the total cross section, the photoelectron angular distributions provide more sensitive tool to study light-matter interaction. Beside carrying the information about photoelectron phase, the dependence on incident photon polarization and the contributions of higher multipole orders of the electron-photon interaction are higher than for the angle-integrated cross sections. Furthermore, while one needs detailed knowledge of the incident beam properties to accurately extract total cross sections from measured electron, ion or fluorescence photon yields, the photoelectron angular distributions depend less on some beam parameters such as intensity. Carefully carried out experiments can, therefore, lead to precise understanding of ionization processes. Unfortunately, in practice, it is more challenging to detect the angular distributions

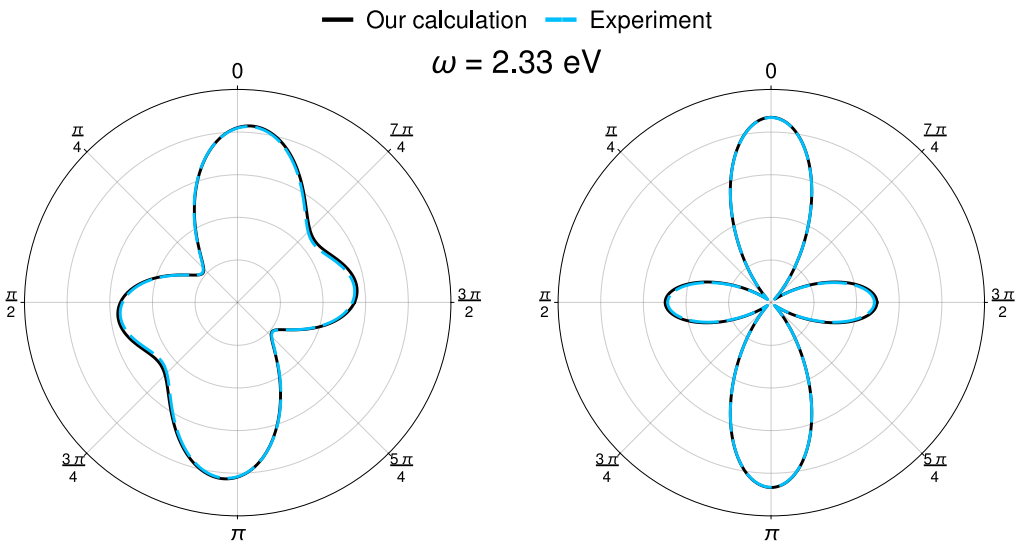

Figure 19: Two-photon ionization of $5s$ electron of neutral rubidium at photon energy $\omega = 2.33$ eV. The experimentally measured values (dashed blue) are in excellent agreement with the calculated distributions (solid black). Two-photon ionization by elliptically, $P_l^2 = 1/2$ and $P_c^2 = 1/2$, (left) and linearly, $P_l^2 = 1$ and $P_c^2 = 0$, (right) polarized light are shown. The plots are shown in the plane perpendicular to photon propagation direction (the polar angle $\theta = \pi/2$), see Fig. 11.

of photoelectrons than to simply register particle counts. Nevertheless, there are techniques to carry out angle-resolved experiments.

The angular distributions of photoelectrons can be experimentally detected using various instruments. For example, it is possible to use a set of microchannel plates followed by a phosphor screen [56, 115, 141]. The distributions are imprinted on the phosphor screen and recorded by a CCD camera. Another approach is to obtain the spatial resolution by arranging several independently operating time-of-flight spectrometers in a circle and place them in a desired plane around the interaction area [45, 46, 147]. A widely used detection method is using the velocity map imaging scheme, where the expanding photoelectron distributions are projected by an electrostatic lens to a two-dimensional position sensitive detector in a velocity map imaging, e.g. [148].

In this thesis, we dominantly concentrate on two-photon ionization of K or L shell electrons. However, available experimental data corresponding to two-photon deep-shell ionization are extremely scarce. In order to present comparison of our calculated data with more than one experimentally measured data, we will make an exception and present cross sections for two-photon ionization of valence shells. Wang *et al.* published their experimentally measured photoelectron angular distributions for non-resonant two-photon ionization of rubidium atoms [115]. In their experiment, they ionized the $5s$ electron of rubidium ($\epsilon_{6s} = 4.17$) atoms at various wavelengths as well as linear and elliptical photon polarization, and detected the slow photoelectrons. Similar experiment has been already performed before [114]. In figure 19, we present the comparison of our calculations with the measure values from [115] for both, ionization by elliptically and linearly polarized light. As it is apparent from the figure, excellent agreement between measured and calculated values was achieved.

In 2013, Ma *et al.* [56] published their results on two-photon ionization of helium which they carried out using the SACLA free-electron at the SPring-8 facility in Japan. The photoelectron angular distributions were recorded by a velocity map imaging spectrometer at four photon energies (20.3, 21.3, 23.0 and 24.3 eV). The lowest energy was chosen in a way it is well below the excitation energy of the ground state helium to the $1s2p\ ^1P$ state, where the two-photon ionization is nonresonant. The two inter-

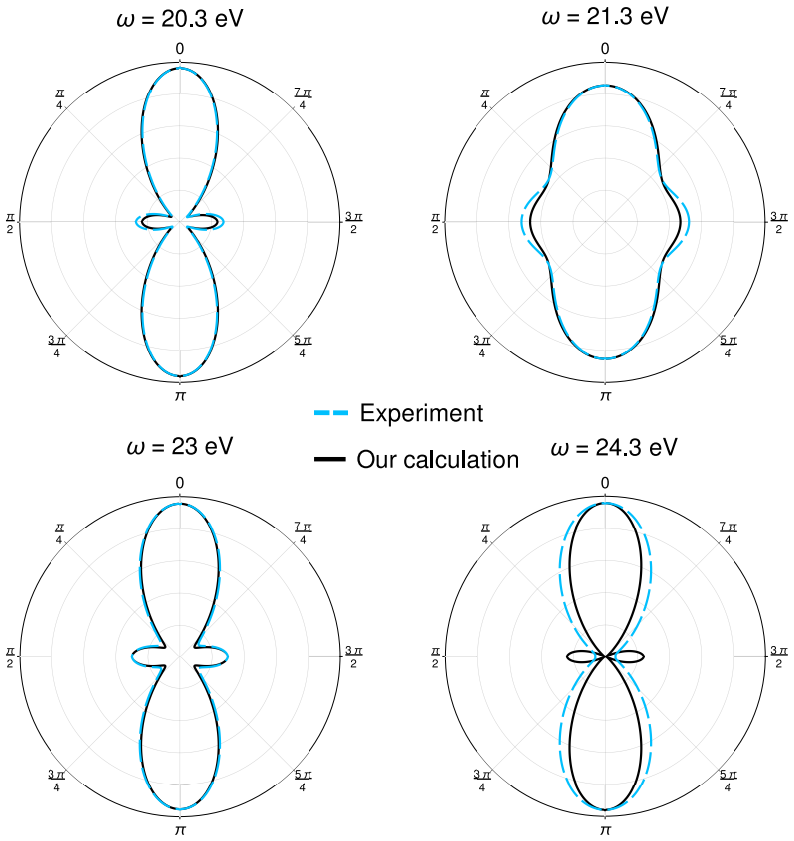

Figure 20: Two-photon ionization of neutral helium. Perfect agreement is reached between the experimentally measured (dashed blue) [56] and our calculated (solid black) distributions. The photon energy of 20.3 eV corresponds nonresonant two-photon ionization, the two-energies 21.3 and 23.0 eV promote one of the electrons between two resonances and populate the $1s2p\ ^1P$ or $1s3p\ ^1P$ states, the last photon energy 24.3 eV populates the Rydberg manifold. All plots were obtained for $\phi = 0$, i.e. in the $\hat{\boldsymbol{\varepsilon}}\hat{\boldsymbol{k}}$-plane (see figure 11).

mediate photon energies can excite the helium ground state into $1s2p\ ^1P$ or $1s3p\ ^1P$ states due to the beam bandwidth. The last energy corresponds to excitation of one of the helium electrons to the Rydberg manifold $1snp\ ^1P$. From the measurements, the asymmetry parameters and amplitude ratios were extracted which can be conveniently utilized for a comparison with theoretical values. Figure 20 presents the experimentally measured distributions (dashed blue) which are in a perfect agreement with our calculations (solid black). Since the two-photon ionization of $1s$ electrons has only two nonrelativistic channels (see Fig. 3), it is not difficult to deduce individual contributions of the channels to the presented photoelectron angular distribution. Generally, the $s \to p \to d$ wave dominates the process [74], which results in the typical dipole distribution with a ring around the origin. However, the second lowest energy lies between two resonances, at a point near the nonlinear Cooper minimum (Sec. 2.2.2), and hence the relative contribution of the $s \to p \to s$ channel increases and the distribution becomes more spherical. According to our calculations, if the measurement would be performed at $\omega = 21.65$ eV, the contribution from the d channel would vanish and the photoelectron angular distributions would be spherically symmetric.

5 Polarization Transfer from Ionizing Light to a Target Atom

In previous sections, we studied the two-photon ionization process and its corresponding cross sections. In particular, we paid attention to creating an inner-shell vacancy in s or p electronic shell and investigated the number and angular distribution of emitted electrons. Now, we would like to consider the same process, but instead of electrons we draw attention to the properties of the created singly charged photoion which is in an excited state. It is no surprise that the inner-shell vacancy will be filled by an electron from higher shell. The energy released during this process can be either transferred via electron-electron interaction to ionize another electron, so called Auger decay, or the energy can be emitted in a form of a photon, which is called fluorescence. In this chapter, we will first study the magnetic properties of the photoion produced by two-photon ionization before the subsequent relaxation. In the next chapter, we concentrate on the polarization properties of the fluorescence photon emitted during the subsequent radiative decay.

While the extraction of the total cross section from experimental results requires detailed knowledge of beam parameters, the polarization degree of photoions and fluorescence are independent of these parameters as they are given by a normalized difference of the measured ion or photon intensities. This ratio is insensitive to photon flux which will allow to measure the polarization with much higher accuracy the than total cross section, and hence, this method could serve as an alternative approach in fundamental research as well as nonlinear spectroscopy [27].

5.1 Ion density matrix and ion polarization

To describe the state of an ion following two-photon inner-shell ionization, we need to obtain the corresponding reduced density matrix. This density matrix can be obtained if we trace out the direction propagation and polarization of the photoelectron from the density matrix (2.31).

$$\left\langle \alpha_f J_f M_f \left| \hat{\rho}_{\rm ion} \right| \alpha_f J_f M_f' \right\rangle = \sum_{m_e} \int d\Omega_{\hat{\boldsymbol{p}}_e} \left\langle \alpha_f J_f M_f, \boldsymbol{p}_e m_e \left| \hat{\rho}_f \right| \alpha_f J_f M_f', \boldsymbol{p}_e m_e \right\rangle \tag{5.1}$$

Performing the summation over photoelectron spin projections as well as integrating over the photoelectron emission direction, we obtain

$$\begin{aligned} \rho^{M_f M_f'}_{l_a j_a}(J_f) &= \left\langle \alpha_f J_f M_f \left| \hat{\rho}_{\rm ion} \right| \alpha_f J_f M_f' \right\rangle \qquad (5.2) \\ &= \frac{1}{[J_i]} \sum_{m_a} \left\langle j_a - m_a, J_i M_i \mid J_f M_f \right\rangle \left\langle j_a - m_a, J_i M_i \mid J_f M_f' \right\rangle \\ &\times \sum_{\substack{\lambda_1 \lambda_2 \\ \lambda_1' \lambda_2'}} \left\langle \boldsymbol{k} \lambda_1 \left| \hat{\rho}_\gamma \right| \boldsymbol{k} \lambda_1' \right\rangle \left\langle \boldsymbol{k} \lambda_2 \left| \hat{\rho}_\gamma \right| \boldsymbol{k} \lambda_2' \right\rangle \sum_{\kappa m_j} T^{\lambda_1 \lambda_2}_{\kappa m_j}(\kappa_a) T^{\lambda_1' \lambda_2' *}_{\kappa m_j}(\kappa_a), \end{aligned}$$

where $T^{\lambda_1 \lambda_2}_{\kappa m_j}(\kappa_a)$ are the simplified transition amplitudes introduced in Sec. 3. This density matrix fully describes the properties of the produced photoion and can be used to calculate the ion polarization or any subsequent processes.

An equivalent description of a system with angular momenta can be given in terms of statistical tensors. The definition of a statistical tensor analogous to the reduced density matrix (5.1) is

$$\bar{\rho}_{kq}(J_f) = \sum_{M_f M_f'} (-1)^{J_f - M_f'} \left\langle J_f M_f J_f - M_f' | kq \right\rangle \left\langle \alpha_f J_f M_f \left| \hat{\rho}_{\rm ion} \right| \alpha_f J_f M_f' \right\rangle . \tag{5.3}$$

The transformation can be also reversed, which follows from the unitary properties of the Clebsch-Gordan coefficients (see Appendix A). One of the advantages of the statistical tensors, is that they can be transformed similar to the spherical harmonics of rank k under a rotation of the coordinates [98, 149, 150]. In our case, statistical tensors make it easier to define the terminology to describe the magnetic state of an ion. For example, if a system is described by the only one nonzero statistical tensor $\rho_{00}(J)$, we say the system is in an *unpolarized* state. If at least one nontrivial ($k > 0$) statistical tensor of the system is nonzero, the system is called *polarized*. A polarized system characterized by statistical tensors of even rank is called *aligned*. Finally, if at least one odd rank statistical tensor is nonzero, the system is called *oriented*. This terminology is consistently used throughout the thesis.

The density matrices as well as the statistical tensors depend on their normalization. In order to avoid this dependency, we define the reduced statistical tensor $\mathcal{A}_{kq}$

$$\mathcal{A}_{kq}(J_f) = \frac{\bar{\rho}_{kq}(J_f)}{\bar{\rho}_{00}(J_f)}. \tag{5.4}$$

The reduced statistical tensor can be conveniently used to quantify the ion properties. In particular, the reduced statistical tensor $\mathcal{A}_{k0}(J_f)$ reflects the magnetic population of the produced ion. It can be expressed from the above definition as the statistically weighted sum of the diagonal elements of the ion density matrix

$$\mathcal{A}_{k0}(J_f) = \frac{1}{\sigma(\omega)} \sum_{M_f} (-1)^{J_f - M_f} \langle J_f M_f, J_f - M_f \mid k0 \rangle \langle \alpha_f J_f M_f | \hat{\rho}_f | \alpha_f J_f M_f \rangle . \tag{5.5}$$

In the upcoming subsection, we will consider photoions with vacancies in electron shells with s and p symmetries. Moreover, we will consider that these ions were produced by two-photon ionization of closed shell atoms only. Our consideration will lead to the reduced statistical tensors with first and second order ranks. The reduced statistical tensors with a nonzero odd rank $\mathcal{A}_{10}(J_f)$, we will refer to as orientation parameter (or orientation) and those with even rank $\mathcal{A}_{20}(J_f)$ alignment parameter (or simply alignment), in accordance to the above definition.

5.2 Polarization of singly charged ions

5.2.1 With an *s* vacancy

After acquired understanding of the total cross sections or photoelectron angular distributions of two-photon ionization of atomic s electrons in previous chapters, we investigate the physical properties of the produced photoion. To be specific, we study the magnetic population or polarization state of the photoion. We have already introduced the necessary general machinery. We first obtain the corresponding ion density matrix from the Eq. (5.2), choose $j_a = 1/2$ and $l_a = 0$ for the initial atomic state and apply the electric dipole approximation. We remind the reader that we consider ionization of a closed shell atom ($J_i = 0$) to begin with by fully polarized ($P_l^2 + P_c^2 = 1$) light. Bearing these assumptions in mind, the photoion density matrix is written as

$$\begin{aligned} \rho_{s_{1/2}}^{M_f M_f}(1/2) &= \frac{1}{400\pi^2}\Big[25(1-P_c^2)|U_{s_{1/2}}|^2 + (2 - 6M_f P_c + P_c^2)|U_{d_{3/2}}|^2 \\ &+ 54(2 + 4M_f P_c + P_c^2)|U_{d_{5/2}}|^2\Big] \\ \rho_{s_{1/2}}^{M_f M'_f}(1/2) &= 0 \qquad\qquad \text{for all } M_f \neq M'_f. \end{aligned} \tag{5.6}$$

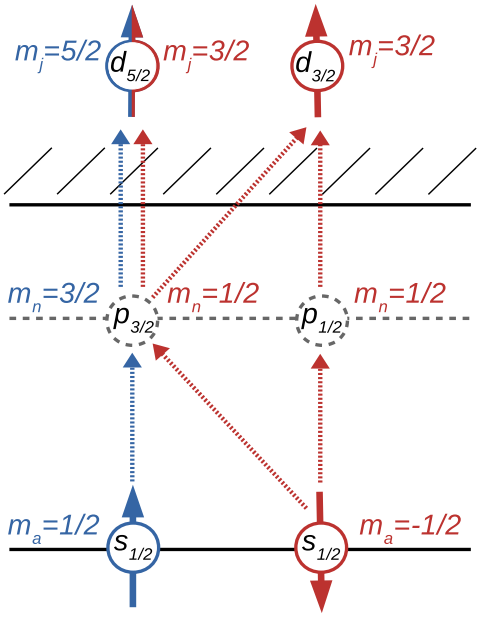

Figure 21: Possible electric dipole ionization channels in nonsequential two-photon ionization of an $s_{1/2}$ state by two right-circularly polarized photons. While both spin projections of the initial state can be promoted to a final $d_{5/2}$ partial wave, selection rules dictate that only spin-down electron can be ionized into a partial wave with $d_{3/2}$ symmetry. Note that due to the light polarization not all ionization channels are allowed, see Fig. 3.

Using this density matrix as well as the definition of the reduced statistical tensor (5.5) we can obtain the ion orientation parameter for the ion produced by two-photon ionization of an s electron

$$\mathcal{A}_{10}(1/2) \;=\; \frac{3P_c(36|U_{d_{5/2}}|^2 - |U_{d_{3/2}}|^2)}{25(1-P_c^2)|U_{s_{1/2}}|^2 + (2+P_c^2)(|U_{d_{3/2}}|^2 + 54|U_{d_{5/2}}|^2)}, \tag{5.7}$$

where the transition amplitudes U_{l_j} leading to a final photoelectron partial wave l_j were defined in chapter 2. The above expression already reveals some of the fundamental properties of the produced photoion. For example, the nominator of Eq. (5.7) is linearly dependent on the degree of circular polarization. This means that unpolarized or linearly polarized incident light cannot produce a polarized atom by means of two-photon ionization of one of its s electrons. On the other hand, from the denominator, we can clearly conclude that for incident pure circular polarized photons, the photoionization channel with a final s symmetry does not contribute to the process. This fact can be understood from the conservation of angular momentum, which has been already discussed in chapter 3.

In accordance with previous section, we should now reduce the above expressions to the nonrelativistic limit. However, it is worth noting that in nonrelativistic limit, the density matrix of the produced ion is described by a single term. For the considered system, we therefore cannot construct a nonrelativistic reduced statistical tensor with a nonzero rank. For this reason, we will restrain ourselves from the nonrelativistic description and proceed to an example which will demonstrate the limits of electric dipole approximation in calculations of the ion orientation.

To achieve photoion orientation by two-photon ionization of s electrons of closed shell atoms, it only makes sense to consider ionization by circularly polarized photons. In order to fully appreciate the upcoming example and to understanding the values as well as behavior of ion orientation, it is worth to spend a moment to think about the electron dynamics and possible ionization channels. Within the electric dipole

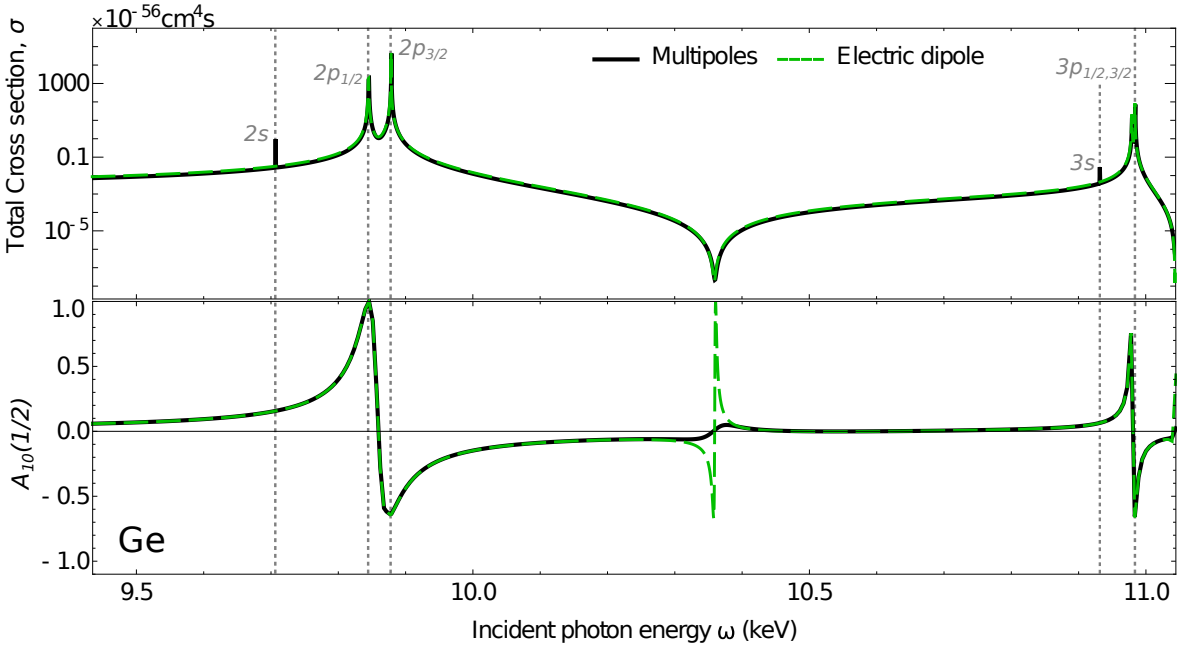

Figure 22: Direct two-photon ionization of germanium atom by two right-circularly polarized photons within electric dipole approximation (dot-dashed green), and with inclusion of higher multipole orders (full, black). Top: The total photoionization cross section as function of incident photon energy. The nonlinear Cooper minimum is expressed into the cross section in a form of a local minimum at around $\omega = 10.35$ keV. Bottom: Orientation $A_{10}(1/2)$ of the produced photoion. Although a good agreement between electric dipole and multipole calculation is achieved in the calculations of the total cross section, clear breakdown of the dipole approximation can be seen in the ion orientation at nonlinear Cooper minimum.

approximation, there are only few allowed ionization channels which the active electron can undertake (see Fig. 21). While both spin-up and spin-down electrons can be ionized from the K shell via the intermediate state with $p_{3/2}$ symmetry into a final $d_{5/2}$ partial wave, only spin-down electron can be ionized via the $p_{1/2}$ or $p_{3/2}$ intermediate states to the $d_{3/2}$ partial wave. Therefore, under circumstances where the channel with final $d_{3/2}$ symmetry strongly dominates the process, only the spin-down electron will be ionized and the produced ion will be strongly oriented. This generally happens if the incident beam energy matches either an intermediate $p_{1/2}$ level resonance, or if it is tuned to nonlinear Cooper minimum. Nonlinear Cooper minimum describes a photon energy where one of the ionization channels vanishes due to balance of positive ($E_{1s} + \omega > E_{n_n j_n}$) and negative ($E_{1s} + \omega < E_{n_n j_n}$) denominators of the virtual intermediate states of Eqn. (2.22), see section 2.2.2 for comprehensive explanation. Due to the cancellation, the channel involving the final $d_{5/2}$ partial wave vanishes and only the spin-down electron will be ionized. Therefore, based on the prediction of the electric dipole approximation, the ion orientation parameter at nonlinear Cooper minimum (as well as at intermediate $p_{1/2}$ resonances) should be equal to unity. However, in the examples below, we show that numerical calculation carried out beyond the dipole approximation reveals breakdown of this prediction in the case of two-photon ionization of K shell electrons of neutral germanium atom.

Let us present an example to demonstrate the properties of ion polarization and to demonstrate the limits of the orientation parameter (5.7) which was obtained within electric dipole approximation. In this example, we consider ionization of the K shell electron of neutral germanium ($E_{1s} = 11.1$ keV) by two right-circularly polarized photons and investigate the magnetic state of the produced photoion. The germanium atom has been chosen since, it has been already used as a target for two-photon

ionization with linearly polarized beam [24] at the SACLA free-electron laser. The experimentally determined total ionization cross section for $\omega = 5.6$ keV is $\sigma_{\text{exp}} \approx 0.64 \times 10^{-59}\text{cm}^4\text{s}$. The uncertainty associated with the experimental value is not mentioned, however, we can assume that it is not better than 50% (typical for cross section data). It is, therefore, in a reasonable agreement with our theoretical result $\sigma_{\text{theo}} \approx 2 \times 10^{-59}\text{cm}^4\text{s}$ [64], suggesting that our calculation methods are suitable for this scenario. We consider single photon energies in the range of $9.5 - 11$ keV, which covers photon energies matching the $1s \to 2p$ and $1s \to 3p$ intermediate resonances, as well as a nonlinear Cooper minimum between the resonances. The corresponding results are presented in Fig. 22. To guide the eye, the upper plot shows the total cross section as a function of the incident photon energy, calculated within (dashed, green) and beyond (full, black) electric dipole approximation. The lower plot shows the orientation of the produced photoion. The same color notation as in the upper plot was used. The level resonances in the upper plot can be understood by the sequential ionization process during which the electron from a given shell is ionized by one photon, and simultaneously, the $1s$ electron is excited into the hole by the second photon. The logarithmic scale used in the figure also reveals the nonlinear Cooper minimum in the total cross section in a form of a local minimum, which lies around $\omega = 10.35$ keV (see Sec. 2.2.2 for the explanation of nonlinear Cooper minimum). From Fig. 22 it becomes apparent that position of the nonlinear Cooper minimum could be determined from measurements of the total cross section. The total cross section, however, cannot reveal the breakdown of the electric dipole approximation. From the plot of the total cross section, we can see that apart from dipole forbidden transitions at the $1s \to 2s$ and $1s \to 3s$ resonances, the calculations within the electric dipole approximation are in an excellent agreement with the multipole calculations. Hence, it would be very challenging to access information about the multipole transitions from measurements of the total cross section, instead, other observables need to be inspected.

The ion orientation depicted in the lower plot of Fig. 22, reveals hitherto elusive information. While the ion orientation for photon energies matching an intermediate $p_{1/2,3/2}$ level (sequential ionization) resonances agrees between electric dipole and multipole calculations, a breakdown of the dipole approximation is clearly visible at the nonlinear Cooper minimum. The high degree of ion orientation at this point drops strongly due to the contributions of the generally weak multipole ionization channels. This breakdown of the electric dipole approximation can be better seen in figure 23, which shows the ion orientation only in the vicinity of the nonlinear Cooper minimum. The left subfigure shows the ion orientation within the electric dipole approximation as well as with inclusion of higher multipoles. The exact position of the Cooper minimum of each channel is marked with a dashed vertical lines. The right side of the figure shows the two electric dipole and one (of many) multipole multipole ionization channels, and demonstrates that the multipole contributions dominate the ionization process in the vicinity of nonlinear Cooper minimum. It is due to the contributions of electric quadrupole transitions that both $1s$ electrons can be ionized. Since there is no longer an asymmetry between ionization a spin-up or spin-down electron, the produced ion is no longer strongly aligned.

5.2.2 With a p vacancy

In contrast to the total as well as angle-differential cross sections, the magnetic properties of a photoion after two-photon ionization strongly depends on the angular momentum properties of the created vacancy. While it is generally difficult to polarize an atom by ionization of the s electron, it becomes significantly simpler in the case of creating a vacancy in shell with a p symmetry. To see this explicitly, we need to

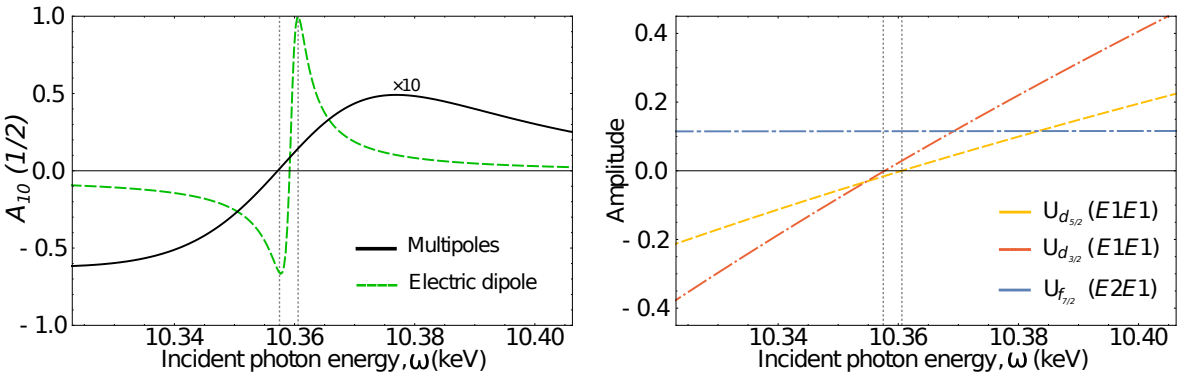

Figure 23: Left: Ion orientation following the direct two-photon ionization of germanium atom by two right-circularly polarized photons within electric dipole approximation (dot-dashed green), and with inclusion of higher multipole orders (full, black), see also Fig. 22. The incident photon energy range is restricted to the vicinity of nonlinear Cooper minimum. Right: Both electric dipole transition amplitudes as well as one of the multipole amplitudes (in atomic units) as functions of incident photon energy. The peaks in the ion orientation parameter of the electric dipole calculation on the left part of the figure can be matched with the zero values of electric dipole amplitudes.

obtain the density matrices describing the photoion after one of its p electrons has been removed by absorption of two photons. Since the full relativistic treatment would become rather lengthy, we restrict the current analytical analysis to the nonrelativistic limit. The nonrelativistic density matrix corresponding to an ion with a p vacancy produced by two photons of arbitrary photon polarization is

$$\begin{aligned}
\rho_p^{\pm1\pm1}(1) &= \frac{9}{2800\pi^2}\Big[175(1\mp P_c)|U_p^{(s)}|^2 + 70\left(1+3P_l^2\mp P_c\right)U_p^{(s)}U_p^{(d)} \\
&+ 7\left(19+6P_l^2\mp P_c-18P_c^2\right)|U_p^{(d)}|^2 + 18\left(9+P_l^2\pm 14P_c+7P_c^2\right)|U_f^{(d)}|^2\Big] \\
\rho_p^{00}(1) &= \frac{81}{2800\pi^2}\Big[7\left(1+P_l^2-P_c^2\right)|U_p^{(d)}|^2 + \left(13+3P_l^2+7P_c^2\right)|U_f^{(d)}|^2\Big] \\
\rho_p^{\pm1\mp1}(1) &= \frac{-63P_l}{2800\pi^2}(5U_p^{(s)}+U_p^{(d)})(5U_p^{(s)}+7U_p^{(d)}).
\end{aligned} \tag{5.8}$$

Out of the density matrix, we can construct the reduced statistical tensors which reflect the polarization state of the photoion. Since we started with a closed shell atom, the total angular momentum of the photoion must be equal to unity. From its density matrix, we can therefore obtain the statistical tensors of the zeroth, first and second rank. This means, that the two-photon ionization produces oriented as well as aligned ion. The orientation is obtained from the above density matrix and reads

$$\mathcal{A}_{10}(1) = \frac{9\sqrt{2}P_c\Big(36|U_f^{(d)}|^2-(5U_p^{(s)}+U_p^{(d)})^2\Big)}{400\pi^2\bar{\rho}_{00}}, \tag{5.9}$$

where $\bar{\rho}_{00}$ is the zeroth order statistical tensor given by

$$\begin{aligned}
\bar{\rho}_{00} &= \frac{3\sqrt{3}}{400\pi^2}\Big[50|U_p^{(s)}|^2 + (47+21P_l^2-45P_c^2)|U_p^{(d)}|^2 + 20U_p^{(s)}U_p^{(d)}(1+3P_l^2) \\
&+ 9(7+P_l^2+5P_c^2)|U_f^{(d)}|^2\Big].
\end{aligned} \tag{5.10}$$

As in the case of orientation of a photoion with an s vacancy studied in previous subsection, the nonzero orientation here also requires the incident photons to be circularly

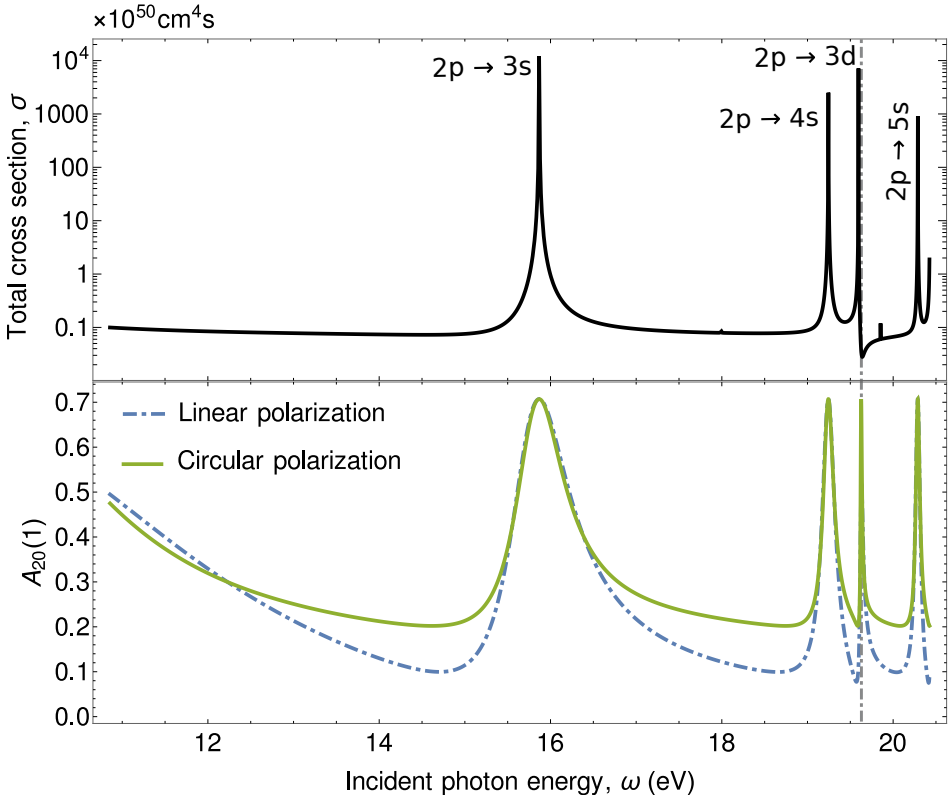

Figure 24: The total cross section of (top) and photoion alignment $\mathcal{A}_{20}(1)$ (bottom) following two-photon ionization of the $2p$ electrons of neutral neon atoms. Ionization by two incident linearly (dot-dashed blue) or right-circularly (solid green) polarized photons was considered. The nonlinear Cooper minimum is marked with a vertical gray line.

polarized. What is different in polarization of photoions with a p vacancy though, is the ion alignment given by

$$\begin{aligned}\mathcal{A}_{20}(1) &= \frac{3\sqrt{6}}{2800\pi^2\bar{\rho}_{00}}\Big[175|U_p^{(s)}|^2 + 7(10 - 3P_l^2 - 9P_c^2)|U_p^{(d)}|^2 + 70U_p^{(s)}U_p^{(d)}(1 + 3P_l^2) \\ &+ 9(5 - P_l^2 + 7P_c^2)|U_f^{(d)}|^2\Big]. \end{aligned} \tag{5.11}$$

In this case, it is no longer true that the atom can be polarized only by circularly polarized light. Quite contrary, the first term in the nominator corresponding to the $U_p^{(s)}$ ionization channel is independent of the photoion polarization, and hence, remains also for two-photon ionization by completely unpolarized light. This concept has been previously described also for one-photon ionization [151, 152].

It is time to numerically investigate polarization of ions produced by two-photon ionization of p electrons. The lower part of figure 24 presents the alignment parameter $\mathcal{A}_{20}(1)$ of a singly charged neon atom, which was produced by two-photon ionization of one of its outer shell electrons. The calculations have been performed considering the incident photon polarization to be linearly (dot-dashed blue) or circularly (solid blue) polarized. From the figure, it is clear that ion alignment depends on the incident photon polarization, however, apart from slightly different values in nonresonant regions, the overall behavior is very similar. What is more interesting, is the dynamic behavior of the alignment parameter as a function of incident photon energy. One could notice a trend of constant value of the alignment, which would take values of around $\mathcal{A}_{20}(1) \approx 0.1$, disturbed by plethora of resonances. The reason why this figure is rich on information is that there are three fundamentally different reasons for these increased values of the alignment.

Firstly, the higher degree of alignment at low photon energies originates from the changing values of transition amplitudes due to threshold effects. Similarly as in Sec. 3.2.3, the generally less dominant ionization channel (in this case $p \to s \to p$) has increased values due to the threshold effects while the otherwise stronger channels take lower values.

The second cause for an increased ion alignment following two-photon ionization of $2p$ electrons of neutral neon are the intermediate resonances. To guide the eye, we present the total cross section for the same process and same incident photon energy range (upper part of Fig. 24). By comparing these figures, it is clear that if the incident photon energy matches an intermediate resonance, the alignment increases. The reason for this is the same as in previous section and can be readily understood from Eq. (5.11). Whenever the incident photon energy matches a $2p \to ns$ resonance, this ionization channel strongly dominates over all others. Therefore, by looking at the alignment expression (5.11) and setting $U_p^{(s)} \approx 1$, $U_p^{(d)} \approx 0$ and $U_f^{(d)} \approx 0$, one immediately obtains $\mathcal{A}_{20}(1) = 1/\sqrt{2} \approx 0.7$, the maximum value seen in the plot.

The last phenomenon which cases an increased ion alignment is when the incident photon energy matches a nonlinear Cooper minimum. At this point, the dominant ionization channels drop to zero, while the $p \to s \to p$ channel remains nonzero. In this case we reach the same degree of alignment as if we tune the photon energy into resonance. The exact energy position of the nonlinear Cooper minimum is very near the $2p \to 3d$ resonance. To make the offset from the resonance more visible, the nonlinear Cooper minimum was marked with a gray vertical line.

5.3 Experimental consideration

The Stern-Gerlach experiment is one of the most famous experiments in atomic physics. In the experiment, it was demonstrated that particles posses intrinsic angular momentum, called spin, that is closely analogous to the angular momentum of a classically spinning object. Moreover, it was also shown that the spin angular momentum is quantized and only one component of the spin can be measured at a time. In the original experiment, silver atoms were sent through a spatially varying magnetic field, which deflected them before they were recorded by a detector. The two possible spin projections of the $5s$ electron of silver atoms created two discrete points of accumulation on the detector screen, rather than a continuous distribution, which proves the quantization of spin.

We can now return to two-photon ionization of an atomic s electron, and consider that the produced photoion is passed through a spatially varying magnetic field. Such Stern-Gerlach analyser [153] can determine the polarization of the photoions. If we consider the detector scheme as in the original experiment, polarization of a photon with an s vacancy would mean, that the intensity of one of the two accumulated points on the detector screen would dominate over the other. We will keep this detection scheme in mind and use it to suggest an experiment which could resolve the long standing disagreement between theory in experiment in a two-photon ionization experiment.

Let us now consider the Stern-Gerlach detection technique in order to study a similar scenario as in the experiments by Doumy *et al.* [38], who reported the total cross section of two-photon ionization of Ne^{8+}. The experimentally determined cross section was orders of magnitude greater than theoretically predicted values [64, 118, 119]. We here suggest, that carrying out a similar experiment (but with a measurement of the ion orientation) could allow to test the theoretical agreement with the experiment at higher accuracy, and thus, elucidate the reason of the discrepancy. Figure 25 shows the total cross section as well as the ion orientation of ionization of Ne^{8+} by two right-circularly polarized photons. As seen from this figure, a nonlinear Cooper minimum

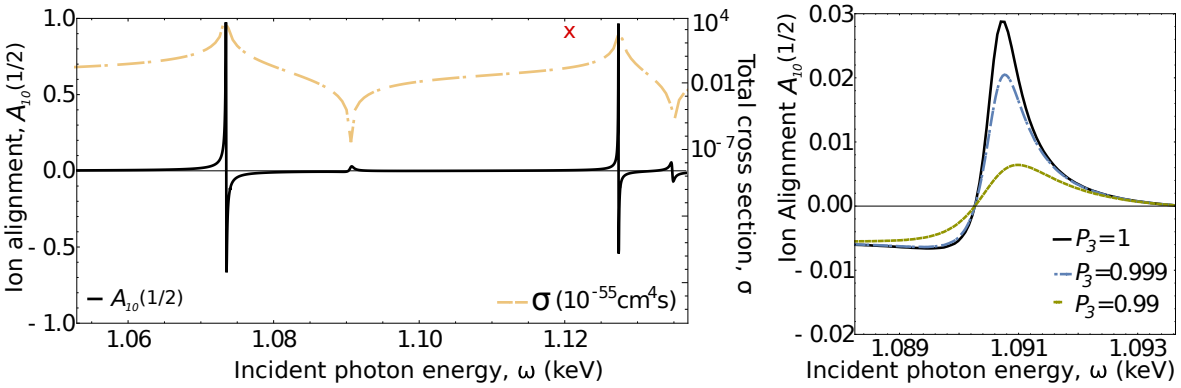

Figure 25: Ion orientation after nonsequential two-photon ionization of Ne^{8+} by two right-circularly polarized photons. Left: the total cross section as well as the orientation parameter $\mathcal{A}_{10}(1/2)$ as a function of incident beam energy. The experimentally determined cross section [38] is marked with a red cross. Right: Sensitivity of the ion orientation to the purity of polarization of the incident photons is shown in detail.

appears for incident photon energy about 20 eV lower than the one used in Ref. [38]. It can also be seen, that the experimentally measured value lies near an intermediate resonance. The width of the ionizing light could overlap with this resonance, which could lead to an increased cross section as reported in the experiment [118, 119]. Measuring the ion polarization at the nonlinear Cooper minimum would avoid this issue, and moreover, comparing the measurements performed using left- and right- photon polarization direction could lead to elimination of further uncertainties and hence, lead to a more precise comparison.

In previous section, it was shown that it is necessary to include higher multipole order of light-matter interaction in order to calculate ion orientation at Cooper minimum. Instead of reviewing the breakdown of the electric dipole approximation, in this example, we demonstrate the sensitivity of the ion orientation to the polarization purity of the incident beam. To get a better feeling about the properties of this observable, let us provide the expression for orientation parameter after two-photon ionization of a $1s$ of a closed-shell atom in the electric dipole ($J_1 = J_2 = 1$ and $p_1 = p_2 = 1$) approximation similar to Eq.(5.7). To describe our considered study case, we choose the incident beam to be circularly polarized, however, not necessary purely. The lack of purity of the degree of circular polarization of the incident light can be described analytically by introducing $\delta P_c = 1 - (P_c)^2$. Hence, for two-photon ionization of the helium-like neon with circularly polarized light, the orientation of the photoion becomes

$$\mathcal{A}_{10}(1/2) \;=\; \frac{6P_c\Big[36(U_{d_{5/2}})^2 - (U_{d_{3/2}})^2\Big]}{6\Big[(U_{d_{3/2}})^2 + 54(U_{d_{5/2}})^2\Big] + 5\delta P_c \delta U^2}, \tag{5.12}$$

where the transition amplitudes U_{l_j} correspond to definitions in chapter 3 and $\delta U^2 = \Big[10(U^{(1/2)}_{s_{1/2}})^2 + 10U^{(1/2)}_{s_{1/2}}U^{(3/2)}_{s_{1/2}} + (5U^{(3/2)}_{s_{1/2}})^2 - 10(U^{(1/2)}_{d_{3/2}})^2 - 10U^{(1/2)}_{d_{3/2}}U^{(3/2)}_{d_{3/2}} + 2(U^{(3/2)}_{d_{3/2}})^2 - 27(U^{(3/2)}_{d_{5/2}})^2\Big]$ with the $(E1E1)$ notation dropped for practical reasons. It can easily be seen that for the case $P_c = \pm 1$ this expression coincides with Eq. (5.7). Moreover, the expression above also demonstrates the strong sensitivity of the ion orientation. With the increasing polarization purity de-tuning (i.e. increasing δP_c), the denominator increases and the orientation parameter decreases. This behavior can be graphically seen on the right side of Fig. 25, where it is shown that de-tuning the purity of incident polarization by mere 0.1% results in a drop of the ion orientation at nonlinear Cooper

minimum by around 30%. If the incident beam is only 99% circularly polarized, the ion polarization decreases to about 20% of the value of pure polarized beam. This high sensitivity of the ion orientation appears uniquely at the nonlinear Cooper minimum, as the influence of other channels increases quickly with polarization de-tuning. At photon energies matching an intermediate level resonances, the process is effectively determined by one of the channels only, hence, all other channels are negligible. Due to this fact, the ion orientation is no longer extremely sensitive to the de-tuning the polarization purity of the incident light. The purity of ion orientation at these resonant photon energies could be, however, influenced by the level widths of the fine-structure levels.

The study of two-photon ionization of the $1s$ electron of helium-like neon of Fig. 25 was inspired by already performed experiment [38]. In contrast to the experiment, we suggest performing the experiments with circularly polarized beams, which are already available at Linac Coherent Light Source (LCLS) at Standford [154] as well as FERMI at Trieste [155]. Moreover, number of other free-electron facilities include polarization control in their upgrade plans[156, 157]. With these experimental possibilities, the nonlinear Cooper minimum can play a key role in detailed understanding of nonlinear light-matter interaction. Moreover, the degree of ion orientation (or degree of circular polarization of fluorescent light) has been found to be extremely sensitive to the polarization purity of ionizing light and hence could be used for measuring the polarization purity of free-electron laser beams.

6 Analysis of Subsequent Fluorescent Light

In the previous chapter, we discussed the magnetic state of an ion following two-photon ionization. In the case of inner-shell ionization, where the created hole is surrounded by electrons in higher orbitals, the excited ion relaxes to a lower energy state after some time. The relaxation can proceed via nonradiative channel where the excess energy is transferred to another electron or by an emission of a photon. Since the existence of the excited ion is limited by its lifetime, it is often experimentally more convenient to detect the photoion state indirectly via detecting the subsequently emitted particles. In this chapter, we will extend the study of two-photon inner-shell ionization one step further and describe the subsequent emission of a photon. This means, we will consider the same process as before, use the density matrix describing the the state of the photoion (5.1) from the previous chapter, and use it to describe the subsequent radiative decay. Starting from the first step, where our system comprises of an atom and two photons, the two-step process we can schematically represent the process as

$$|\alpha_i J_i M_i\rangle + 2\gamma(\omega) \rightarrow |\alpha_f J_f M_f\rangle + |\boldsymbol{p}_e m_e\rangle \rightarrow |\alpha_0 J_0 M_0\rangle + |\boldsymbol{p}_e m_e\rangle + \gamma_0(\omega_0), \qquad (6.1)$$

which differs from (2.9) only by the subsequent step, the relaxation of the excited photoion from a state $|\alpha_f J_f M_f\rangle$ into a lower energy state $|\alpha_0 J_0 M_0\rangle$ with simultaneous emission of a fluorescence photon $\gamma_0(\omega_0)$. To obtain the fluorescence photon properties we need to obtain the density matrix of the system after this additional relaxation step. Detection of fluorescence yields are often employed in measurements of two-photon K shell ionization of solids, where the $K\alpha$ fluorescence serve as a direct signature of the K shell hole creation. While electron spectroscopy would also be a possible detection technique, re-scattering of the photoelectrons in the solid could lead to experimental difficulties. In this sense, detection of the fluorescence is a more suitable method, and therefore, requires theoretical attention.

6.1 Density matrix of fluorescent photons

The density matrix fully describing the properties of the fluorescence photons can be obtained using the same tools as in chapter 2 by propagating the produced photoion density matrix through an additional step of radiative decay. Following the general rules, we obtain the photon density matrix of the fluorescence photon [98, 100]

$$\begin{aligned}\langle \boldsymbol{k}_0\lambda_0 |\hat{\rho}_{\gamma_0}| \boldsymbol{k}_0\lambda_0'\rangle &= \sum_{M_f M_f' M_0} \langle \alpha_f J_f M_f |\hat{\rho}_f| \alpha_f J_f M_f'\rangle \left\langle \alpha_0 J_0 M_0 \left|\hat{\mathcal{R}}(\boldsymbol{k}_0,\lambda_0)\right| \alpha_f J_f M_f \right\rangle \\ &\times \left\langle \alpha_0 J_0 M_0 \left|\hat{\mathcal{R}}(\boldsymbol{k}_0,\lambda_0')\right| \alpha_f J_f M_f' \right\rangle^* . \qquad (6.2)\end{aligned}$$

The $\left\langle \alpha_0 J_0 M_0 \left|\hat{\mathcal{R}}(\boldsymbol{k}_0,\lambda_0)\right| \alpha_f J_f M_f \right\rangle$ is the transition matrix for the specific bound-bound radiative transition. This transition amplitude is similar to the second-order amplitude (2.10) but with the difference, that only one photon transition takes place and both initial and final wave functions describe an electronic bound state. Since the polarization degree of the fluorescence photon are given by a ration of its density matrix elements, the polarization is independent of the bound-bound transition amplitudes. Just as in the case of Eq. (2.10), we can simplify this transition amplitude with the

use of the photon field of Eq. (2.16) and the Wigner-Eckart theorem (A.1). We obtain

$$\begin{aligned}\langle \boldsymbol{k}_0\lambda_0 \,|\hat{\rho}_{\gamma_0}|\, \boldsymbol{k}_0\lambda_0'\rangle &= 2\pi \sum_{\substack{JMp\\J'M'p'}} \sum_{\substack{M_fM_f'\\M_0}} \lambda_0^p \lambda_0'^{p'} i^{J-p+J'-p'} D^J_{M\lambda_0}(\theta,\phi) D^{J'*}_{M'\lambda_0'}(\theta,\phi)[J_0][J,J']^{1/2} \\ &\times \langle J_fM_f, JM \mid J_0M_0\rangle \left\langle J_fM_f', J'M' \mid J_0M_0\right\rangle \left\langle \alpha_f J_f M_f \,|\hat{\rho}_f|\, \alpha_f J_f M_f'\right\rangle \\ &\times \left\langle \alpha_0 J_0 || \boldsymbol{\alpha}\cdot \boldsymbol{a}^{(p)}_J || \alpha_f J_f\right\rangle \left\langle \alpha_0 J_0 || \boldsymbol{\alpha}\cdot \boldsymbol{a}^{(p')}_{J'} || \alpha_f J_f\right\rangle^*, \end{aligned} \tag{6.3}$$

where the polar and azimuthal angles θ and ϕ define the fluorescence photon emission direction with respect to the $\hat{\boldsymbol{z}}$ axis. The quantization axis was chosen to be along the incoming photon direction $\hat{\boldsymbol{k}}$, see Fig. 2. This equation represents the most general form of the photon density matrix for the radiative transition between the many-electron state $|\alpha_f J_f\rangle$ and $|\alpha_0 J_0\rangle$. It depends on the electronic structure of the photoion as described by the decay transition amplitudes as well as the magnetic population of the excited ionic state described by its density matrix. Although it has the capacity to describe all possible decay transitions, in the subsection below, we always choose only one specific transition to demonstrate the physical properties of the fluorescence photon.

6.2 Degree of polarization of fluorescence light

The polarization of photons is conveniently expressed in terms of Stokes parameters introduced in Sec. 2.3.2. Theoretically, the three Stokes parameters describing the photon polarization can be obtained by a combination of elements of the density matrix (6.3). Their exact expression can be easily derived from the expression (2.25) by normalized addition (subtraction) of its terms

$$\begin{aligned} P_1^{(J_0)}(\boldsymbol{k}_0) &= \frac{\langle \boldsymbol{k}_0\lambda_0 = 1 \,|\hat{\rho}_{\gamma_0}|\, \boldsymbol{k}_0\lambda_0' = -1\rangle + \langle \boldsymbol{k}_0\lambda_0 = -1 \,|\hat{\rho}_{\gamma_0}|\, \boldsymbol{k}_0\lambda_0' = 1\rangle}{\langle \boldsymbol{k}_0\lambda_0 = 1 \,|\hat{\rho}_{\gamma_0}|\, \boldsymbol{k}_0\lambda_0' = 1\rangle + \langle \boldsymbol{k}_0\lambda_0 = -1 \,|\hat{\rho}_{\gamma_0}|\, \boldsymbol{k}_0\lambda_0' = -1\rangle} \\ P_2^{(J_0)}(\boldsymbol{k}_0) &= i\frac{\langle \boldsymbol{k}_0\lambda_0 = -1 \,|\hat{\rho}_{\gamma_0}|\, \boldsymbol{k}_0\lambda_0' = 1\rangle - \langle \boldsymbol{k}_0\lambda_0 = 1 \,|\hat{\rho}_{\gamma_0}|\, \boldsymbol{k}_0\lambda_0' = -1\rangle}{\langle \boldsymbol{k}_0\lambda_0 = 1 \,|\hat{\rho}_{\gamma_0}|\, \boldsymbol{k}_0\lambda_0' = 1\rangle + \langle \boldsymbol{k}_0\lambda_0 = -1 \,|\hat{\rho}_{\gamma_0}|\, \boldsymbol{k}_0\lambda_0' = -1\rangle} \\ P_3^{(J_0)}(\boldsymbol{k}_0) &= \frac{\langle \boldsymbol{k}_0\lambda_0 = 1 \,|\hat{\rho}_{\gamma_0}|\, \boldsymbol{k}_0\lambda_0' = 1\rangle - \langle \boldsymbol{k}_0\lambda_0 = -1 \,|\hat{\rho}_{\gamma_0}|\, \boldsymbol{k}_0\lambda_0' = -1\rangle}{\langle \boldsymbol{k}_0\lambda_0 = 1 \,|\hat{\rho}_{\gamma_0}|\, \boldsymbol{k}_0\lambda_0' = 1\rangle + \langle \boldsymbol{k}_0\lambda_0 = -1 \,|\hat{\rho}_{\gamma_0}|\, \boldsymbol{k}_0\lambda_0' = -1\rangle}, \end{aligned} \tag{6.4}$$

where the superscript (J_0) represents the total angular momentum of the ion after the radiative decay. In this chapter, we aim to describe the polarization degree of fluorescence photons. Since their energy is determined by the corresponding bound-bound transition, we will simplify the notation by leaving out the momentum $\boldsymbol{k}_0$ and using only the angles which determine the photon emission direction in the notation of Stokes parameters, e.g. $P_1^{(J_0)}(\theta,\phi)$. Having explained the basic quantities and their notation, we can now dive into investigation of the fluorescence polarization properties of specific examples. As in all previous chapters, we begin with considering two-photon ionization of s electrons and study the properties of the subsequent $K\alpha$ decay. We remind the reader that in Sec. 2.3.2, we introduced a notation to distinguish between the degree of polarization of the incident and the fluorescence photons. While the two photons that ionize the target are described by Stokes parameters P_l and P_c, the polarization of the photons emitted by the produced ion is described by P_1, P_2 and P_3 parameters.

6.2.1 $K\alpha$ fluorescence

The $K\alpha$ fluorescence is emitted by the decay of a $2p$ electron to a $1s$ vacancy. As such, the detection of the characteristic fluorescence photon is a direct evidence of a

K shell vacancy. This signal is often used in experiments [24–27] to quantify the total two-photon K shell ionization cross section. The fluorescence photon density matrix can be obtained from the above general expression. For convenience, we here introduce a shorter notation $\rho^{\pm1\pm1}_{\gamma_f}(J_0) = \langle \boldsymbol{k}_0\lambda_0 = \pm1 \,|\hat{\rho}_{\gamma_0}|\, \boldsymbol{k}_0\lambda_0' = \pm1\rangle$ to express the fluorescence photon density matrix. Consistently with relativistic theory in previous chapters, we assume that the excited ion was produced by two-photon ionization of a full shell atom by fully polarized photons. Let us first consider the case, where the $1s$ vacancy is filled by an electron from the $2p_{1/2}$ shell. Under these conditions, the photon density matrix of the $K\alpha_2$ fluorescence is given by

$$\begin{aligned}
\rho^{\pm1\pm1}_{\gamma_f}(1/2) &= \frac{3|T_{n'pns}|^2}{400\pi}\Big[50(1-P_c^2)|U_{s_{1/2}}|^2 + 2(2+P_c^2)(|U_{d_{3/2}}|^2 + 54|U_{d_{5/2}}|^2) \\
&\mp 3P_c\cos\theta(36|U_{d_{5/2}}|^2 - |U_{d_{3/2}}|^2)\Big] \qquad (6.5)\\
\rho^{\pm1\mp1}_{\gamma_f}(1/2) &= 0,
\end{aligned}$$

where $T_{n'pns}$ is reduced amplitude describing the bound-bound decay transition. Although we discuss the $K\alpha_2$ emission only, the above expression is valid for any other transition with the same symmetry, i.e. for any transition $np_{1/2} \to n's_{1/2}$. The photon density matrix for the $K\alpha_1$ fluorescence photon which describes the photon emitted by the $p_{3/2} \to s_{1/2}$ transition, $\rho^{\pm1\pm1}_{\gamma_f}(3/2)$, is the same as $\rho^{\pm1\pm1}_{\gamma_f}(1/2)$ only with the $\cos\theta$ term multiplied by a factor of $-1/2$. From the above photon density matrix, we can also see that no properties of the fluorescence photon depend on the azimuthal angle ϕ and unless the incident light is circularly polarized, there is also no dependence on the θ angle.

We can now utilize the photon density matrix to obtain the degree of polarization of the fluorescence photons. Notice that since the off-diagonal elements of the photon density matrix are always zero, the fluorescence photon will never posses any degree of linear polarization. Nevertheless, it can be circularly polarized. The degree of circular polarization of the fluorescence photon can be written in the electric dipole approximation as

$$\begin{aligned}
P_3^{(1/2)}(\theta) &= \mathcal{A}_{10}(1/2)\cos\theta, \qquad (6.6)\\
P_3^{(3/2)}(\theta) &= -\frac{1}{2}\mathcal{A}_{10}(1/2)\cos\theta.
\end{aligned}$$

We already know, that the ion alignment $\mathcal{A}_{10}(1/2)$ is nonzero, only if the incident photons are circularly or elliptically polarized (see Eq. (5.7)). This property propagates also to the degree of polarization of the fluorescence photon. The simple expressions (6.6) clearly demonstrate, that the fluorescence photon is fully determined by the alignment of the ion and carries the spin polarization information. Since the $K\alpha_1$ and $K\alpha_2$ fluorescent photons have different energies, they are experimentally distinguishable [24]. This means that the degrees of circular polarization corresponding to each radiative decay can be measured and analysed separately. From the above expression, it is clear that detecting the fluorescence light emitted by the decay of the $p_{1/2}$ electron will yield stronger signal in measurements of the degree of polarization than the one emitted by the decay of the $p_{3/2}$ electron.

Due to the trivial dependence of the degree of circular polarization of $K\alpha$ radiation on the angle θ and its proportionality to the ion orientation, we will restrain from presenting an example here. Instead, we refer the reader to the corresponding results of the previous chapter and move on to investigate the $L\alpha$ characteristic lines.

6.2.2 $L\alpha$ fluorescence

We have already seen in previous chapter, that it is possible to polarize an atom by two-photon ionization of p electrons with light of arbitrary polarization. Here, we show that this feature also propagates to the polarization properties of the subsequently emitted fluorescence photon, which provides us with new tools to study atomic properties. We will now consider decay of a singly charged ion with an inner-shell p vacancy under consideration that this ion has been produced by two-photon ionization of a closed shell atom and limit the current analysis to $ns \to n'p$ bound-bound decay transitions only. As in earlier chapters, we will restrict our analytical description of two-photon ionization of p electrons to the nonrelativistic limit. The density matrix of the fluorescence photon can be simply obtain from Eq. (6.3) and (5.8). Although it is straightforward to obtain this photon density matrix, it becomes lengthy without placing any restrictions on the incident photon polarization. For the sake of simplicity, we consider that the ion was produced by two-photon ionization of right-circularly polarized light, however, in later subsection, we present an example where an unpolarized incident beam was considered. The photon density matrix for a photon emitted by $ns \to n'p$ transition is then

$$\begin{aligned} \rho_{\gamma_f}^{\pm 1 \pm 1} &= \frac{9|T_{n'snp}|^2}{2800\pi}\Big\{7(\cos\theta \pm 1)^2|U_p|^2 + 12\big[(3\cos\theta \mp 7)^2 - 10\big]|U_f|^2\Big\}, \qquad (6.7) \\ \rho_{\gamma_f}^{-11} &= \rho_{\gamma_f}^{1-1} = \frac{-9|T_{n'snp}|^2 \sin^2\theta}{2800\pi}(7|U_p|^2 + 108|U_f|^2), \end{aligned}$$

where θ is angle between the fluorescence emission direction and the propagation direction of the two incident photons, $T_{n'snp}$ is the reduced transition amplitude describing decay of the $n's$ electron to the np^{-1} vacancy. We can now use the density matrix to obtain the degrees of linear and circular polarization of the fluorescence photons by utilizing Eqs. (6.4)

$$\begin{aligned} P_1^{(0)}(\theta) &= \frac{-2\sin^2(\theta)\Big[7|U_p|^2 + 108|U_f|^2\Big]}{7\big[3+\cos(2\theta)\big]|U_p|^2 + 36\big[29+3\cos(2\theta)\big]|U_f|^2}, \qquad (6.8) \\ P_3^{(0)}(\theta) &= \frac{28\cos(\theta)\Big[|U_p|^2 - 36|U_f|^2\Big]}{7\big[3+\cos(2\theta)\big]|U_p|^2 + 36\big[29+3\cos(2\theta)\big]|U_f|^2}. \end{aligned}$$

These simple expressions describing the polarization of the fluorescence photon already reveal the dependence of the photon polarization on its emission angle. While the photons emitted along the incident beam polarization will be circularly polarized, at right angle they will be only linearly polarized. For any emission angle between these characteristic directions, the fluorescence photons will be elliptically polarized. The exact degrees of polarization will depend on the incident photon energy as well as the atomic structure of the target atom.

Even though it is necessary to calculate the transition amplitudes U_l explicitly, let us argue with physical arguments based on properties of Eq. (2.22) and quantum paths of each magnetic substate of the p orbital (see Fig. 26) that full polarization transfer from incident to fluorescent photon in direct two-photon ionization by circularly polarized light is achievable. The absorption of each right-circularly polarized photon increases angular momentum projection of the active electron by one, which lays restrictions on the possible ionization channels for each initial magnetic substate. While the ionization channel which describes the photoelectron with f symmetry is open to all of the bound $np-$electrons, the channels describing photoelectron with p symmetry is open

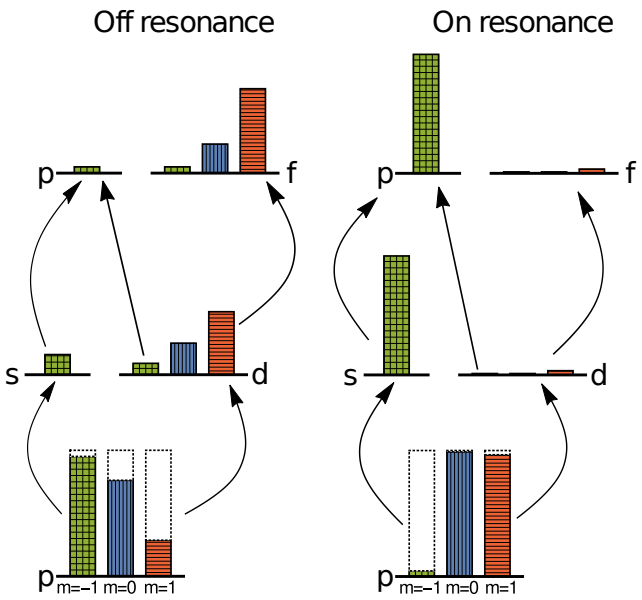

Figure 26: (Color online) Schematic diagram of possible electric dipole channels for two-photon ionization of a $p-$electron by right-circularly polarized light. The population of each magnetic projection, $m = -1$ (squared green pattern), $m = 0$ (vertical blue pattern), $m = 1$ (horizontal red pattern), after ionization is indicated with respect to the full shell population (dotted rectangle) for photon energies not matching polarization resonances (left) and matching them (right).

only to the $m = -1$ electron. This means that whenever U_p transition amplitude is greater than the U_f amplitude, ionization of the electron with negative projection will be preferred. For example, if we choose a photon energy matching a transition to an intermediate level $s-$resonance, channel with final p symmetry will dominate the process and population of negative projection electrons will be depleted (see right side of Fig. 26). The subsequent $n's \to np$ electronic transition will therefore fill the $m = -1$ vacancy and emit a photon with helicity $\lambda = -1$ along the incident beam propagation (quantization) axis. This means that the emitted radiation will be fully polarized, and specifically, the degree of circular polarization of this photon along quantization axis will be $P_3(0^\circ) \approx 1$ while at the right angle to the quantization axis $P_1(90^\circ) \approx -1$. The resonant photon energy will be clearly visible in fluorescence polarization spectrum in form of a peak (or through), to which we shall refer to as *level resonance*. Since the channel with final f symmetry is generally dominant, tuning our photon energy to an intermediate d resonance will not affect the fluorescence polarization. Another way to obtain strong polarization transfer is to tune the photon energy near the nonlinear Cooper minimum (see Sec. 2.2.2). At this point, the dominant ionization channel vanishes, and identical polarization scheme as described above is achieved. The strong polarization transfer originating from this phenomenon will be referred to as *Cooper resonance*.

We will now demonstrate the above predictions with a numerical calculation of two-photon ionization of $2p$ electron of neutral magnesium. For the particular example of two-photon ionization of the $2p$ orbital of magnesium atom, the initial state is $|\alpha_i J_i M_i\rangle = |1s^2 2s^2 2p^6 3s^2\ {}^1S_0\rangle \equiv i$. The dominant ionization channels will lead to the following two final states (ionic part only) $\left|1s^2 2s^2 2p^5 3s^2\ {}^2P_{1/2}\right\rangle \equiv f_{1/2}$ and $\left|1s^2 2s^2 2p^5 3s^2\ {}^2P_{3/2}\right\rangle \equiv f_{3/2}$, describing singly charged magnesium ion with $2p_{1/2}^{-1}$ and $2p_{3/2}^{-1}$ holes, respectively. The subsequent decay of the singly charged magnesium ion to the ground state $\left|1s^2 2s^2 2p^6 3s\ {}^2S_{1/2}\right\rangle \equiv g$ results in an emission of a fluorescence photon with energy $\omega_f = E_{f_{1/2}} - E_g = 50.153$ eV or $\omega_f = E_{f_{3/2}} - E_g = 49.915$ eV [158]. Let

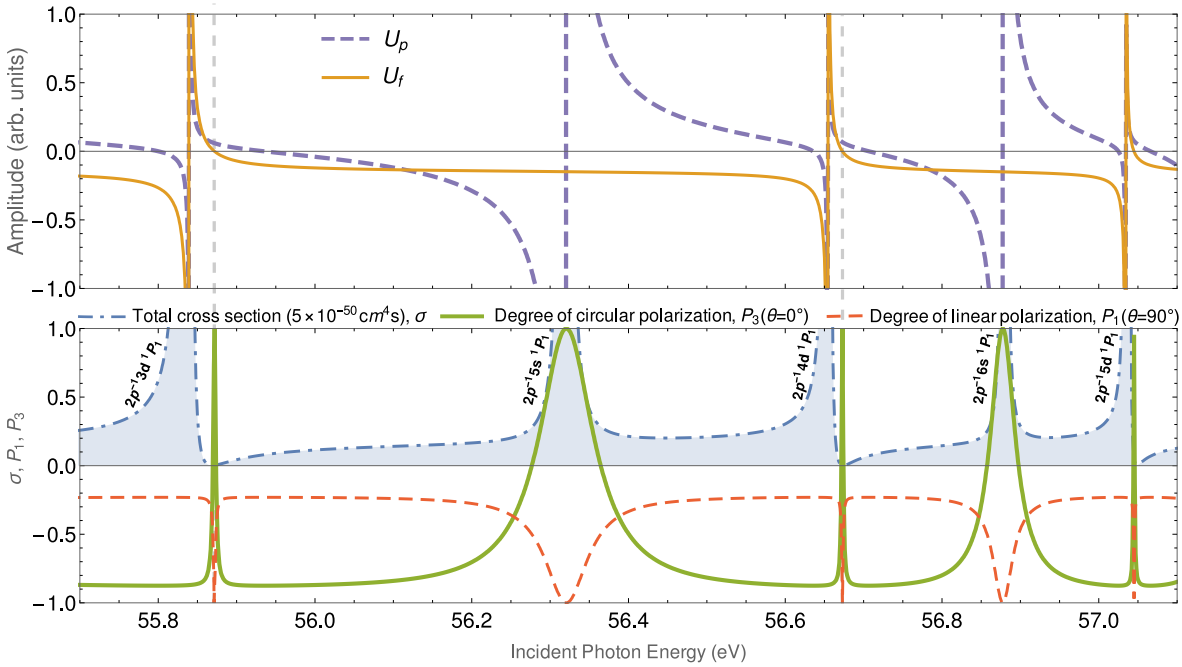

Figure 27: Two-photon ionization of the $p-$electron of magnesium atom. Transition amplitudes (top), total cross section (bottom, dot-dashed) and degree of circular and linear polarization of the emitted fluorescence photon $P_3^{(0)}(\theta = 0°)$ (bottom full) and $P_1^{(0)}(\theta = 90°)$ (bottom dashed) as functions of incident photon energy. While the electronic fluorescence resonances match the intermediate $s-$state (also visible in the total cross section).

us now consider displacement of other electrons, so called shake-up processes, which could influence the final result. Assuming that this secondary effect is more important near threshold energies, similarly as in one-photon ionization, the shake-up transition $1s^22s^22p^63s^2 + 2\gamma_i \to 1s^22s^22p^53s4s$ dominates this effect [159]. We estimated that in our example, this process contributes by less than 10%. Moreover, the subsequent fluorescent photon carries energy $E_{1s^22s^22p^53s4s} - E_{1s^22s^22p^64s} \geq 52.26$ eV [158], depending on the coupling of $2p^53s4s$ electrons. It is therefore clear, that in comparison to ≈ 50 eV produced by the dominant channels, one can filter out the photons arising from the shake-up decay channel by the photon detector [160].

Having justified our theoretical approach, let us first utilize the nonrelativistic expression (6.8) to predict the degree of polarization of the subsequent $3s \to 2p$ fluorescence. Figure 27 shows possible ionization channels (upper plot) as well as the total two-photon ionization cross section and degrees of circular and linear polarization of subsequent fluorescent photon (lower plot) as functions of incident photon energy. The lower subfigure shows, that degree of circular polarization (full green) generally takes constant value of around $P_3^{(0)}(0°) \approx -0.88$ along the quantization axis, while degree of linear polarization at perpendicular direction is $P_1^{(0)}(90°) \approx -0.23$, as predicted by Eqs. (6.8). However, these values change dramatically at clearly visible resonances. If we compare the energy positions of these polarization resonances, we notice that some of them (level resonances) appear at the same energies as the resonances of the total cross section, as expected. On the other hand, Cooper resonances have no counter part in the total cross section. Their origin is apparent if the corresponding energetic positions are compared with zero value of the U_f transition amplitude (full orange curve of Fig. 27). To guide the eye, Cooper resonances are marked with dashed vertical lines. First Cooper resonance occurs at energy $\omega = 55.87$ eV near the intermediate $2p^63s^2\ ^1S_0 \to 2p^53s^23d\ ^1P_1$ resonant transition, while second Cooper resonance can be found at $\omega = 56.68$ eV close to the intermediate $2p^63s^2\ ^1S_0 \to 2p^53s^24d\ ^1P_1$ resonance.

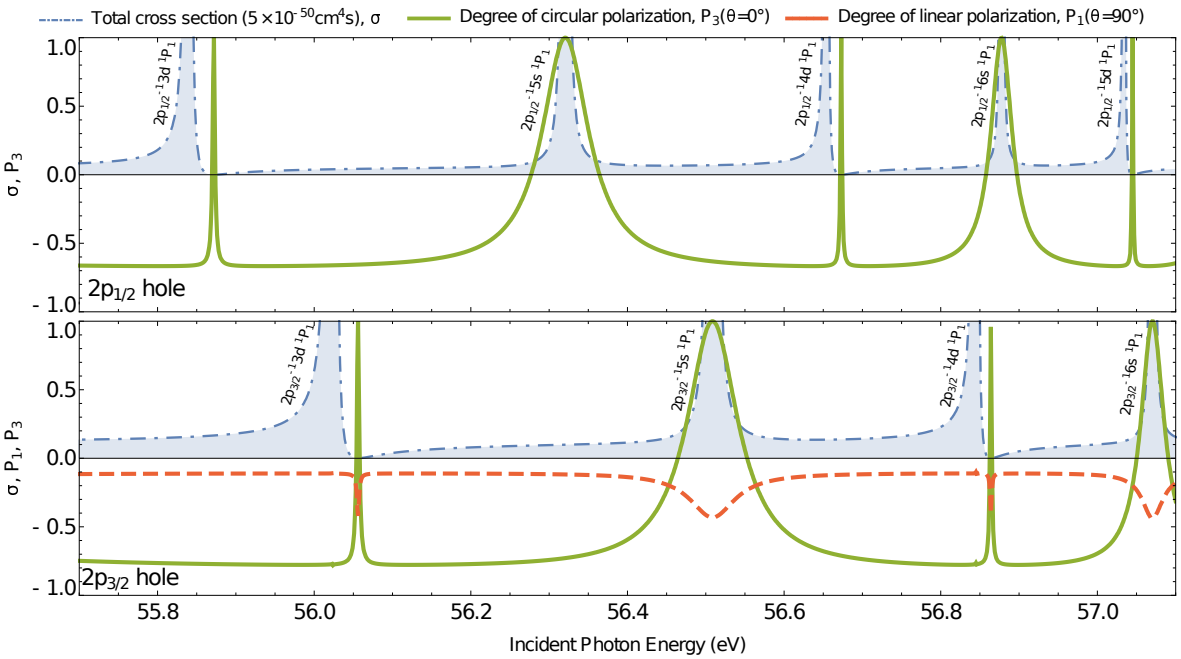

Figure 28: Two-photon ionization of the $p_{1/2}$ (upper) and $p_{3/2}$ (lower) electron of magnesium atom. Total cross section (dot-dashed) and degree of circular and linear polarization of the emitted fluorescent photon $P_3^{(0)}(\theta = 0°)$ (full) and $P_1^{(0)}(\theta = 90°)$ (dashed) as functions of incident photon energy. While the level fluorescence resonances match the intermediate $s-$state (also visible in the total cross section), the Cooper resonances originate from vanishing of the dominant ionization channels.

A natural question arises at this point. Is the nonrelativistic description sufficient in the described scenario? The fine-structure splitting of the p level is larger than the width of the Cooper minimum, it is therefore reasonable to question the nonrelativistic results. The nonrelativistic treatment was chosen for its simplicity to explain the phenomenon of polarization transfer, nevertheless, it is worth to spend a moment in order to address the validity of the presented results explicitly. For this reason, we carried out fully relativistic calculation using the general expression (6.4). The results are presented in Fig. 28, where the upper figure shows the results corresponding to two-photon ionization of the $2p_{1/2}$ ($f_{1/2}$ state) electron and the figure below to ionization of the $2p_{3/2}$ ($f_{3/2}$ state) electron. If we compare these results to the nonrelativistic ones presented in Fig. 27, we notice that by resolving the fine-structure splitting of the $2p$ electrons, we also resolve the splitting of the Cooper resonances associated with each of them. The nonlinear Cooper minima appear due to the dominant ionization channel passing through zero between two adjacent $2p^6 3s^2\ ^1S_0 \to 2p^5(P_{1/2})3s^2 nd\ ^1P_1$ or $2p^6 3s^2\ ^1S_0 \to 2p^5(P_{3/2})3s^2 nd\ ^1P_1$ resonances. From the figure, it becomes apparent that the degree of linear polarization of the fluorescent photon arises from ionization of the $p_{3/2}$ electron only, and hence the corresponding Cooper resonances are shifted to higher incident photon energies with respect to the nonrelativistic prediction. Furthermore, Fig. 28 also shows that accounting for the spin-orbit interaction changes the magnitude of the degree of linear polarization of the subsequent fluorescence photons. The larger nonrelativistic value of linear polarization degree at the Cooper resonances arises from the interference of the $f_{1/2}$ and $f_{3/2}$ terms in Eq. (2.25), which should be introduced when $E_{f_{1/2}} = E_{f_{3/2}}$. With this interference term the nonrelativistic results are restored. The important point that Fig. 28 demonstrates, is that although accounting for fine-structure splitting changes the magnitudes of the polarization degree at Cooper resonances, it firmly confirms their presence in relativistic treatment.

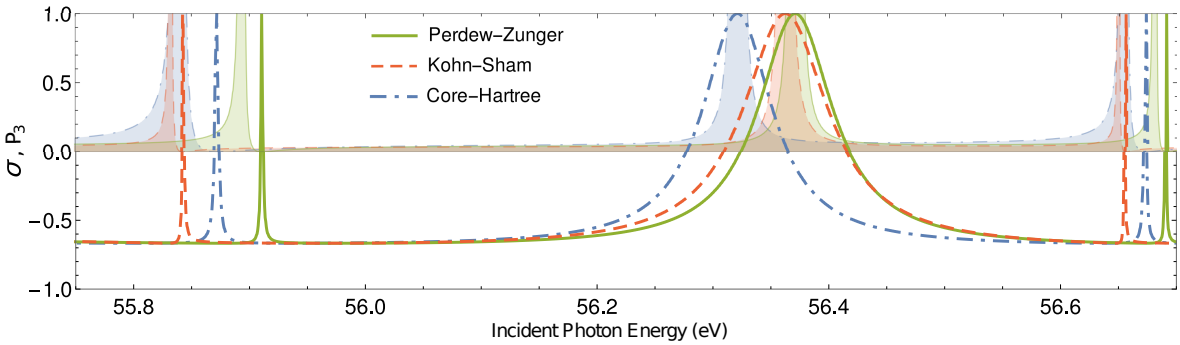

Figure 29: (Color online) Two-photon ionization of the $2p_{1/2}-$electron of magnesium atom. Total cross section (in units of 5×10^{-50} cm^{4}s shaded) and degree of circular polarization (lines) of the emitted fluorescent photon $P_3(\theta = 0^\circ)$ as functions of incident photon energy. Three different screening potentials were used to calculate the quantities: Core-Hartree (dot-dashed, blue), Perdew-Zunger (full, green), and Kohn-Sham (dashed, red).

Predictions of exact energy positions of polarization Cooper resonances strongly depend on capability of theoretical models to represent the complete atomic spectrum. However, our aim here is not to predict the position precisely, but to *justify* that the nonlinear Cooper minimum always appears between any pair of $n'(l+1)$ and $(n'+1)(l+1)$ resonances (as explained above). Although we consider our proof to be rather general, we carried out further calculations for verification. The employed single-active electron approach reproduces all the intermediate resonances $|\alpha_n J_n M_n\rangle$ as listed by NIST [158] in the given energy region. The remaining difference between single- and many-electron approaches comes from the numerical values of matrix elements. In order to investigate the sensitivity of the matrix elements on the employed theoretical model, we perform the calculations for number of different screening potentials [93–95]. Figure 29 presents the cross section (shaded) and degrees of circular polarization of fluorescence light emitted after two-photon ionization of $2p_{1/2}$ electron for three different screening potentials: Core-Hartree (dot-dashed, blue), Perdew-Zunger (full, green), and Kohn-Sham (dashed, red). From the figure, it is clear that although the exact position predictions of Cooper minima differ, the minima are predicted by all potentials. Thus, with the presented calculations we cover the essential attributes of the second-order many-electron matrix elements (2.22) and justify the existence of nonlinear Cooper minima.

6.3 Fluorescence emission direction

Now we know, how does the photon polarization change with the photon energy and what is its dependence on the photon emission direction. However, we have not yet explored, what is the most likely emission direction. It is often assumed the the atomic relaxation leads to an isotropic emission of electrons, but to what extend is this correct and does this assumption always hold? It is the aim of this section to answer these questions.

The angular distribution of the fluorescence photons can be readily obtained from the trace of the photon density matrix

$$\mathcal{W}(\theta,\phi) \;=\; \langle \boldsymbol{k}_0\lambda_0 = 1\,|\hat{\rho}_{\gamma_0}|\,\boldsymbol{k}_0\lambda_0' = 1\rangle + \langle \boldsymbol{k}_0\lambda_0 = -1\,|\hat{\rho}_{\gamma_0}|\,\boldsymbol{k}_0\lambda_0' = -1\rangle\,. \qquad (6.9)$$

From this expression together with Eq. (6.5) we can briskly come to the conclusion that the fluorescence photons emitted by a transition $np \to n's$ are equally likely to be emitted in any direction, and hence, that their angular distributions are spherically symmetric. This conclusion comes from the fact that once the two terms of Eq. (6.5)

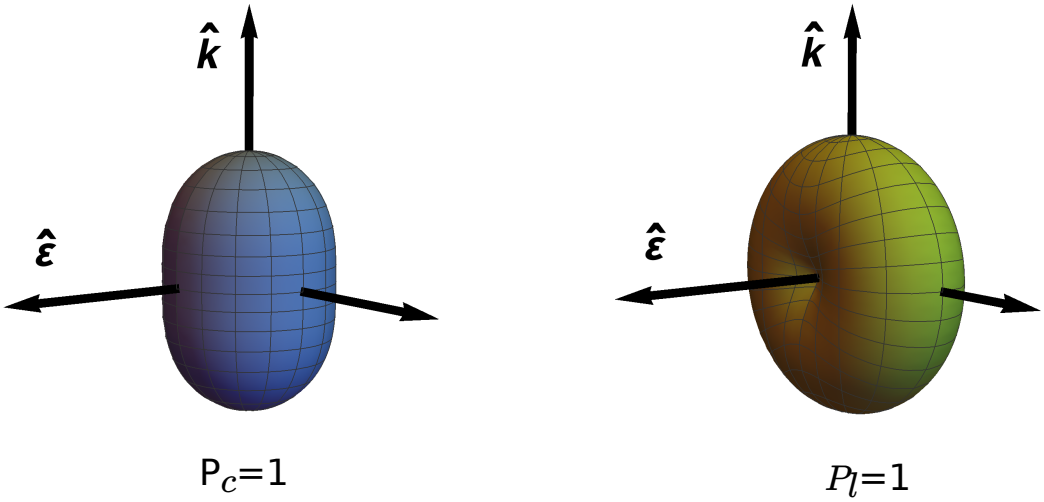

Figure 30: Typical fluorescence photon distributions for the characteristic $L\alpha$ lines emitted from a singly charged ion. The ion was produced by two-photon ionization of closed shell atom by circularly (left) or linearly (right) polarized beam.

are added, there is no angular dependence. The possible contributions arising from the higher multipole orders to this transition were found equally angle-independent. For this reason, we will concentrate on the angular distributions of the $L\alpha$ series. Even though we restricted our description of the fluorescence photon density matrix to a particular incident photon polarization, here, we return to the general case and present angular distributions of the fluorescence photons for arbitrary incident beam polarization

$$\begin{aligned}\mathcal{W}(\theta,\phi) &= \frac{9|T_{n's np}|^2}{5600\pi}\Big[P_l\cos(2\phi)\sin^4\theta\Big(7(5R_p^{(s)}+R_p^{(d)})(5R_p^{(s)}+7R_p^{(d)})+36|R_f^{(d)}|^2\Big)\\ &+ 175|R_p^{(s)}|^2(4\sin^2\theta-8)+280R_p^{(d)}R_p^{(s)}(\sin^2\theta-2)(1+3P_l^2)\\ &+ 7|R_p^{(d)}|^2\Big(8(19+18P_c^2-6P_l^2)+4\sin^2\theta(10-9P_c^2-3P_l^2)\Big)\\ &+ 18|R_f^{(d)}|^2\Big(-8(9+7P_c^2+P_l^2)+\sin^2\theta(5+7P_c^2-P_l^2)\Big)\Big]. \qquad (6.10)\end{aligned}$$

Although the above expression is rather long, by a closer investigation it provides us with a first feeling about the angular distributions of the $L\alpha$ fluorescence photons. One can notice, that all transition amplitudes multiply a certain function which depends on the zeroth, second or fourth power of $\sin^2\theta$ and therefore, change of amplitude values does not significantly change the angular dependence. Since this is the case, figure 30 presents the general angular distribution of $L\alpha$ fluorescence photons. It is also worth noting, that the only ϕ dependence lays in the first term which is linearly proportional to the degree of linear polarization of the incident light. Therefore, for two-photon ionization of inner-shell p electrons by circularly polarized light, the distributions of subsequent fluorescence must be rotationally symmetric. The angular distribution expression above also answers the question from the beginning of this section. Since the distributions depend on powers of $\sin\theta$ they are no longer spherically symmetric as it was in the case of fluorescence emitted by a $np \to n's$ transition.

6.4 Experimental possibilities

For inner-shell ionization, it is experimentally often simpler to detect particles emitted by one of the subsequent processes rather than measuring the produced photoion. In

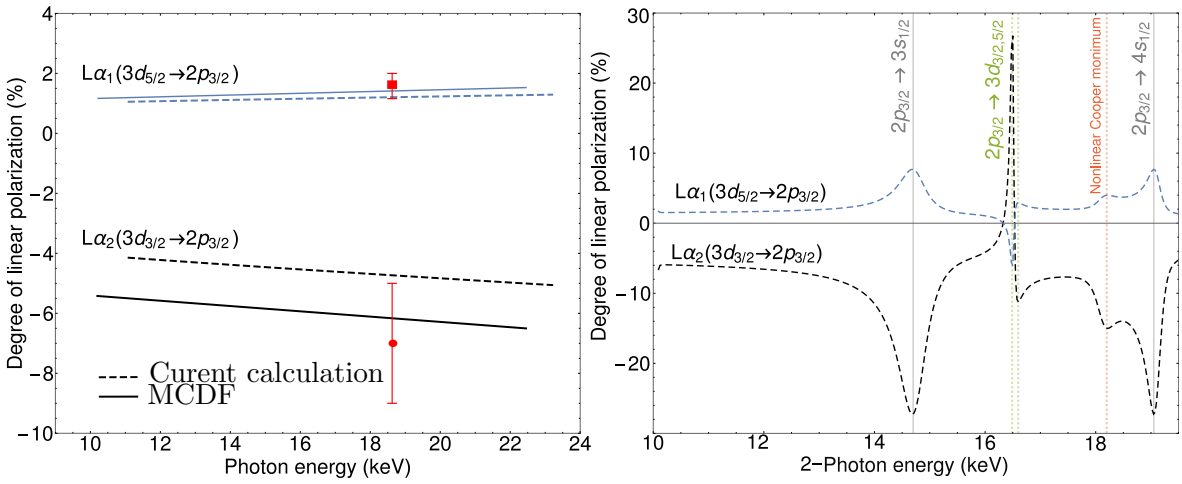

Figure 31: The linear polarization of characteristic $L\alpha$ lines emitted from singly charged neutral tungsten ion. The tungsten ion was produced by either by one- (left) or two- (right) photon ionization by unpolarized incident light. The degree of linear polarization of the fluorescence photons is presented as function of absorbed energy from one (left) or two (right) photons. For the case of one-photon ionization, results are presented for the current computation method, i.e. independent-particle approximation (dashed lines), multiconfiguration Hartree-Fock method (full lines, see [163]) as well as experimental data (red points).

the case of two-photon K shell ionization, the detection of subsequent $K\alpha$ fluorescence became a standard approach to extract the total cross sections from the measured yields $Y(\theta)$ [24–27, 161]. Currently, the total two-photon ionization cross section is the most commonly used quantity to describe the ionization process (see chapter 3 for detailed description of the total two-photon ionization cross sections). Unfortunately, there is a standing problem with the precision of the extracted cross sections. The yield of the $K\alpha$ fluorescence, which is typically measured in experiments, being integrated over angles, is a product of cross section $\sigma^{(2)}$ and a photon flux F squared [162]

$$\int Y(\theta)d\theta \propto \sigma^{(2)}F^2. \tag{6.11}$$

Thus, the precision of cross section extracted from a measured fluorescence yield are highly sensitive to uncertainties in the flux, which needs to be extracted from the fluctuating pulse energy and the pulse structure. For example, for two-photon ionization of the $K-$shell of zirconium, the total cross section was reported in the range $3.9 - 57 \times 10^{-60}\text{cm}^4\text{s}$. The reason for this wide range of values was appointed to the systematic uncertainty in beam parameters of LCLS FEL which determine the absolute flux [25]. Similarly, Richter *et al.* [37] report 30% uncertainty in the beam flux at FLASH FEL which results in $\approx 50\%$ uncertainty in the extracted cross section of two-photon ionization of singly and doubly charged neon atoms. Here we want to argue that the polarization degree of fluorescence is independent of these factors as it is given by a normalized difference of the measured fluorescent photon intensities (see Sec. 6.2). This insensitivity to photon flux will allow to measure the polarization with much higher accuracy than total cross section, and hence, this method could serve as an alternative approach in fundamental research as well as nonlinear spectroscopy [27]. Studies aimed at determining the position of nonlinear Cooper minima could in particular test the current theoretical description of atomic structure. Such studies are also experimentally realizable with the use of seeded free-electron laser operations, which are capable of producing spectrally narrow beams. At the time of writing, there have been no experiments measuring the polarization properties of fluorescence photons emitted by an ion produced by two-photon ionization. However, such experiments

have been performed for cases, where an inner-shell electron of an atom is ionized by a single photon. We here take the experiment performed by Kämpfer *et al.*, where the authors measured the linear polarization of the characteristic lines $L\alpha$, following one-photon ionization of $2p_{3/2}$ electron of neutral tungsten atoms by the primary emission of an x-ray tube [163]. We first perform the corresponding calculations within our independent-particle approximation and compare the results to the calculations performed with the multiconfiguration Dirac-Fock (MCDF) method as well as the experimental results. Then, we consider the same experimental conditions, however, this time we consider that the inner-shell hole is produced by two-photon ionization.

The left side of Fig. 31 shows the degree of linear polarization of the $L\alpha_{1,2}$ lines following the ionization of a $2p_{3/2}$ electron of tungsten by an unpolarized beam. The plot presents the comparison between theoretical results calculated within the independent-particle approximation (dashed) and the MCDF method performed in [163] as well as the experimental results presented in the same publication. From this figure we can deduce that although the many-electron electron calculation reaches better agreement with the experiment, the independent-particle approximation is still in rather good agreement. More importantly, the results of the present calculation still reflect the same energy dependence of the degree of linear polarization of the fluorescence photons and differs from the results calculated by MCDF method by approximately a constant factor.

The right side of Fig. 31 also presents the degree of linear polarization (in percentage) of the $L\alpha_{1,2}$ lines, however, this time, following two-photon ionization of a $2p_{3/2}$ electron of tungsten by an unpolarized beam. The x-axis show the combined energy of the two photons, i.e. the energy pumped into the atomic system. Already from the first glance, it becomes apparent that ionizing the neutral tungsten atom by two photons instead of one results in high sensitivity of the fluorescence photon (or ion) polarization on the incident photon energy. Even more intriguing are the physical origins of the peaks and troughs. At low photon energies, in the nonresonant region, the degree of linear polarization is rather comparable to the case of one-photon ionization, however at higher energies, this value changes dramatically due to intermediate level resonances and nonlinear Cooper minimum. The first and last peaks (and troughs) originate from the incident photon energy matching an intermediate $2p_{3/2} \to ns$ resonance, they have been marked by solid gray lines. The peaks marked with green dashed lines originate from the $2p_{3/2} \to 3d_{3/2,5/2}$ resonances. Lastly, the small peak marked with red dashed line originates from the zero contributions of the $2p_{3/2} \to nd$ channels, which corresponds to the nonlinear Cooper minimum (see Sec. 2.2.2). The detailed explanation of the origin of each of these phenomena was provided in previous examples in this and the previous chapter.

The comparison of the left and right plots of Fig. 31 demonstrates just how completely new behavior of the light-matter interaction can be achieved with nonlinear processes. While the left-hand side figure contains only information about the initial and final electron states, two-photon ionization allows us to probe the complete electron structure of atoms and use the same methods as in one-photon ionization case to obtain this information.

7 Summary and Outlook

In this thesis we theoretically studied one of the most fundamental nonlinear processes, the two-photon ionization. Using the independent particle approximation and relativistic second-order perturbation theory, we derived the most common quantities which are commonly obtained from measurements, the total cross section and photoelectron angular distributions. Moreover, we also investigated other measurable quantities such as the magnetic properties of the produced photoion as well as polarization properties of the subsequent fluorescence light. We explored the dependence of the cross section and polarization degrees on the incident photon energy and evaluated the contributions of relativistic effects. We also studied the properties of these quantities in the vicinity of the nonlinear Cooper minimum. We found out that in particular cases interesting effects such as minimum in the total cross section, elliptical dichroism in the photoelectron angular distributions or full polarization transfer from incident to fluorescence photons can be achieved at or near the nonlinear Cooper minimum.

To summarize this thesis in more detail, in the first section, we started by a historical overview of two-photon ionization process. The studies of this nonlinear process arose from the first theoretical consideration by Marie Göppert-Mayer [1] and significantly progressed with the first experiments which employed optical lasers. Recent efforts pushed the theoretical description to utilize ever more precise theory and describe the process within fully many-electron or relativistic approach. Experimentally, rapid increase of interest in two-photon ionization appeared with the fast development of free-electron lasers, which allow to probe the nonlinear dynamics in strongly bound electrons.

The aim of chapter 2 was to lay out the theoretical basis of relativistic and density matrix theory for the description of the two-photon ionization process. After a brief overview of the Dirac equation and its solutions in spherically symmetric potentials, the transition amplitude of the two-photon ionization was described within the framework of second-order perturbation theory and within independent particle approximation. From the properties of the transition amplitude, the concept of nonlinear Cooper minimum was deduced. With nonlinear Cooper minimum, we describe the photon energy at which the otherwise dominant ionization channel passes through zero due balance of ionization path spectra. This phenomenon, which always occurs for nonresonant photon energies which lays between any two level resonances of the same angular momentum, strongly impacts all observables of the two-photon ionization process. The numerical evaluation of the transition amplitudes which was employed in generating all results of this thesis was described.

The last subsection of the second chapter was used to introduce the concept of density matrix theory and to obtain the density matrix of the final state of the considered system. This density matrix fully describes all properties of both, the produced photoelectron as well as photoion and is the central expression of this thesis as it served as a starting point to each of the remaining chapters.

Chapter 3 was dedicated to the total two-photon ionization cross sections. Total cross sections for ionization of atomic s and p electrons were derived within electric dipole approximation to provide a simple tool for analytical analysis of two-photon ionization. Total two-photon ionization cross sections have been shown to have a local minimum at the nonlinear Cooper minimum. Since the energy position of this minimum is determined by the complete level spectrum of an atom, its experimental determination could serve as a sensitive tool to accurately test the agreement between theory and experiment.

In the third section, the contribution of relativistic effects to the total two-photon ionization cross section was evaluated. Relativistic and nonrelativistic calculations were

presented for various photon energies and for ionization of $1s$ electrons of atoms ranging from hydrogen to uranium. It was shown, that the relativistic wave function contractions is the dominant relativistic effect, while the contribution of higher multipoles of the photons or the contributions from the negative energy continuum were found to be less important. Significant dependence of the contributions of all relativistic effects on nuclear charge as well as the incident photon energy was shown. The last subsection of the third chapter discussed current experimental efforts and fully relativistic calculations were compared to the available experimental values of the total cross section for two-photon K shell ionization. From the comparison, it appears that the experiments which were performed with incident photon energies near the two-photon ionization threshold [24, 25, 27, 116] are generally in a good agreement with theory, while those utilizing photon energies near the one-photon ionization threshold [26, 38, 117] require more attention.

In section 4, the photoelectron angular distributions following two-photon atomic ionization were studied in detail. The dependence of the photoelectron emission direction on the photon polarization was studied and explained. Relativistic calculations of the distributions were compared to the nonrelativistic ones. It was demonstrated that the momentum transfer from the light to the atom included in higher multipole orders of the light-matter interaction result in increased emission into the forward direction in comparison to emission backwards. This forward-backward asymmetry in photoelectron emission increases with increasing photon energy and is more pronounced for heavier elements [66]. The photoelectron angular distributions were studied in the vicinity of nonlinear Cooper minimum and their strong variation close to this point was shown explicitly.

Section 4 also reports on an intriguing phenomenon called the elliptical dichroism. The elliptical polarization of the incident photons results in a unique left-right asymmetry of the photoelectron angular distributions in two-photon ionization of atoms. This asymmetry is present also for ionization of unpolarized atoms, which is the dominant difference from the well-known circular dichroism in photoionization process. The physical as well as mathematical origins of this asymmetry were unveiled and the conditions to achieve the maximum of this effect were presented. Lastly, comparison with experimentally measured photoelectron angular distributions were presented and a proposal for experimental detection of the elliptical dichroism in two-photon ionization of helium was shown.

Section 5 explored the state of a photoion following the two-photon ionization process. The meaning of ion polarization was defined and the magnetic substate populations of atoms after two-photon s and p electron ionization were investigated for different incident photon polarization. While producing a high degree of ion polarization by two-photon ionization of the s electron is generally ineffective, ionization of p electrons results in much higher degree of polarization. A strong deviations of the ion polarization can be achieved at the nonlinear Cooper minimum where the polarization strongly increases. This is, in particular, the case for atomic ionization by circularly polarized light, for which the ion polarization reaches its maximum. A detection scheme based on this atomic response could serve for a precise determination of the position of nonlinear Cooper minimum. By measuring the ion polarization, atomic ionization parameters (such as transition amplitudes) could be extracted, which could lead to resolving of current discrepancies. An example how to resolve the discrepancy in the total two-photon ionization cross section of helium-like neon [38, 118] was proposed.

Detection of fluorescence photons is a common technique to experimentally measure the K (or inner) shell two-photon ionization process [24–27]. Chapter 6 discusses the polarization properties of such fluorescence photons as well as their angular distributions. The polarization transfer from the incident to the fluorescence photons

is studied for different incident photon polarization. The extrema of the polarization transfer at the nonlinear Cooper minimum were discussed for both, creation of s and p vacancies by two-photon ionization. The strong fluorescence polarization signals at nonlinear Cooper minimum could serve for experimental determination of the positions of the Cooper minimum, and hence, to an accurate test of the theory of the nonlinear interaction as well as atomic structure. Realistic examples were presented to motivate new experiments to be performed.

This work was mainly motivated by the new experimental opportunities offered by the free-electron lasers. The development of these high energetic intense light sources proceeds and new spectacular beam properties are becoming available by upgrades of standing free-electron lasers as well as in new facilities. This continuing grow of free-electron laser science and its countless number of possibilities provide motivation for further theoretical research of interaction of atoms with strong fields. For example, the seeded operation at the FERMI free-electron laser in Trieste Italy is capable of producing pulses with narrow beam width. This unique feature of the FERMI laser would readily allow detailed investigations of the nonlinear Cooper minima discussed in this thesis, while free-electron lasers based on SASE operation could made such studies cumbersome.

The polarization control of the free-electron laser pulses is becoming a popular topic and is included in number of plans for upgrades of free-electron laser facilities. In this work we have shown, that elliptically and circularly polarized beams open new possibilities in spectroscopy as well as in quantum control. The polarization control of XUV beams would of course be also beneficial in other fields such as quantum chemistry, material science and molecular physics where the chirality of the target could be probed.

One particularly interesting upgrade plan is the two-color operation of the free-electron lasers which has been mentioned on recent conferences (at the time of writing). So far, two-color experiments have been restricted to overlapping the XUV pulses with IR lasers. The two-color operation of free-electrons would allow us to move past this restriction and investigate XUV pump and XUV probe schemes or the interplay of different ionization channels. For example, by overlapping a beam with energy ω and one with lower intensity but double the energy 2ω, one could investigate the interference of one- and two-photon ionization paths in the XUV or x-ray regime [164, 165] or to boost the total cross section in order to investigate nonlinear effects such as the elliptical dichroism.

With the increasing intensities of the free-electron electron lasers, it becomes easier to investigate multi-photon absorption dynamics beyond two-photon ionization. There is no question about the presence of nonlinear Cooper minima in three- and more photon ionization. However, with the number of absorbed photons, the number of possible ionization channels also increases. Hence, the question arises what atomic behavior is there to discover at many-photon ionization at these minima. Will the strong responses of atomic systems presented in this work diminish, or are there yet unnoticed effects waiting to be explored? A similar question applies to the threshold effects we have seen in this work. With increasing number of absorbed photons, the angular momentum of the photoelectrons increases. If the threshold effects originate from the centrifugal potential barrier, will the amplitude dynamics near threshold be even more pronounced in the case of many-photon ionization? The understanding of the two-photon ionization might hint the answers to some of these questions, however, further theoretical as well as experimental efforts are needed to fill in the gaps in our understanding explicitly.

During calculations of the cross sections of two-photon ionization of inner-shell electrons and in particular the properties of subsequent fluorescence photons, the inde-

pendent particle approximation came short on reproducing the many-electron atomic structure. It would be indeed very interesting to extend the current effective one-electron theory into many-electron theory. This would allow us to perform the calculation to practically any atomic system. Moreover, it would be possible to test the representation of the complete many-electron spectrum near the nonlinear Cooper minimum as well as to extend the included process of relaxation of the produced photoions by including for example Auger decays (this has been done for one-photon ionization, see e.g. [152]). A promising opportunity to perform many-electron calculations of two-photon ionization lays in the recently published software JAC [50] which aims to provide all building blocks for the necessary code.

There have been few recent experiments, where two-photon ionization is performed near the one-photon ionization threshold [26, 117]. Due to the excitation of the Rydberg manifold, the corresponding total cross sections exceed the scaling law introduced by Zernik [21]. There are further plans to perform similar experiments, however, with an additional overlap of the free-electron laser pulses with a IR laser beam. Previously, a similar experiment challenged our understanding of nonlinear light-matter interaction in one of the simplest systems, the helium atom [45]. It is therefore an interesting question what happens when such an experiment is performed for much heavier elements with the excitation of the Rydberg states. Near future experimental as well as theoretical efforts will attempt to pin point this issue and deepen our understanding of atomic response in such extreme conditions.

The last few paragraphs sketch a few possibilities of further theoretical research ideas. There are of course many more then mentioned here, however, their discussion would exceed the limits of this thesis. All these unanswered questions motive us to carry out more precise calculations, predict hitherto unobserved effect and to put our theoretical predictions to a test at experimental facilities. Let's keep exploring!

Appendices

For completeness, this appendix briefly lists the definitions and some important properties of the special functions occurring in the thesis. More detailed treatments can be found in the relevant literature. For example, the Atomic Structure Theory from W. R. Johnson [70] is particularly useful, or the Relativistic Atomic Collisions from J. Eichler and W. E. Meyerhof [69].

A Used Angular Momentum Theory Relations

The *Wigner-Eckart theorem* states that matrix elements of spherical tensor operators in the basis of angular momentum eigenstates can be expressed as

$$\langle j_f m_f \,|\, T_{JM} \,|\, j_i m_i \rangle = \frac{(-1)^{2J}}{[j_f]} \langle j_i m_i JM \,|\, j_f m_f \rangle \langle j_f \,\|T_J\|\, j_i \rangle \,, \tag{A.1}$$

where the reduced matrix element $\langle j_f \,\|T_J\|\, j_i \rangle$ is independent of angular momentum orientation, and $\langle j_i m_i JM \,|\, jm \rangle$ is a Clebsch–Gordan coefficient. This theorem is widely used in quantum physics and its proof and examples of applications can be found for example in Ref. [70].

To derive the total ionization cross section, one needs to count electrons emitted all directions. Theoretically, this means that we need to integrate over the two angles defining the photoelectron emission direction. The angular dependence of spherically symmetric electron wave functions are given by spherical harmonics. The orthogonality of spherical harmonics dictates

$$\int d\Omega Y_{lm}(\theta,\phi) Y^*_{l'm'}(\theta,\phi) = \delta_{ll'}\delta_{mm'}. \tag{A.2}$$

The consequence of the orthogonality is, that the total two-photon ionization cross section does not contain any interference between different ionization channels with a different final photoelectron partial wave. The Orthogonality of Clebsch-Gordan coefficients

$$\sum_{m_1,m_2} \langle j_1 m_1, j_2 m_2 \,|\, jm \rangle \langle j_1 m_1, j_2 m_2 \,|\, j'm' \rangle = \delta_{jj'}\delta_{mm'} \tag{A.3}$$

allows for further simplification of the total cross section expression.

To obtain a density matrix from a statistical tensor, the following transformation may be used.

$$\langle \alpha JM \,|\hat{\rho}|\, \alpha JM' \rangle = \sum_{kq} (-1)^{J-M'} \langle JMJ - M'|kq\rangle \, \rho_{kq}\,(\alpha J)\,. \tag{A.4}$$

One of the advantages of the statistical tensors, is that they can be transformed similar to the spherical harmonics of rank k under a rotation of the coordinates .

B Scattering cross sections

Transition rates are the typical quantity to describe any scattering process. The general transition rate describing number of particles n_s scattered into an interval $\mathbf{p}_r$ for a unit time and in unit volume is [166]

$$dW_{p\to p'} = (2\pi)^{3s+1} n_1 ... n_s |T_{p'p}|^2 \delta(E_p - E_{p'}) d\mathbf{p'}_1 .... d\mathbf{p'}_r, \tag{B.1}$$

where $d\mathbf{p}$ and $d\mathbf{p'}$ are the initial and final states of the system, T is the transition amplitude

$$d\boldsymbol{p} = |\boldsymbol{p}|^2 dp d\Omega = E_e |\boldsymbol{p}| dE_e d\Omega. \tag{B.2}$$

The corresponding cross section is then

$$d\sigma^{(s)} = \frac{W_{p\to p'}}{j^s}, \tag{B.3}$$

with j being the current of initial particles (nc for photons, nv for electrons, where v is the velocity of the initial electron in the nucleus frame).

For two-photon ionization, we have $s = 2$. Hence, the angle differential cross section is

$$\frac{d\sigma}{d\Omega} = \frac{8\pi^3\alpha^2}{\omega^2}|T_{p'p}|^2, \tag{B.4}$$

where the normalization factors $\frac{1}{\epsilon_e|\boldsymbol{p}_e|}$ and $\frac{e}{\sqrt{(2\pi)^3 2\omega}}$ of the photoelectron and photon wave functions have been taken out of the transition amplitudes.

C Radial integrals

The key component of the one-electron transition amplitudes (2.20) are the radial integrals of the electron wave functions (Eq.(2.22)). In the transverse (velocity) gauge, these integrals are explicitly given for the magnetic ($p = 0 = M$) transitions

$$R_{\kappa_f\kappa_i}(MJ) = \int_0^\infty dr \frac{\kappa_i + \kappa_j}{J+1} j_J(kr) \left[P_i(r)Q_j(r) + Q_i(r)P_j(r)\right] \tag{C.1}$$

and electric for the electric transitions ($p = 1 = E$)

$$\begin{aligned} R_{\kappa_f\kappa_i}(EJ) &= \int_0^\infty dr \left\{ -\frac{\kappa_i - \kappa_j}{J+1}\left[j'_J(kr) + \frac{j_J(kr)}{kr}\right]\left[P_i(r)Q_j(r) + Q_i(r)P_j(r)\right] \right. \\ &\times \left. +J\frac{j_J(kr)}{kr}\left[P_i(r)Q_j(r) - Q_i(r)P_j(r)\right]\right\}. \end{aligned} \tag{C.2}$$

In the length gauge, this integral is given by

$$\begin{aligned} R_{\kappa_f\kappa_i}(EJ) &= \int_0^\infty dr \left\{ j_J(kr)\left[P_i(r)P_j(r) + Q_i(r)Q_j(r)\right] \right. \\ &+ j_{J+1}(kr)\left[\frac{\kappa_i - \kappa_j}{J+1}\left[P_i(r)Q_j(r) + Q_i(r)P_j(r)\right]\right. \\ &+ \left.\left.\left[P_i(r)Q_j(r) - Q_i(r)P_j(r)\right]\right]. \end{aligned} \tag{C.3}$$

In the above expressions, $j_J(x)$ are the spherical Bessel functions.

Bibliography

[1] M. Goeppert-Mayer, Ann. Phys. (Leipzig) **9**, 273 (1931).

[2] E. Siegman, Anthony, *Laser* (University Science Books, Sausalito, California, 1976).

[3] P. Lambropoulos, Phys. Rev. Lett. **28**, 585 (1972).

[4] P. Lambropoulos, Phys. Rev. Lett. **29**, 453 (1972).

[5] A. Saenz and P. Lambropoulos, Journal of Physics B: Atomic, Molecular and Optical Physics **32**, 5629 (1999).

[6] M. G. Makris, P. Lambropoulos, and A. Mihelič, Phys. Rev. Lett. **102**, 033002 (2009).

[7] S. Fritzsche, A. N. Grum-Grzhimailo, E. V. Gryzlova, and N. M. Kabachnik, Journal of Physics B: Atomic, Molecular and Optical Physics **41**, 165601 (2008).

[8] A. N. Grum-Grzhimailo, E. V. Gryzlova, S. I. Strakhova, N. M. Kabachnik, and S. Fritzsche, Journal of Physics: Conference Series **194**, 012004 (2009).

[9] E. V. Gryzlova *et al.*, Phys. Rev. A **84**, 063405 (2011).

[10] L. Argenti *et al.*, Phys. Rev. A **87**, 053405 (2013).

[11] L. V. Keldysh, JETP **20**, 1307 (1965).

[12] T. Nubbemeyer, K. Gorling, A. Saenz, U. Eichmann, and W. Sandner, Phys. Rev. Lett. **101**, 233001 (2008).

[13] D. B. Milošević, Phys. Rev. A **74**, 063404 (2006).

[14] D. R. Austin and J. Biegert, Phys. Rev. A **86**, 023813 (2012).

[15] W. Paufler, B. Böning, and S. Fritzsche, Phys. Rev. A **98**, 011401 (2018).

[16] B. Böning, W. Paufler, and S. Fritzsche, Phys. Rev. A **99**, 053404 (2019).

[17] W. Kaiser and C. G. B. Garrett, Phys. Rev. Lett. **7**, 229 (1961).

[18] I. D. Abella, Phys. Rev. Lett. **9**, 453 (1962).

[19] J. L. Hall, E. J. Robinson, and L. M. Branscomb, Phys. Rev. Lett. **14**, 1013 (1965).

[20] R. L. Smith, Phys. Rev. **128**, 2225 (1962).

[21] W. Zernik, Phys. Rev. **135**, A51 (1964).

[22] E. Karule, Journal of Physics B: Atomic and Molecular Physics **4**, L67 (1971).

[23] S. Klarsfeld, Lettere al Nuovo Cimento **3**, 395 (1970).

[24] K. Tamasaku *et al.*, Nat. Photonincs **8**, 313 (2014).

[25] S. Ghimire *et al.*, Phys. Rev. A **94**, 043418 (2016).

[26] J. Szlachetko *et al.*, Sci. Rep. **6**, 33292 (2016).

[27] K. Tamasaku *et al.*, Phys. Rev. Lett. **121**, 083901 (2018).

[28] V. Florescu, O. Budriga, and H. Bachau, Phys. Rev. A **84**, 033425 (2011).

[29] V. Florescu, O. Budriga, and H. Bachau, Phys. Rev. A **86**, 033413 (2012).

[30] P. Koval, S. Fritzsche, and A. Surzhykov, Journal of Physics B: Atomic, Molecular and Optical Physics **37**, 375 (2003).

[31] P. Koval, *Two-photon ionization of atomic inner-shells* (Doctoral Thesis, Universität Kassel, 2004).

[32] Y. Kobayashi, T. Sekikawa, Y. Nabekawa, and S. Watanabe, Opt. Lett. **23**, 64 (1998).

[33] Y. Kobayashi, T. Ohno, T. Sekikawa, Y. Nabekawa, and S. Watanabe, Applied Physics B **70**, 389 (2000).

[34] N. A. Papadogiannis, L. A. A. Nikolopoulos, D. Charalambidis, G. D. Tsakiris, P. Tzallas, and K. Witte, Phys. Rev. Lett. **90**, 133902 (2003).

[35] J. M. J. Madey, Journal of Applied Physics **42**, 1906 (1971).

[36] C. Pellegrini, The European Physical Journal H **37**, 659 (2012).

[37] M. Richter, S. V. Bobashev, A. A. Sorokin, and K. Tiedtke, Journal of Physics B: Atomic, Molecular and Optical Physics **43**, 194005 (2010).

[38] G. Doumy *et al.*, Phys. Rev. Lett. **106**, 083002 (2011).

[39] P. Lambropoulos, K. G. Papamihail, and P. Decleva, Journal of Physics B: Atomic, Molecular and Optical Physics **44**, 175402 (2011).

[40] H. Fukuzawa *et al.*, Phys. Rev. Lett. **110**, 173005 (2013).

[41] L. Young *et al.*, Nature **466**, 56 (2010).

[42] K. Motomura *et al.*, Journal of Physics B: Atomic, Molecular and Optical Physics **46**, 164024 (2013).

[43] A. N. Grum-Grzhimailo, E. V. Gryzlova, S. Fritzsche, and N. M. Kabachnik, Journal of Modern Optics **63**, 334 (2016).

[44] K. Toyota, S.-K. Son, and R. Santra, Phys. Rev. A **95**, 043412 (2017).

[45] M. Ilchen *et al.*, Phys. Rev. Lett. **118**, 013002 (2017).

[46] M. Ilchen *et al.*, Nat. Commun. **9**, 4659 (2018).

[47] B. M. Lagutin, I. D. Petrov, V. L. Sukhorukov, P. V. Demekhin, A. Knie, and A. Ehresmann, Phys. Rev. A **95**, 063414 (2017).

[48] I. D. Petrov, B. M. Lagutin, V. L. Sukhorukov, A. Knie, and A. Ehresmann, Phys. Rev. A **93**, 033408 (2016).

[49] S.-K. Son, L. Young, and R. Santra, Phys. Rev. A **83**, 033402 (2011).

[50] S. Fritzsche, Computer Physics Communications **240**, 1 (2019).

[51] A. K. Kazansky and N. M. Kabachnik, Journal of Physics B: Atomic, Molecular and Optical Physics **40**, 2163 (2007).

[52] Y. V. Vanne and A. Saenz, Phys. Rev. A **85**, 033411 (2012).

[53] A. Jiménez-Galán, L. Argenti, and F. Martín, Phys. Rev. Lett. **113**, 263001 (2014).

[54] N. Douguet, A. N. Grum-Grzhimailo, and K. Bartschat, Phys. Rev. A **95**, 013407 (2017).

[55] I. V. Ivanova, V. M. Shabaev, D. A. Telnov, and A. Saenz, Phys. Rev. A **98**, 063402 (2018).

[56] R. Ma *et al.*, Journal of Physics B: Atomic, Molecular and Optical Physics **46**, 164018 (2013).

[57] K. Ishikawa and K. Ueda, Appl. Sci. **3**, 189 (2013).

[58] S. Mondal *et al.*, Journal of Physics B: Atomic, Molecular and Optical Physics **46**, 205601 (2013).

[59] J. W. Cooper, Phys. Rev. **128**, 681 (1962).

[60] J. W. Cooper, Phys. Rev. Lett. **13**, 762 (1964).

[61] M. G. White, S. H. Southworth, P. Kobrin, E. D. Poliakoff, R. A. Rosenberg, and D. A. Shirley, Phys. Rev. Lett. **43**, 1661 (1979).

[62] W. R. Johnson and K. T. Cheng, Phys. Rev. Lett. **40**, 1167 (1978).

[63] J. L. Dehmer and D. Dill, Phys. Rev. Lett. **37**, 1049 (1976).

[64] J. Hofbrucker, A. V. Volotka, and S. Fritzsche, Phys. Rev. A **94**, 063412 (2016).

[65] J. Hofbrucker, A. Volotka, and S. Fritzsche, Nucl. Instr. Meth. Phys. Res. Sect. B **408**, 125 (2017).

[66] J. Hofbrucker, A. V. Volotka, and S. Fritzsche, Phys. Rev. A **96**, 013409 (2017).

[67] J. Hofbrucker, A. V. Volotka, and S. Fritzsche, Phys. Rev. Lett. **121**, 053401 (2018).

[68] J. Hofbrucker, A. V. Volotka, and S. Fritzsche, Phys. Rev. A **100**, 011401(R) (2019).

[69] J. Eichler and W. E. Meyerhof, *Relativistic Atomic Collisions* (Academic Press, San Diego, 1995).

[70] W. R. Johnson, *Atomic Structure Theory Lecture on Atomic Physics* (Springer, Berlin, 2007).

[71] D. A. Varshalovich, A. N. Moskalev, and V. K. Khersonskii, *Quantum Theory Of Angular Momemtum* (World Scientific, Singapore, New Jerseu, Hong Kong, 1988).

[72] V. V. Balashov, A. N. Grum-Grzhimailo, and N. M. Kabaschnik, *Polarization and Correlation Phenomena in Atomic Collisions* (Springer, New York, 2000).

[73] J. Eichler and T. Stöhlker, Physics Reports **439**, 1 (2007).

[74] U. Fano, Phys. Rev. A **32**, 617 (1985).

[75] R. S. Berry, The Journal of Chemical Physics **45**, 1228 (1966).

[76] D. Busto *et al.*, Phys. Rev. Lett. **123**, 133201 (2019).

[77] H. Derenbach and V. Schmidt, Journal of Physics B: Atomic and Molecular Physics **16**, L337 (1983).

[78] A. Fahlman, T. A. Carlson, and M. O. Krause, Journal of Physics B: Atomic and Molecular Physics **16**, L485 (1983).

[79] O. Hemmers *et al.*, Phys. Rev. Lett. **91**, 053002 (2003).

[80] S. Saha *et al.*, Phys. Rev. A **90**, 053406 (2014).

[81] L. Argenti, A. Jiménez-Galán, J. Caillat, R. Taïeb, A. Maquet, and F. Martín, Phys. Rev. A **95**, 043426 (2017).

[82] G. W. F. Drake and Z.-C. Yan, Canadian Journal of Physics **86**, 45 (2008).

[83] B. M. Henson *et al.*, Phys. Rev. Lett. **115**, 043004 (2015).

[84] Y.-H. Zhang, L.-Y. Tang, X.-Z. Zhang, and T.-Y. Shi, Phys. Rev. A **93**, 052516 (2016).

[85] J. Sapirstein and W. R. Johnson, Journal of Physics B: Atomic, Molecular and Optical Physics **29**, 5213 (1996).

[86] V. M. Shabaev, I. I. Tupitsyn, V. A. Yerokhin, G. Plunien, and G. Soff, Phys. Rev. Lett. **93**, 130405 (2004).

[87] A. V. Volotka, A. Surzhykov, V. M. Shabaev, and G. Plunien, Phys. Rev. A **83**, 062508 (2011).

[88] A. Surzhykov *et al.*, Phys. Rev. A **81**, 042510 (2010).

[89] A. V. Volotka, V. A. Yerokhin, A. Surzhykov, T. Stöhlker, and S. Fritzsche, Phys. Rev. A **93**, 023418 (2016).

[90] F. Salvat, J. Fernández-Varea, and W. Williamson, Computer Physics Communications **90**, 151 (1995).

[91] A. C. Thompson and *et al.*, *X-Ray Data Booklet, 3rd ed.* (Lawrence Berkeley National Laboratory, University of California, 2009).

[92] F. Salvat, J. D. Martnez, R. Mayol, and J. Parellada, Phys. Rev. A **36**, 467 (1987).

[93] J. P. Perdew and A. Zunger, Phys. Rev. B **23**, 5048 (1981).

[94] W. Kohn and L. J. Sham, Phys. Rev. **140**, A1133 (1965).

[95] J. C. Slater, Phys. Rev. **81**, 385 (1951).

[96] J. v. Neumann, Nachrichten von der Gesellschaft der Wissenschaften zu Göttingen, Mathematisch-Physikalische Klasse **1927**, 245 (1927).

[97] U. Fano, Rev. Mod. Phys. **29**, 74 (1957).

[98] K. Blum, *Density Matrix Theory and Applications* (Springer, Berlin Heidelberg, 2012).

[99] Z. W. Wu, A. V. Volotka, A. Surzhykov, C. Z. Dong, and S. Fritzsche, Phys. Rev. A **93**, 063413 (2016).

[100] L. Sharma, A. Surzhykov, M. K. Inal, and S. Fritzsche, Phys. Rev. A **81**, 023419 (2010).

[101] A. A. Peshkov, D. Seipt, A. Surzhykov, and S. Fritzsche, Phys. Rev. A **96**, 023407 (2017).

[102] D. Seipt, D. Del Sorbo, C. P. Ridgers, and A. G. R. Thomas, Phys. Rev. A **98**, 023417 (2018).

[103] G. S. Thekkadath *et al.*, Phys. Rev. Lett. **117**, 120401 (2016).

[104] N. B. Delone and V. P. Krainov, *Multiphoton Processes in Atoms* (Springer, Berlin, Heidelberg, New York, 2000).

[105] N. L. Manakov, S. I. Marmo, and S. A. Sviridov, Journal of Experimental and Theoretical Physics **108**, 557 (2009).

[106] K. T. Cheng and C. F. Fischer, Phys. Rev. A **28**, 2811 (1983).

[107] K. T. Cheng and W. R. Johnson, Phys. Rev. A **28**, 2820 (1983).

[108] T. Kjellsson, S. Selstø, and E. Lindroth, Phys. Rev. A **95**, 043403 (2017).

[109] T. K. Lindblom, M. Førre, E. Lindroth, and S. Selstø, Phys. Rev. Lett. **121**, 253202 (2018).

[110] L. N. Labzowsky, A. V. Shonin, and D. A. Solovyev, Journal of Physics B: Atomic, Molecular and Optical Physics **38**, 265 (2005).

[111] A. Surzhykov, J. P. Santos, P. Amaro, and P. Indelicato, Phys. Rev. A **80**, 052511 (2009).

[112] J. A. Duncanson, M. P. Strand, A. Lindgård, and R. S. Berry, Phys. Rev. Lett. **37**, 987 (1976).

[113] A. Siegel, J. Ganz, W. Bussert, and H. Hotop, Journal of Physics B: Atomic and Molecular Physics **16**, 2945 (1983).

[114] A. Dodhy, R. N. Compton, and J. A. D. Stockdale, Phys. Rev. Lett. **54**, 422 (1985).

[115] Z.-M. Wang and D. S. Elliott, Phys. Rev. A **62**, 053404 (2000).

[116] H. Hasegawa, E. J. Takahashi, Y. Nabekawa, K. L. Ishikawa, and K. Midorikawa, Phys. Rev. A **71**, 023407 (2005).

[117] K. Tyrała *et al.*, Phys. Rev. A **99**, 052509 (2019).

[118] A. Sytcheva, S. Pabst, S.-K. Son, and R. Santra, Phys. Rev. A **85**, 023414 (2012).

[119] S. A. Novikov and A. N. Hopersky, Journal of Physics B: Atomic, Molecular and Optical Physics **34**, 4857 (2001).

[120] M. Vogel *et al.*, Hyperfine Interactions **236**, 65 (2015).

[121] J. M. Dahlström, A. L'Huillier, and A. Maquet, Journal of Physics B: Atomic, Molecular and Optical Physics **45**, 183001 (2012).

[122] E. Lindroth and J. M. Dahlström, Phys. Rev. A **96**, 013420 (2017).

[123] L. Argenti and R. Moccia, Journal of Physics B: Atomic, Molecular and Optical Physics **43**, 235006 (2010).

[124] N. L. Manakov, A. Maquet, S. I. Marmo, V. Veniard, and G. Ferrante, Journal of Physics B: Atomic, Molecular and Optical Physics **32**, 3747 (1999).

[125] G. Baum, M. S. Lubell, and W. Raith, Phys. Rev. Lett. **25**, 267 (1970).

[126] N. A. Cherepkov, V. V. Kuznetsov, and V. A. Verbitskii, Journal of Physics B: Atomic, Molecular and Optical Physics **28**, 1221 (1995).

[127] A. N. Grum-Grzhimailo, Journal of Physics B: Atomic, Molecular and Optical Physics **34**, L359 (2001).

[128] P. V. Demekhin, Phys. Rev. A **99**, 063406 (2019).

[129] G. D. Fasman, *Circular Dichroism and the Conformational Analysis of Biomolecules* (Springer, Berlin, Heidelberg, New York, 1996).

[130] S. Beaulieu *et al.*, Nature Physics **14**, 484 (2018).

[131] S. A. Mousavi, E. Plum, J. Shi, and N. I. Zheludev, Scientific Reports **5**, 8977 EP (2015), article.

[132] A. B. Khanikaev *et al.*, Nature Communications **7**, 12045 EP (2016), article.

[133] M. Bashkansky, P. H. Bucksbaum, and D. W. Schumacher, Phys. Rev. Lett. **60**, 2458 (1988).

[134] A. Kassaee, M. L. Rustgi, and S. A. T. Long, Phys. Rev. A **37**, 999 (1988).

[135] P. Lambropoulos and X. Tang, Phys. Rev. Lett. **61**, 2506 (1988).

[136] H. G. Muller, G. Petite, and P. Agostini, Phys. Rev. Lett. **61**, 2507 (1988).

[137] S. Basile, F. Trombetta, and G. Ferrante, Phys. Rev. Lett. **61**, 2435 (1988).

[138] A. Jaroń, J. Kamiński, and F. Ehlotzky, Optics Communications **163**, 115 (1999).

[139] G. G. Paulus *et al.*, Phys. Rev. Lett. **80**, 484 (1998).

[140] G. G. Paulus *et al.*, Phys. Rev. Lett. **84**, 3791 (2000).

[141] Z.-M. Wang and D. S. Elliott, Phys. Rev. Lett. **84**, 3795 (2000).

[142] F. Dulieu, C. Blondel, and C. Delsart, Journal of Physics B: Atomic, Molecular and Optical Physics **28**, 3845 (1995).

[143] J. Colgan and M. S. Pindzola, Phys. Rev. Lett. **86**, 1998 (2001).

[144] B. Borca, M. V. Frolov, N. L. Manakov, and A. F. Starace, Phys. Rev. Lett. **87**, 133001 (2001).

[145] M. Meyer *et al.*, Phys. Rev. Lett. **101**, 193002 (2008).

[146] A. K. Kazansky, A. V. Grigorieva, and N. M. Kabachnik, Phys. Rev. Lett. **107**, 253002 (2011).

[147] M. Ilchen *et al.*, Phys. Rev. Lett. **112**, 023001 (2014).

[148] L. H. Haber, B. Doughty, and S. R. Leone, Phys. Rev. A **79**, 031401 (2009).

[149] E. G. Berezhko and N. M. Kabachnik, Journal of Physics B: Atomic and Molecular Physics **10**, 2467 (1977).

[150] S. Fritzsche, A. Surzhykov, and T. Stöhlker, Phys. Rev. A **72**, 012704 (2005).

[151] H. Klar, Journal of Physics B: Atomic and Molecular Physics **13**, 3117 (1980).

[152] N. M. Kabachnik and O. V. Lee, Journal of Physics B: Atomic, Molecular and Optical Physics **22**, 2705 (1989).

[153] T. Suzuki and Y. Yamauchi, Phys. Rev. A **77**, 022902 (2008).

[154] A. A. Lutman *et al.*, Nature Photonics **10**, 468 (2016).

[155] E. Allaria *et al.*, Nat. Photonics **7**, 913 (2013).

[156] E. A. Schneidmiller and M. V. Yurkov, Phys. Rev. ST Accel. Beams **16**, 110702 (2013).

[157] B. Faatz *et al.*, Applied Sciences **7**, 1114 (2017).

[158] P. Linstrom and W. Mallard, Eds., NIST Chemistry WebBook, NIST Standard Reference Database Number 69, National Institute of Standards and Technology, Gaithersburg MD, 20899 (retrieved 03/05/2019).

[159] N. R. Badnell, D. Petrini, and S. Stoica, Journal of Physics B: Atomic, Molecular and Optical Physics **30**, L665 (1997).

[160] M. Wünsche *et al.*, Review of Scientific Instruments **90**, 023108 (2019).

[161] M. Žitnik *et al.*, Phys. Rev. Lett. **113**, 193201 (2014).

[162] P. Lambropoulos, *Advances in Atomic and Molecular Physics* (Academic Press, New York, 1976).

[163] T. Kämpfer *et al.*, Phys. Rev. A **93**, 033409 (2016).

[164] A. N. Grum-Grzhimailo, E. V. Gryzlova, E. I. Staroselskaya, J. Venzke, and K. Bartschat, Phys. Rev. A **91**, 063418 (2015).

[165] N. Douguet, E. V. Gryzlova, E. I. Staroselskaya, K. Bartschat, and A. N. Grum-Grzhimailo, Eur. Phys. J. D **71**, 105 (2017).

[166] A. I. Achiezer and V. B. Berestecky, *Quantum electrodynamics* (Nauka, Moscow, 1969).

Acknowledgements

During very enjoyable PhD study years, I was guided, supported and motivated by many people, who deserve my gratitude. I would like to use this space to do just that.

I would like to start by expressing my deepest appreciation to Dr. Andrey V. Volotka, who patiently supervised me over the years. His explosive enthusiasm about new physics ideas always inspired and motivated me to work harder. The completion (or even start) of my thesis would not be possible without Prof. Dr. Stephan U. Fritzsche who came up with the original topic of my work and who guided and supported me to speak like, write like or simply to be a physicist. His achievements in our field of physics still drive me to work harder. I would also like to thank all of my current and former colleagues from the theoretical atomic physics group in the Helmholtz Institute Jena for their continuous feedback on my work: Dr. Zhongwen Wu, Dr. Anton Peshkov, Dr. Randolf Beerwerth, Willi Paufler, Dr. Moazzam Bilal, Birger Böning, Shahram Panahiyan, Valeriia Kosheleva, Sebastian Stock, Baghdasar Baghdasaryan, Jiahao Fan, Dmitrii Samoilenko, Dr. Robert Müller, Dr. Daniel Seipt, Prof. Andrey Surzhykov, and Dr. Biplab Goswami. I am also grateful to the Research School of Advanced Photon Science, the Helmholtz Graduate School for Hadron and Ion Research, the GSI Helmholtzzentrum für Schwerionenforschung as well as the Friedrich Schiller University Jena for making my studies possible. I also cannot thank enough Dr. Markus Ilchen whose attitude and endless dedication to push his research forward is truly motivating.

I would never get to this point without the support of my family, my parents Jiří and Jitka Hofbruckerovi, my sister Jana Hofbruckerová and my brother with his family Pavel, Eva and Anička Hofbruckerovi. Děkuji Vám za vše! For over eight years now, I have been supported and encouraged by the love of my life, my wife Sarah Hofbrucker-MacKenzie. As a brilliant researcher herself, she widens my horizon and motivates me in scientific thinking. My deepest gratitude also goes to my parents-in-law, sisters-in-law and twin-in-law for their trust and support.

I surely need to thank my pre-PhD educators, my high school teacher Zdeněk Máša who always sparkled my curiosity in his classes. I also wish to thank Prof. Norval Strachan and Dr. Ovidiu Rotariu for engaging me in my first research project as well as Dr. Stefan Diehl, Prof. Marco Thiel and Prof. Björn Schelter for their supervision of my project during my bachelor studies.

Publications

As part of my PhD studies, I contributed to the following publications:

- *Relativistic calculations of the nonresonant two-photon ionization of neutral atoms*
  J. Hofbrucker, A. V. Volotka, and S. Fritzsche
  Phys. Rev. A **94**, 063412 (2016).

- *Relativistic effects in the non-resonant two-photon K-shell ionization of neutral atoms*
  J. Hofbrucker, A. V. Volotka, and S. Fritzsche
  Nucl. Instr. Meth. B **408**, 125 (2017).

- *Photoelectron distribution of nonresonant two-photon ionization of neutral atoms*
  J. Hofbrucker, A. V. Volotka, and S. Fritzsche
  Phys. Rev. A **96**, 013409 (2017).

- *Maximum Elliptical Dichroism in Atomic Two-Photon Ionization*
  J. Hofbrucker, A. V. Volotka, and S. Fritzsche
  Phys. Rev. Lett **121**, 053401 (2018).

- *Fluorescence polarization as a precise tool for understanding nonlinear photoionization*
  J. Hofbrucker, A. V. Volotka, and S. Fritzsche
  Phys. Rev. A **100**, 011401(R) (2019).

- *Breakdown of electric dipole approximation at Cooper minima in direct two-photon ionisation*
  J. Hofbrucker, A. V. Volotka, and S. Fritzsche
  Sci. Rep. **10**, 3617 (2020).

Ehrenwörtliche Erklärung

Ich erkläre hiermit ehrenwörtlich, dass ich die vorliegende Arbeit selbstständig, ohne unzulässige Hilfe Dritter und ohne Benutzung anderer als der angegebenen Hilfsmittel und Literatur angefertigt habe. Die aus anderen Quellen direkt oder indirekt übernommenen Daten und Konzepte sind unter Angabe der Quelle gekennzeichnet.

Bei der Auswahl und Vorbereitung dieser Arbeit haben mir meine Betreuer und die Koautoren der oben genannten Publikationen unentgeldlich geholfen.

Weitere Personen waren an der inhaltlich-materiellen Erstellung der vorliegenden Arbeit nicht beteiligt. Insbesondere habe ich hierfür nicht die entgeltliche Hilfe von Vermittlungs- bzw. Beratungsdiensten (Promotionsberater oder andere Personen) in Anspruch genommen. Niemand hat von mir unmittelbar oder mittelbar geldwerte Leistungen für Arbeiten erhalten, die im Zusammenhang mit dem Inhalt dervorgelegten Dissertation stehen.

Die Arbeit wurde bisher weder im In- noch im Ausland in gleicher oder ähnlicher Form einer anderen Prüfungsbehörde vorgelegt.

Die geltende Promotionsordnung der Physikalisch-Astronomischen Fakultät ist mir bekannt.

Ich versichere ehrenwörtlich, dass ich nach bestem Wissen die reine Wahrheit gesagt und nichts verschwiegen habe.

Jena, den

.....
Jiri Hofbrucker

Curriculum Vitae

Personal information

Name	Jiří Hofbrucker
Date of Birth	19.02.1992
Place of Birth	Ivančice

School education

09. 2007 - 06. 2011	Gymnázium T. G. Masaryka Zastávka, Czechia

University education

09. 2011 - 06. 2015	Bachelor of Science in Physics University of Aberdeen, Scotland
11. 2016 - present	PhD in Theoretical Atomic Physics Faculty of Physics and Astronomy Friedrich Schiller University Jena, Germany

Employment

07. 2013 - 08. 2013	Research Fellow University of Aberdeen, Scotland
08. 2014 - 09. 2014	Lab assistant University of Giessen, Germany
07. 2015 - 11. 2016	Research Fellow Friedrich Schiller University Jena, Germany
11. 2016 - 12. 2019	Research Fellow Helmholtz Institute Jena, Germany

Rewards

Arnott Prize 2015	University of Aberdeen, awarded for the most distinguished performance in the experimental branches of Physics